The Dissertation Committee for Ian Alexander Durant Williamson certifies that this is the approved version of the following dissertation:

Subwavelength and Nonreciprocal Optical and Electromagnetic Systems for Sensing and Communications

Committee:

Zheng Wang, Supervisor

Andrea Alù

Seth R. Bank

Yaguo Wang

Edward T. Yu

Subwavelength and Nonreciprocal Optical and Electromagnetic Systems for Sensing and Communications

by

Ian Alexander Durant Williamson, B.S.E.E., M.S.E.

Dissertation

Presented to the Faculty of the Graduate School

of the University of Texas at Austin

in Partial Fulfillment

of the Requirements

for the Degree of

Doctor of Philosophy

The University of Texas at Austin

August 2017

The woods are lovely, dark and deep,
But I have promises to keep,
And miles to go before I sleep,
And miles to go before I sleep.

— Robert Frost

Acknowledgments

Although I am the author of this rather long document, writing it and carrying out this research would not have been possible without the support and encouragement of many people along the way. First and foremost thank you to my adviser, Zheng Wang. I have been able to learn a lot from working with him over the past four and a half years. As a result, I feel very well prepared for whatever challenges come next. I would also like to thank Professors Andrea Alù, Seth Bank, Yaguo Wang, and Ed Yu for serving on my committee.

It goes without saying that I would not be where I am today without the encouragement and unwaivering love of my parents, Paul Williamson and Nancy Durant. Thank you for everything. I am also grateful to Holly Marchant for her support and endless patience over the past four years.

I am also grateful to all of my friends, current coworkers, and former coworkers. During the time that I overlapped with Hossein Mousavi, I was able to learn a lot from my collaborations with him and his patient explanations have improved my understanding of many topics. In my first few semesters of this program I worked closely with Kristen Parrish and she was a great mentor at a time that I knew nothing. I'd also like to thank Thien-An Nguyen for being a great lab partner, research collaborator, and friend. Thank you to the other members of my research group as well: Boxue Chen, Danlu Wang, and Hui Dong. I am of course also grateful to all of my friends for their support and companionship during this journey. In particular, thanks to Jackson Massey who was a great roommate when we started this and remains a good friend today. Also thank you to Jon Rackham (my first friend at UT), Rhys Ulerich, Justin Shade, Scott Delgado, Jake Johnson, John Barnes, Danny White, Ben Rimmer, Shawn Mawdsley, Emily Walker, Tanuj Trivedi, and everyone else that I've forgotten to list here.

Finally, I would like to thank all of the staff in the ECE Department and the Microelectronics Research Center. In particular, a huge thank you is owed to Christine Wood for her tireless efforts to keep everything in our research group functioning and operating smoothly. Also, thank you to Melanie Gulick for always looking out for the ECE graduate students. She has been a huge help in making sure that every requirement was met for me to make it out the door and graduate.

Subwavelength and Nonreciprocal Optical and Electromagnetic Systems for Sensing and Communications

by

Ian Alexander Durant Williamson, Ph.D.
The University of Texas at Austin, 2017
Supervisor: Zheng Wang

This dissertation is organized into three parts.

First, the design for a radio frequency fiber transmission line built out of a grid of micrometer-scale conductors embedded in an insulating polymer cladding is presented to mitigate the skin and proximity effects. By adopting a checkerboard out-of-phase current phasing scheme, the internal inductance of the line is significantly lower than in two-conductor lines and results in an LC bandwidth of approximately 2 GHz, with flat attenuation and linear phase dispersion. The device performance is characterized in terms of its geometric degrees of freedom and a fabricated prototype is presented.

Second, the kinetic inductive and plasmonic response of monolayer graphene in the terahertz spectrum is examined in the context of several important applications. The dispersive responses of two-dimensional graphene and three-dimensional copper transmission lines are compared to map the dispersive signaling performance in terms of transmission line cross-sectional size. This demonstrates a surprisingly broadband LC response with flat attenuation in nano-scale lines. This kinetic inductive response of graphene is demonstrated to miniaturize the photonic band structure of a photonic crystal slab where an in-plane periodicity of 300 nm has its photonic band gap in the terahertz spectrum. The sub-diffraction photonic band structure resembles that of the two-dimensional photonic crystal, supporting a wide photonic band gap in extremely thin slabs. The viability of graphene for cavity optomechanics is analyzed from near infrared to terahertz

wavelengths, demonstrating a large optomechanical coupling, on the order of 3D optomechanical materials.

Third, a class of nonreciprocal devices is proposed based on coupling to the sideband states, called Floquet resonances, that arise in temporally modulated optical resonators. The degrees of freedom in the modulating waveform tailor the energy exchange and phase of the Floquet resonances to realize unique nonreciprocal spectral responses in compact devices. We examine optical scattering from Floquet resonators coupled to narrowband waveguides using temporal coupled-mode theory. A three-port circulator is built out of a cascade of Floquet resonators to demonstrate broadband forward transmission and ideal isolation for dual-carrier waves. Full-wave numerical simulations in the coupled frequency domain demonstrate the circulator in an on-chip photonic crystal platform.

Table of Contents

Chapter 1

Introduction

1.1 Overview

This dissertation deals with several projects in applied electromagnetics and optics that are relevant to time-domain sensing, high-speed digital communications, component miniaturization and integration, and the realization of magnet-free nonreciprocal responses. The applicable operating frequencies of these systems range from microwaves, through the terahertz spectrum, and all the way to the optical domain. Portions of the work covered in this dissertation have been published in the following peer-reviewed journal articles [1]–[4]:

1. I. A. D. Williamson, T.-A. N. Nguyen, and Z. Wang, "Suppression of the skin effect in radio frequency transmission lines via gridded conductor fibers," *Applied Physics Letters*, vol. 108, no. 8, p. 083 502, Feb. 22, 2016

2. S. H. Mousavi, I. A. D. Williamson, and Z. Wang, "Kinetic inductance driven nanoscale 2D and 3D THz transmission lines," *Scientific Reports*, vol. 6, p. 25 303, May 3, 2016

3. I. A. D. Williamson, S. H. Mousavi, and Z. Wang, "Extraordinary wavelength reduction in terahertz graphene-cladded photonic crystal slabs," *Scientific Reports*, vol. 6, p. 25 301, May 4, 2016

4. I. A. D. Williamson, S. H. Mousavi, and Z. Wang, "Large Cavity-Optomechanical Coupling with Graphene at Infrared and Terahertz Frequencies," *ACS Photonics*, vol. 3, no. 12, pp. 2353–2361, Dec. 21, 2016

1.2 Organization

This dissertation is loosely organized into three parts. The first part discusses the design and prototype of a radio frequency transmission line with a superior frequency response over conventional structures. The second part discuss three systems which leverage graphene's dispersive response in the terahertz spectrum:

broadband on-chip transmission lines, sub-diffraction photonic crystals and band structures, and low-mass cavity optomechanics. The third part discusses an approach to realizing magnet-free nonreciprocity in on-chip optical systems through selective spatial coupling of modulation-induced sidebands in resonators, called Floquet resonators.

1.2.1 Part I: Transmission Lines for Sensing and Communications

In Chapter 2 we present a design and fabricated prototype of a radio frequency transmission line that mitigates the skin and proximity effects. The device is made of a grid of μm-scale electrodes embedded in an insulating polymer cladding that can be readily fabricated using a thermal fiber-draw fabrication process. The fabrication procedure can produce meter to kilometer long fibers with well defined sub-micron features in its cross section. The performance of this so-called *Gridded Fiber* is characterized by an unprecedented signal bandwidth (approximately 2 GHz) of frequency-flat attenuation and linear phase dispersion which is enabled by an optimized current phasing scheme across the grid of electrodes.

The proposed design is significant because the skin and proximity effects fundamentally limit the bandwidth and reach of conventional (two-conductor) off-chip transmission lines and interconnects (Fig. 1.1, left). The constricted flow of electrical current at high frequencies in these systems causes an increased per-length resistance and reduced per-length inductance, and ultimately results in an attenuation coefficient with a square root frequency-dependence [5]. This low pass response limits the resolution of time domain transmission line sensors and creates a trade off between the maximum length and maximum data rate in transmission lines that are used as communication channels. Active signal equalizers and other loss compensation schemes can mitigate these issues. However, they come with increased power consumption, an increased system complexity, and a reduced noise tolerance. For interconnects, all-optical communication schemes have been proposed but high frequency electronic transceivers have superior dynamic range, are easier to integrate, and are cheaper [6], [7]. The *Gridded Fiber*, through its grid of electrodes, provides a platform that can be readily fabricated to overcome these issues that have long-plagued passive high-frequency transmission lines [8]–[10].

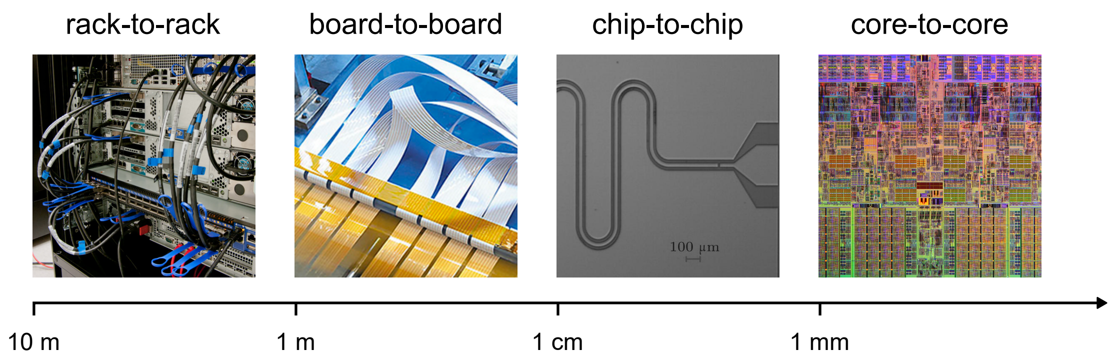

Figure 1.1: Classification of high frequency transmission lines with respect to their typical transmission distances. Rack-to-rack transmission lines span distances of more than 1 meter. Board-to-board transmission lines are up to approximately 1 meter in length. Chip-to-chip transmission lines span from 1 centimeter to several millimeters. Core-to-core transmission lines are typically less than 1 millimeter.

1.2.2 Part II: Subwavelength and Dispersive Graphene Systems

Chip-Scale 2D Transmission Lines

In Chapter 3 we examine the unusual dispersion and attenuation of chip-scale graphene and copper transmission lines in the terahertz spectrum. Our numerical modeling and analytical analysis across a wide range of frequencies and geometric sizes reveals that the conductor kinetic inductance provides a means for realizing a broad bandwidth of constant signal attenuation and linear phase dispersion with a size-independent low-frequency cutoff. In one sense, this response is the counterpart of the LC response realized by the *Gridded Fiber* presented in Chapter 2, but realized through an entirely different underlying physical mechanism.

This work is significant because on-chip transmission lines (Fig. 1.1, right) are conventionally thought to be limited by a large RC time constant that results from the increased resistance of sub-micron conductors. Additionally, the interplay between the kinetic inductance, the magnetic inductance, and the resistance has never been considered in the context of transmission line signaling performance over a large parameter space. We conduct a comprehensive comparison of the dispersion of copper and graphene transmission line performance through the RC, LC, and multi-mode plasmonic regimes. Furthermore, the higher-order frequency-dependent losses that adversely affect signaling performance are characterized. Our results demonstrate that the low frequency cutoff of a *kinetic* LC regime is defined by the phenomenological free carrier scattering rate in nanoscale lines and opens up the possibility of realizing a large bandwidth of flat signal attenuation. Moreover, up to 40$\times$ wavelength reduction is observed in the transverse electric-magnetic (TEM) mode of graphene transmission lines operating in the terahertz spectrum.

Sub-diffraction Photonic Crystals

In Chapter 4, we leverage the results of Chapter 3 to demonstrate that the kinetic inductance from two single-layer graphene sheets, effectively a graphene parallel plate waveguide, allow silicon photonic crystal slabs with sub-micron periodicity to operate in the terahertz regime (corresponding to a 100$\times$ wavelength reduction). Photonic crystals are the backbone for a number of important integrated photonic systems for light confinement, dispersion engineering, nonlinearity enhancement, and other unusual effects arising from their structural periodicity.

This work is significant because there is a need in photonic integrated circuits to combine a much larger number of optical components into a much smaller footprint (Fig. 1.2). We show that despite graphene's very dispersive optical response, the kinetic LC regime discussed in Chapter 3 can provide a platform for realizing a well confined out-of-plane mode and a scaled down in-plane photonic band structure. The photonic band structure that arises from the merger of the silicon photonic crystal and the graphene parallel plate waveguide is uniformly scaled from the corresponding 2D crystal, opening up the opportunity to realize many of the unique features of purely 2D optical systems. For example, the demonstrated system supports a large photonic band gap ($\sim$27%) and can confine light along in-plane line defect waveguides. Additionally, the propagation lengths are on the order of tens of lattice constants.

Low-Mass Cavity Optomechanics with 2D Materials

In addition to its unique optical response, graphene also exhibits many unusual elastic properties that make it an intriguing material for mechanical measurement and actuation at the quantum limit. In Chapter 5, we extend the results of Chapter 3 and Chapter 4 to characterize graphene's optomechanical properties in

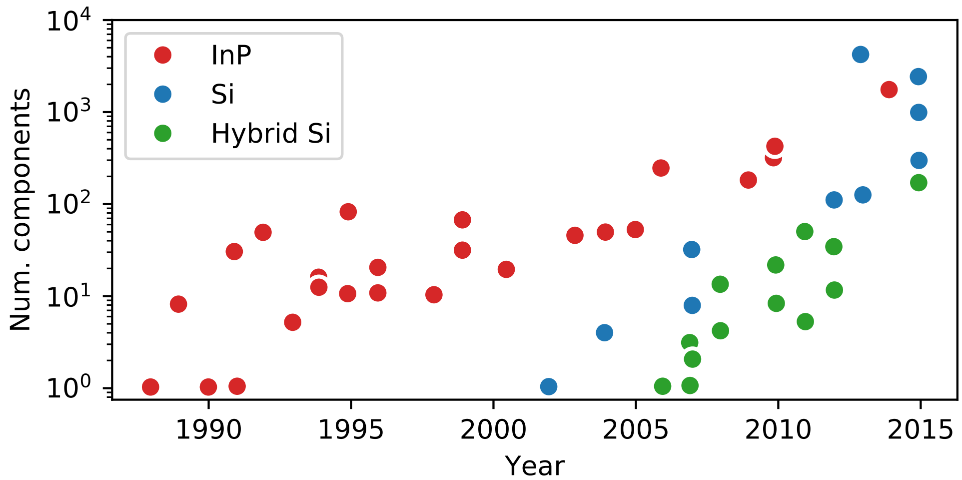

Figure 1.2: Number of integrated optical components for various photonic material systems: InP, Si, and Hybrid Si. Visualization and data based on the work of Heck [11], [12].

terms of fabrication parameters and operating conditions. We show that graphene is capable of supporting a large optomechanical coupling coefficient, on the order of those observed in state-of-the-art 3D optomechanical materials. With an operating frequency around 100 THz, the dispersive coupling coefficient reaches $g_{om} = 180$ MHz/nm and $g_{om} = 500$ MHz/nm in the resolved and unresolved sideband regimes, respectively. We find that predominantly dispersive coupling requires a high graphene Fermi level and mid-infrared excitation, while predominantly dissipative coupling favors a moderate graphene Fermi level and near-infrared excitation.

This work is significant because the field of cavity optomechanics can benefit from the unique mechanical properties of single- and few-layer graphene membranes, namely a large stiffness (~1 TPa) and a low mass $\left(\rho \sim 10^{-19}\ \mathrm{kg}/\mu\mathrm{m}^2\right)$. State-of-the-art graphene mechanical resonators have resonance frequencies on the order of 100 MHz and quality factors exceeding 10^4 (Fig. 1.3). Additionally, the low mass of graphene leads to orders-of-magnitude larger zero-point fluctuation amplitudes than what is achievable with higher dimensional materials such as silicon nitride [25]. Such a low mass also allows graphene resonators to support a reduced noise floor for optomechanical force sensing [26]–[28].

Graphene has yet to be considered as a promising material at optical frequencies for cavity optomechanics. Its large absorption is thought to set a limit on

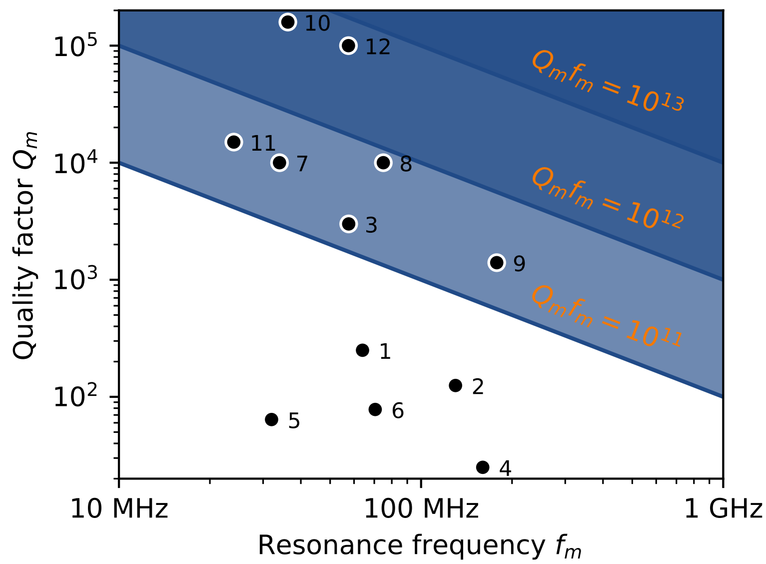

Figure 1.3: Quality factor and resonance frequency of experimentally demonstrated graphene mechanical resonators. 1: [13], 2: [14], 3: [15], 4: [16], 5: [17], 6: [18], 7: [19], 8: [20], 9: [21], 10: [22], 11: [23], 12: [24]. Contours indicate $Q_m f_m$ products of 10^{11}, 10^{12}, and 10^{13}.

the optical quality factor that is too low for most optomechanical phenomena and its strong dispersion in general makes it more challenging to choose the ideal combination of operational frequency and fabrication parameters. Moreover, graphene-based cavity optomechanical experiments to date have been limited mostly to microwave frequencies, where graphene is simply used as one of the conducting electrodes in a mechanically variable LC resonator [22]–[24]. At optical frequencies, graphene has been used for quantum-limited position and force readouts only through evanescent coupling to quantum emitters [29], [30] and microspheres [31], where the influence of radiation pressure is not exploited.

1.2.3 Part III: Magnet-Free Nonreciprocal On-Chip Optics

As the field of photonic integrated circuits (PIC's) continues to progress, many functionalities that previously existed only as discrete components have been incorporated into on-chip all-optical signal processing and communication systems. However, nonreciprocal components such as isolators and circulators have remained elusive in PIC's due to lingering challenges with material compatibility and the necessary large footprints for overcoming weak magneto-optical effects. The need for compact and high performing circulators and isolators with low insertion loss and high isolation is critical for protecting laser cavities from undesired reflections, reducing multi-path interference, routing reflective signals, and enabling full-duplex transmission over a single fiber. In Chapter 7 we introduce an approach for realizing nonreciprocal devices using on sideband-selective coupling of modulated resonators, which we call *Floquet* resonators.

This work is significant because none of the nonreciprocal schemes based on time-modulation proposed to date have made use of the degrees of freedom provided by modulation-induced sideband states. We demonstrate that by controlling the amplitude of individual Floquet sideband states through the modulating *waveforms*, unique nonreciprocal spectral responses can be realized in compact device structures. We examine the nonreciprocal phase shift and general scattering properties of a single parametrically modulated resonator side-coupled to two waveguides. Temporal coupled-mode theory is used to study the necessary conditions for producing a circulator response from a low-symmetry cascade of two Floquet resonators. A compact three-port circulator based on individually coupled Floquet sidebands is demonstrated that provides broadband nonreciprocal transmission that is distinct from conventional circulators and a photonic crystal realization is presented from the results of first-principle numerical simulations.

Part I

Transmission Lines for Sensing and Communications

Chapter 2

The Gridded Fiber: A Multi-Conductor Fiber Transmission Line for Mitigating the Skin and Proximity Effects *

Composite conductor-insulator geometries have long been realized for mitigating current crowding caused by the skin effect. For example, Litz wires are commonly used in kHz-MHz transformer windings and other magnetic devices [32]. These wires consist of conductor strands which are precisely braided so that each strand spends an equivalent distance at the surface of the bundle. However, Litz wires are subject to the proximity effect among the individual strands [33]. Another approach, first proposed over sixty years ago, arranges alternating conducting and insulating layers in a coaxial configuration [34]. Known as Clogston lines, these designs have stringent requirements on the geometric and material parameters and lack a scalable fabrication process for mass producing extended lengths of cabling [35]–[37].

In this chapter, the combined effects of a micro-structured cross-sectional geometry and current phasing in are investigated for suppressing both skin and proximity effects, as well as the associated frequency-dependent attenuation. The proposed structure, which we refer to as the "gridded fiber," consists of a grid of μm-wide electrodes embedded inside of a polymer cladding. Such a fiber structure is made possible by a recently developed top-down thermal-drawing process capable of producing kilometer-long uniform fibers with arbitrary cross-sectional geometries and nanometer feature sizes [38]–[41]. We first illustrate that the key to suppressing skin and proximity effects is to reduce the stored magnetic energy internal to the conductors. This understanding allows us to deliberately arrange conduction currents of opposite polarity in a "checkerboard" pattern and to employ sub-skin depth widths for individual electrodes. Ultimately this leads to the realization of a broadband frequency-flat attenuation regime that outperforms two-conductor lines.

*A subset of the work discussed in this chapter is published in Ref [1]. I.W. performed the numerical and analytical modeling and developed the physical intuition that led to the optimal configuration. In collaboration with T.N. the prototypes were fabricated to realize the optimal structure.

2.1 Transmission Line Circuit Model

The underlying connection between the skin effect and the transmission line signal attenuation can be represented through distributed circuit parameters that account for the spatial distribution of the magnetic flux. The transverse electromagnetic (TEM) mode has a complex propagation constant defined as [42]

$$\gamma(\omega) = j\beta(\omega) + \alpha(\omega) = \sqrt{(R + j\omega L)(j\omega C)} \tag{2.1}$$

where R, L, and C correspond to the resistance, inductance, and capacitance per unit length, respectively. The attenuation is determined by the real part of the above expression, $\alpha(\omega)$, while the phase delay is determined by the imaginary part, $\beta(\omega)$. The resistance and inductance depend on the distribution of the conduction current density $\mathbf{J}$ and magnetic field $\mathbf{H}$ respectively, as

$$R(\omega) = \frac{1}{I^2} \iint \sigma^{-1} |\mathbf{J}|^2 dA, \tag{2.2}$$

and

$$L(\omega) = \frac{1}{I^2} \iint \mu |\mathbf{H}|^2 dA. \tag{2.3}$$

σ and μ correspond to the material conductivity and permeability, and I corresponds to the magnitude of the total current flowing in one direction (i.e. outgoing or returning) on the line. Depending on the relative magnitudes of the inductive and resistive impedances, the transmission line can be classified [10] as operating in the RC regime at low frequencies ($\omega L < R$) or the LC regime at high frequencies ($\omega L > R$). The RC regime is highly dispersive with $\gamma \cong \sqrt{j\omega RC}$ while the LC regime is characterized by a linear dispersion with $\gamma \cong j\omega\sqrt{LC} + R/2\sqrt{C/L}$. The LC regime attenuation is given by

$$\alpha_{LC} \cong R/\left(2Z_{0,\omega\to\infty}\right), \tag{2.4}$$

which is constant if there is negligible dispersion in R and the impedance, $Z_0(\omega) = \sqrt{(R + j\omega L)/j\omega C} \underset{\omega\to\infty}{\cong} \sqrt{L/C}$.

In two-conductor transmission lines, the LC cutoff frequency, $\omega_{LC} = R/L$, lies just below the skin effect onset frequency for two reasons [10]. First, many transmission line applications operate within a limited range of characteristic impedances (25 - 75 Ω), which requires a comparable electrode size and separation. This requirement leads to the internal inductance, corresponding to the magnetic energy residing inside the conductors, being a substantial portion of the total inductance (Fig. 2.1a). For example, in a 40 Ω twisted pair $L_e = 0.25\ \mu$H/m and $L_i = 0.15\ \mu$H/m, thus $L_i \sim 0.6 L_e$ where $L = L_e + L_i$. Second, since current takes the distribution of minimum impedance (where impedance is actually the quantity, $R + j\omega L$), the skin effect onset occurs once the internal inductive impedance exceeds the resistance, and is given by $\omega_{skin} \cong R/L_i$. This implies that ω_{skin} only exceeds ω_{RC-LC} by the factor L_e/L_i.

Essentially, two-conductor transmission line designs, such as the twisted pair, will always have dispersive attenuation: either from the RC response at low frequencies or the skin effect at high frequencies (Fig. 2.3c). There is no practical means for increasing the ratio L_e/L_i with only two conductors.

2.2 Comparison of Two- and Multi-Conductor Transmission Lines

The gridded fiber overcomes the fundamental issue outlined above by segregating the conduction area into many discrete subsections (Fig. 2.1b,c). The smaller lateral dimensions of individual electrodes make them affected by the skin effect at a higher on-set frequency, while their large aggregate area ensures a low overall DC resistance. To mitigate the proximity effect, outgoing and returning currents are interleaved in a checkered pattern which allows the magnetic flux generated by the currents from neighboring electrodes to cancel out inside a given conductor. The magnetic flux external to the conductor is less affected, with a large overall increase in L_e/L_i (Fig. 2.2).

In contrast, for a two-conductor line, or for a multi-conductor line without the checkered current pattern, magnetic flux generated by current elements of the same polarity constructively add up, and the only way to increase L_e/L_i is to use an impractically large conductor separation (to increase L_e) which results in a very large characteristic impedance. For example, a twisted pair would need to be configured with a high frequency characteristic impedance exceeding 200 Ω to achieve

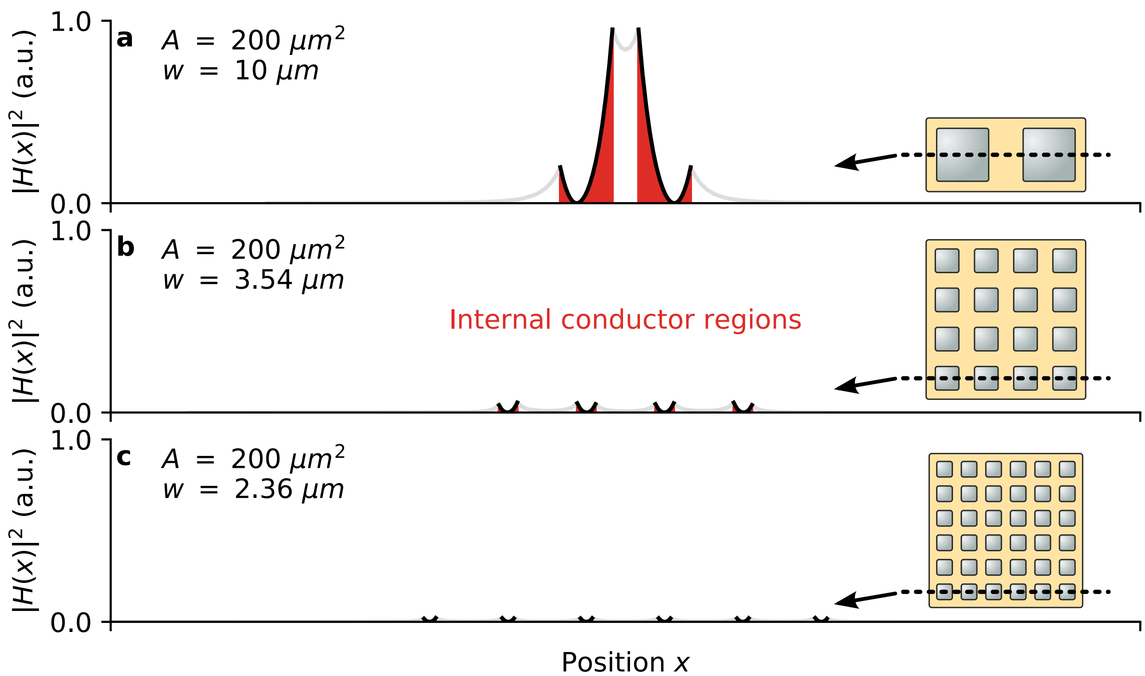

Figure 2.1: Profile of $|\mathbf{H}|^2$ for (a) 2×1 conductor transmission line and across a single row of a (b) 4×4, and (c) 6×6 conductor transmission line. Current phasing in the 4×4 and 6×6 is in a checkerboard configuration and all three lines have an equivalent conduction area. Red shaded regions correspond to the result of $\iint |H|^2 dA$ over the "internal" conductor region. The x- and y-ranges for (a), (b), and (c) are equivalent.

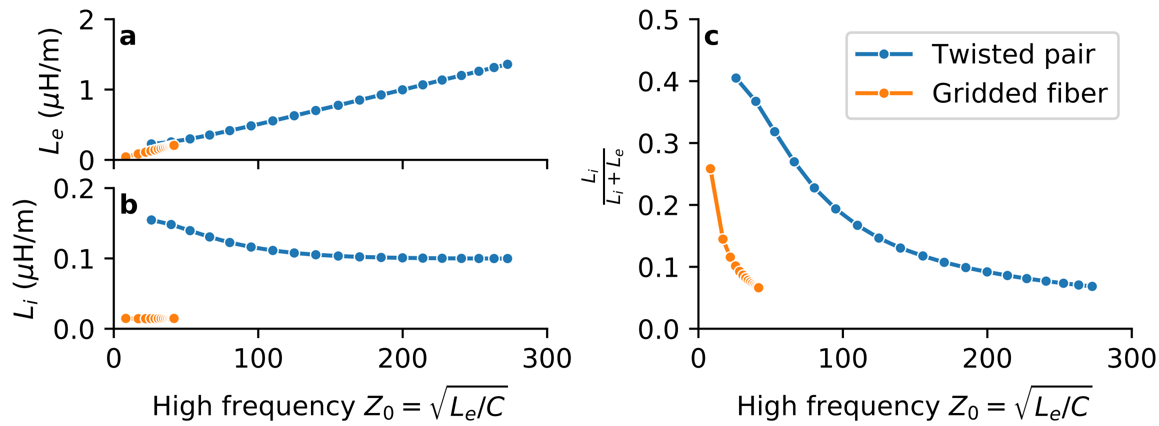

Figure 2.2: (a) External and (b) internal inductance. (c) Ratio of internal to total inductance as a function of the high frequency characteristic impedance, Z_0. The relative conductor separation is the structural degree of freedom used to tune Z_0.

$L_e/L_i \approx 10$ (Fig. 2.2).

The gridded fiber's dramatically improved conductor utilization can be visualized by contrasting the computed current density of the fiber (Fig. 2.3d) with that of the twisted pair (Fig. 2.3b inset) at 1 GHz. Both lines have an equivalent metallic area but only the gridded fiber is able to mitigate current crowding. This improvement pays dividends for the fiber, as this configuration is capable of supporting over 2 GHz of flat-attenuation bandwidth (Fig. 2.3e). Note that throughout this chapter we have assumed copper conductors (conductivity, $\sigma = 5.8 \times 10^7$ S/m) and a cladding dielectric with a relative permittivity of $\varepsilon_r = 2.2$, which is typical of a number of polymers and glasses. All results were computed by COMSOL Multiphysics, where the phase and attenuation are extracted directly from the complex eigenvalues and the circuit parameters are computed from the mode field distributions.

A drawback of having a large number of discrete electrodes in the gridded fiber is a significantly increased surface area, which translates to an increased capacitance and reduced characteristic impedance. For it to achieve an impedance comparable to that of a twisted pair with an equivalent conducting area, the fiber requires a larger electrode pitch-to-width ratio ($a/w > s/d$). The $a/w = 5$ value that we have used so far is sufficient to obtain a reasonably large high frequency impedance of $\sim 15\ \Omega$ (Fig. 2.5a). The diverging resistive and reactive components of

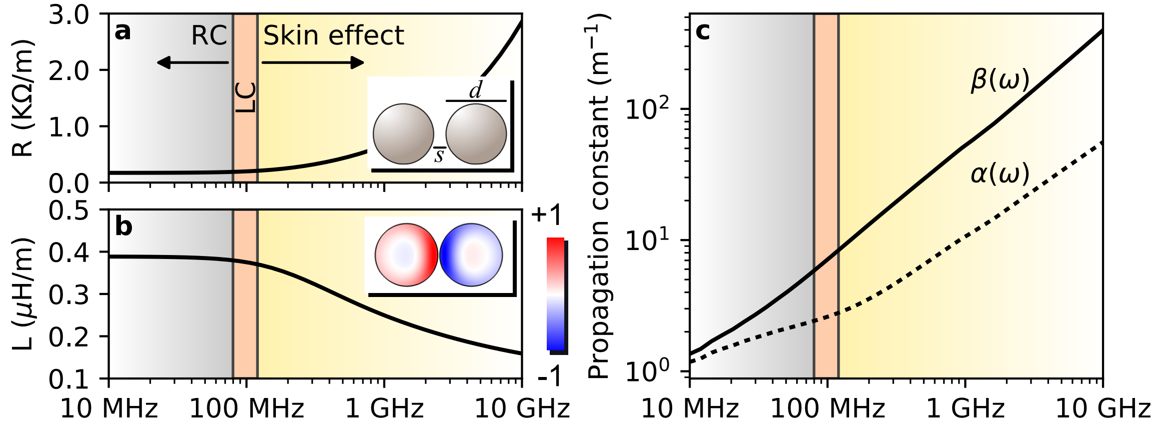

Figure 2.3: Spectra of (a) distributed resistance, (b) distributed inductance, and (c) attenuation constant and phase constant for a twisted-pair transmission line with $d = 16\,\mu$m, $s = 0.03d$ calculated using a full-field finite element eigensolver. (insets) Schematic and instantaneous current density at 1 GHz of twisted pair.

the impedance at low frequencies is characteristic of all TEM modes on microwave transmission lines [10].

2.3 Prototype Fabrication

The SEM micrograph of a fabricated prototype (Fig. 2.5a, inset) demonstrates that the w = 5 μm and a = 25 μm configuration can be readily obtained with bismuth-tin (Bi-Sn) eutectic alloy conductors and polycarbonate (PC) cladding. The macroscopic preform of the fiber was fabricated by vacuum oven consolidation of stacked PC slabs with embedded Bi-Sn wires at a temperature of 155 °C. Two successive fiber draws were performed (Table 2.1) between which fiber segments from the first draw were vacuum-consolidated in PC cladding films for the subsequent draw. The first draw had a down feed speed of 0.04 mm/sec and capstan speed of 0.65 m/min and the second draw had a down feed speed of 0.06 mm/sec with a capstan speed of 1.28 m/min. Furnace temperatures were configured to maintain an average drawing stress of 2 MPa and 7.5 MPa for the first and second draw, respectively.

Due to Bi-Sn's reduced conductivity (approximately 4.5% of copper's), the LC regime of the prototype resides at higher frequencies and has larger attenuation

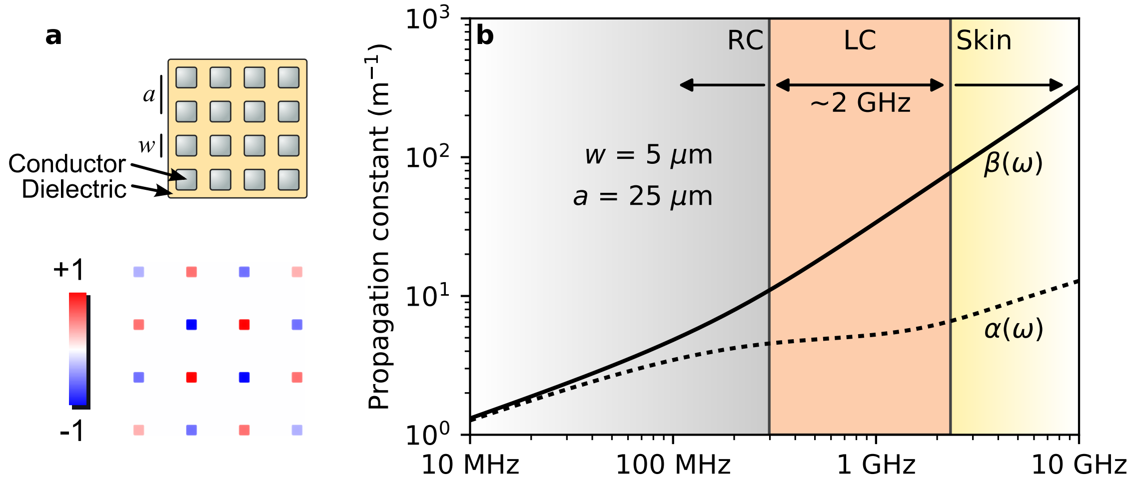

Figure 2.4: (a) (top) Schematic of gridded fiber and (bottom) instantaneous current density at 1 GHz showing the "checkerboard" distribution. (b) Calculated spectra of phase and attenuation constant of the gridded fiber with $w = 5\ \mu$m, $a = 25\ \mu$m supporting approximately 2 GHz of LC bandwidth.

Stage	Average stress	Down feed speed	Capstan speed
1	2.0 MPa	0.04 mm/sec	0.65 m/min
2	7.5 MPa	0.06 mm/sec	1.28 m/min

Table 2.1: Summary of fabrication conditions and parameters for fiber prototype shown in the inset of Fig. 2.5a.

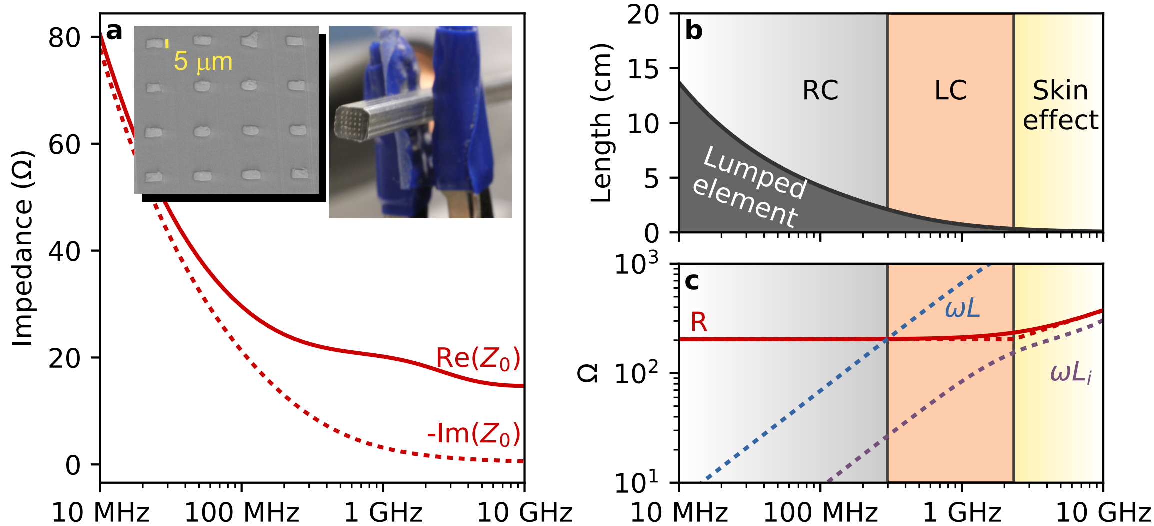

Figure 2.5: (a) Simulated characteristic impedance of a 4×4 gridded fiber with w = 5 μm, a = 25 μm (identical to Figure 2.4). Inset shows a SEM micrograph of a fiber prototype fabricated with polycarbonate cladding and Bi-Sn electrodes and a photograph of the fiber end facet before being thermally drawn. (b) Operational frequency ranges of the gridded fiber and lumped element cross-over length. (c) Simulated distributed resistance, inductive impedance, and internal inductive impedance of the gridded fiber as a function of frequency. The RC-LC transisition occurs when the inductive impedance crosses the resistance and the LC-skin effect transisition frequency occurs where the extrapolated flat-DC resistance intersects the skin effect resistance slope.

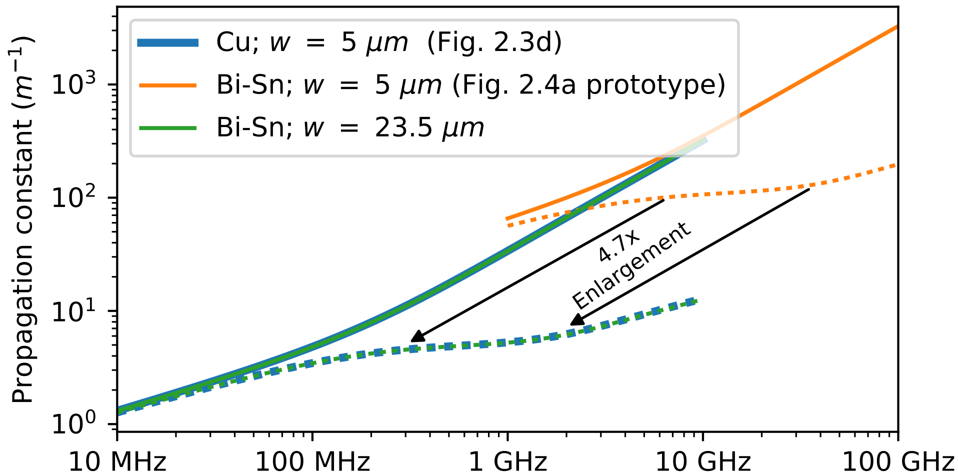

Figure 2.6: Computed $\beta(\omega)$ (solid lines) and $\alpha(\omega)$ (dashed lines) for a copper conductor gridded fiber that is identical to the structure in Fig. 2.4, a Bi-Sn fiber identical to the prototype shown in Fig. 2.5, and a Bi-Sn fiber that has been enlarged from the prototype by a factor of 4.7 to achieve a performance equivalent to that of the Cu design. All fibers have $a/w = 5$.

(both proportional to the increase in resistance, see Fig. 2.6). To achieve an equivalent performance to that of the simulated copper design, the Bi-Sn fiber would need its dimensions enlarged by a factor of $\sqrt{1/0.045} \approx 4.7$ to reduce its resistance. The fabricated fiber demonstrates micron sized electrodes and an enlarged fiber can be easily obtained by adjusting the reduction ratio of our successive fiber draws (Fig. 2.6). Also, in principal copper filaments could be co-drawn [43] with silica to fabricate our simulated structure.

The numerically calculated operating regime ranges as a function of length are shown in Fig. 2.5b for the copper conductor fiber. The LC region and the associated constant attenuation becomes relevant when the fiber length exceeds just several centimeters, $L > 0.25/|\gamma(\omega)|$.

2.4 Performance Scaling: Electrode Size and Distribution

The scaling of the characteristic impedance is important in determining if a simple "tiling out" of additional electrodes can further reduce the attenuation. Additional electrodes decrease R and Z_0 in tandem. While R is reduced because of the increased conducting area, Z_0 is reduced through L and C. For example, tiling a

$2{\times}2$ fiber out to a $4{\times}4$ fiber will scale L by $1/4$ and C by 4, which leads to Z_0 scaling by $1/4$. Since R also scales by $1/4$, the propagation constant remains unchanged by the tiling if the electrode size and pitch remain constant.

Rather than reducing the propagation loss, the gridded fiber offers the ability to tune the size and extent of the LC bandwidth through its grid configuration. We demonstrate this in simulated $2{\times}2$, $4{\times}4$, and $6{\times}6$ fiber grid sizes with electrode widths of 10 μm, 5 μm, and 3.33 μm; and center-to-center spacing of 15.5 μm, 25 μm, and 133.3 μm, respectively. These parameter combinations have an equivalent total conducting cross sectional area and an approximately equivalent characteristic impedance. Fig. 2.7a demonstrates that the magnitude of the attenuation remains the same in the LC region but the skin effect onset shifts to higher frequencies for smaller electrodes. Such performance engineering is entirely unique to the gridded fiber and has no analogue in any two-conductor transmission lines.

Aside from constituent material parameters, conductor size and separation are the only parameters that can tune the performance of a two conductor line. Fig. 2.7b plots the resistance of the three fiber configurations (red, blue, and green) from Fig. 2.7a along with the resistance of two twisted pair configurations (light grey and dark grey). The light grey curve corresponds to a twisted pair that has been scaled by a factor of 1/2 from the twisted pair represented by the dark curve. Although the smaller twisted pair has a higher skin effect onset frequency it also has a larger DC resistance. There are simply not enough degrees of freedom to independently tune the different performance features of the twisted pair.

For a gridded fiber with a uniform lattice of electrodes, even though current maintains a uniform distribution over the cross-section of individual electrode, larger grid sizes result in a non-uniform distribution of *currents across the electrode grid*. As a result of the magnetic fields of edge electrodes being unbalanced from the outside, an "anti-skin effect" results in a reduced current density near the grid surface, and a larger effective DC resistance than what a simple geometric (conductor area) analysis reveals. Fig. 2.7b highlights this effect in the left-most-portion of the resistance curve for each fiber.

To achieve a large LC bandwidth (Fig. 2.7c, left axis), a significant increase in the electrode separation is needed for an increase in the grid size (Fig. 2.7c, right axis); this is a key limitation of the gridded fiber design. The electrode separation must be increased to maintain a large characteristic impedance and to avoid drastically increasing the attenuation magnitude in the LC regime. The 6×6 design considered earlier has $a/w = 40$, while an 8×8 design would require a/w to exceed 100 to achieve a comparable signal attenuation and characteristic impedance, representing a potential practical upper limit on the grid size.

2.5 Discussion

The gridded fiber is a compelling alternative to two-conductor transmission lines which significantly mitigates the low pass frequency response associated with the skin effect. Importantly, we have shown that only a relatively small grid size (4×4) is needed to open up over 1 GHz of LC bandwidth.

The 25 μm electrode pitch that we have chosen for the 4×4 design results in an extremely small physical footprint for the overall device; the total width of the fiber cross section is only approximately 0.1 mm^2. This ensures that the fiber can be integrated with transceiver packaging or other circuitry. For applications where larger or smaller end facets are required the thermal draw process is capable of tapering the fiber ends.

The thermal draw process inherently introduces variations in feature sizes down the length of the fiber. In the case of our Bi-Sn prototype, these were on the order of 1% across 1 meter which will negligibly impact the fiber bandwidth and performance. Additionally, the smoothness of the variations means that the line impedance will not change abruptly, and signal reflections can be avoided. Overall, these features make the gridded fiber well suited for high speed chip-to-chip and board-to-board interconnect applications or distributed sensing systems.

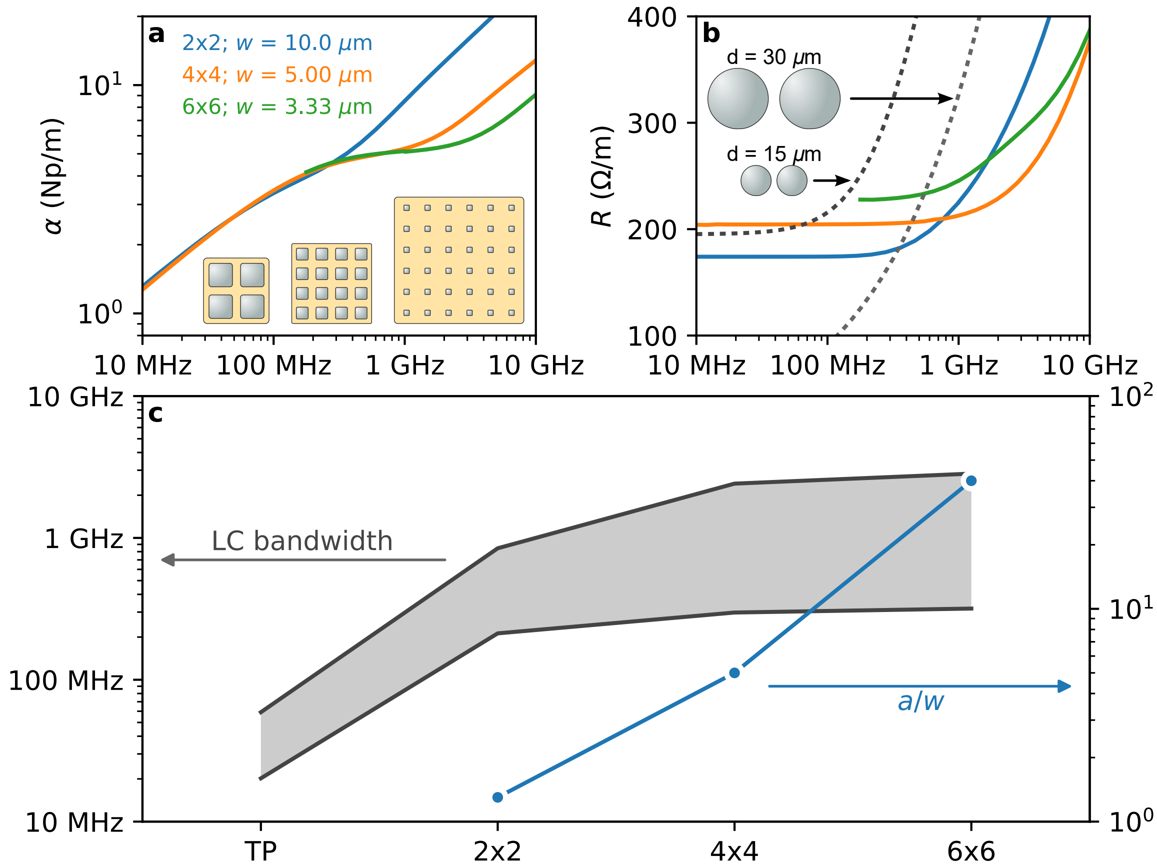

Figure 2.7: (a) Calculated attenuation spectra and the associated cross sections of 2×2, 4×4, and 6×6 fibers having 10 μm, 5 μm, and 3.33 μm electrode widths with 15.5 μm, 25 μm, and 133.33 μm center-to-center electrode spacing, respectively. These parameters are selected to maintain constant conducting area, characteristic impedance, and attenuation in the LC region. (b) Resistance spectra of the three fibers from (a) along with two twisted pairs. (c, left axis) LC flat-attenuation bandwidth for the gridded fibers in (a) and (b) and the twisted pair from (b) having $d = 30\ \mu m$. (c, right axis) Value of a/w for the three gridded fiber designs.

Part II

Subwavelength and Dispersive Graphene Systems

Chapter 3

Mapping the Performance of Terahertz Transmission Lines *

Although various graphene transmission line structures have been studied separately in the microwave [44]–[46] and optical regimes [47], [48], there exists no comprehensive study of their performance over a wide range of length scales and operating frequencies. Such a study is of significant interest for chip-scale transmission lines due to graphene's dominant kinetic inductance at relatively low THz frequencies [49]. The kinetic inductance of graphene has been previously exploited in infinite sheets and nano-ribbons for ultra-short-wavelength graphene plasmons [47]–[51] and stems from the kinetic energy of oscillating free charges. It is also significant in superconductors [52] at microwave frequencies and metals at optical frequencies [53].

In this chapter, we examine the effect of the material kinetic inductance on the propagation and attenuation of the transverse electromagnetic modes in nanoscale and microscale transmission lines. Over a vast parameter space, spanning 10^6-fold variation in dimensions (nm through cm) and 10^4-fold variation in frequency (10 GHz - 100 THz), we examine the conditions for the kinetic inductance to produce a surprisingly broadband LC region for small-scale transmission lines. Investigating both graphene and copper conductors, we develop a map of the performance regions for 2D and 3D materials, contrast the significant differences in their scaling laws, and explain dominant physical mechanisms that limit their performance.

Throughout our analysis we focus on the coplanar stripline (CPS) shown in Fig. 3.1 because it exhibits the typical skin effect induced attenuation and is widely used in integrated systems [54] and traveling wave modulators [55]. The CPS consists of two parallel conductors on top of a dielectric substrate [56], [57]. We consider two distinct CPS designs with two different conductor materials: one with single-layer graphene ribbons and the second with copper conductors. The copper wires have a finite thickness t and the graphene ribbons are treated as an

*A subset of the work discussed in this chapter is published in Ref [2]. I.W. performed analytical and numerical modeling with assistance from S.H.M. Both I.W. and S.H.M. contributed to the analysis.

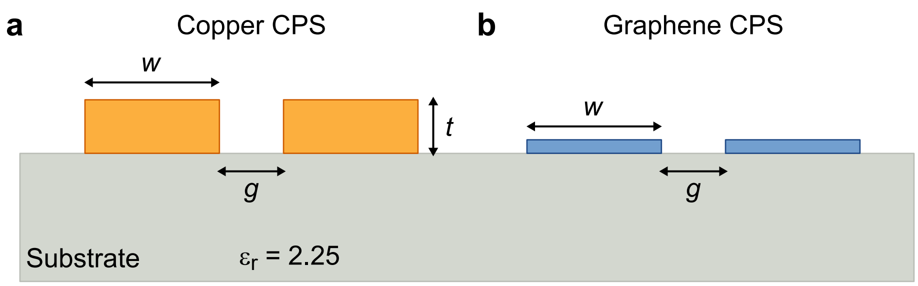

Figure 3.1: Cross-section schematic of (a) copper and (b) graphene coplanar strip line (CPS). The conductor width and separation are w and $g = w/2$, respectively. The copper conductors have a thickness $t = w/2$. The substrate is assumed to be lossless and non-magnetic with a relative permittivity $\epsilon_r = 2.25$.

infinitesimally thin surface conductors.

3.1 Optical Response of Graphene: The Kinetic Inductance

The complete optical response of graphene is modeled as an infinitesimally thin conducting surface with a surface conductivity given by $\sigma(\omega) = \sigma_d(\omega) + \sigma_i(\omega)$, where the Drude conductivity is given by [58],

$$\sigma_d(\omega) = -j\frac{e^2 k_B T}{\pi\hbar^2}\frac{1}{(\omega - j\gamma)}\left[\frac{E_F}{k_B T} + 2\ln\left(e^{-E_F/k_B T} + 1\right)\right], \tag{3.1}$$

and the interband conductivity is given by,

$$\sigma_i(\omega) = \frac{je^2}{4\pi\hbar}\ln\left(\frac{2|E_F| - (\omega - j\gamma)\hbar}{2|E_F| + (\omega - j\gamma)\hbar}\right). \tag{3.2}$$

E_F is the Fermi level, determined by chemical doping or electrostatic gating, and γ is the phenomenological free-carrier scattering rate which parameterizes the losses. At THz frequencies and below, both copper and graphene are accurately modeled with just a Drude conductivity of the form [50]

$$\sigma(\omega) = \frac{\sigma_0}{1 + j\omega/\gamma}. \tag{3.3}$$

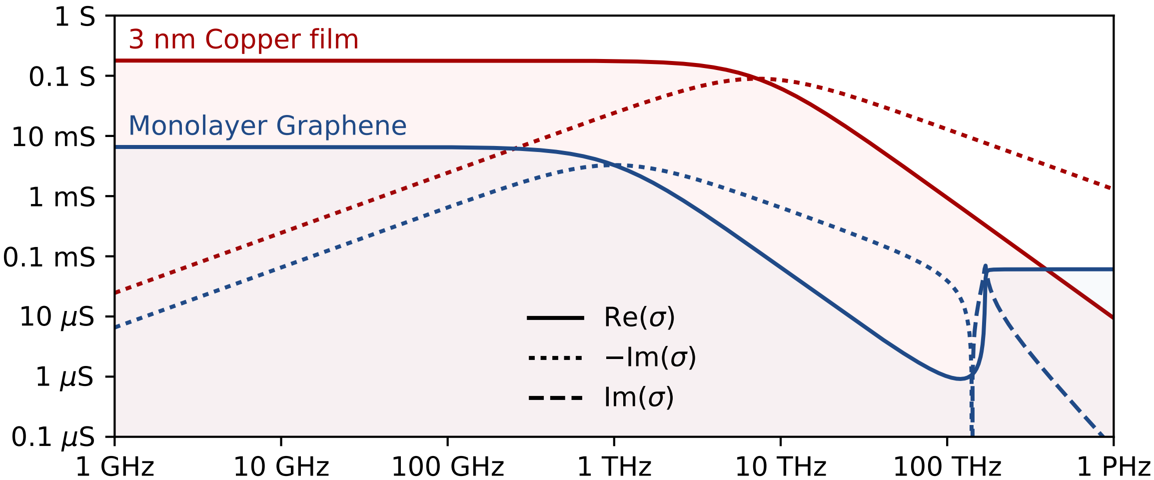

Figure 3.2: Complex-valued surface conductivity of monolayer graphene (blue) compared with the effective surface conductivity of a 3 nm copper film (red). Graphene has a Fermi level of 0.35 eV and a scattering rate of 1 THz and copper has a scattering rate of 7.26 THz and a DC conductivity of 2×10^7 S·m.

σ_0 is the DC bulk conductivity (surface conductivity) for (graphene) copper. Scattering effects due to surface roughness, finite temperature effects, and spatial dispersion are neglected. The *effective* surface conductivity $\sigma_s = \sigma_0 \times t$ for a 3 nm thick copper film is more than an order of magnitude larger than the graphene surface conductivity (Fig. 3.2). Thicker copper films are used throughout the rest of this chapter, which implies an even higher conductance in the copper transmission lines that we consider. For copper the scattering rate γ = 7.26 THz [59] while for graphene the scattering rate is γ = 1 THz [60]. Note that these values are representative and the main points of this analysis do not rely on specific values for γ or σ_0.

The complex-valued conductivity is what results in the kinetic inductive impedance, which is proportional to the imaginary part of the reciprocal of the conductivity, while the resistive impedance relates to the real part. Similarly to Eqn. 2.2, they contribute to the power stored or dissipated, respectively, in the conduction currents in the quantity

$$RI^2 + j\omega L_K I^2 = \iint \mathbf{J}^* \cdot \mathbf{E}\, dA = \iint \sigma^{-1} |\mathbf{J}|^2 \, dA \tag{3.4}$$

$\mathbf{J}$ is the surface or volume current density produced by an electric field, $\mathbf{E}$. From

Eqn. 3.4 we can conclude that the ratio of the kinetic inductive impedance and the resistance and simplifies to

$$\frac{\omega L_K}{R} = \frac{\mathrm{Im}\{\sigma^{-1}\}}{\mathrm{Re}\{\sigma^{-1}\}}. \tag{3.5}$$

This ratio depends only on the conductivity and therefore, may be dispersive, but is *completely independent* of the transmission line geometry. Similarly to the resistance, the kinetic inductance is also inversely proportional to the current carrying area A (or width w in the case of graphene), but unlike the resistance it is related to the imaginary part of the inverse conductivity,

$$L_K = \mathrm{Im}\left\{\sigma^{-1}\right\}\omega^{-1}A^{-1}, \tag{3.6}$$

so it becomes significant only at high frequencies.

When the conductivity is represented by the Drude model, Eqn. 3.5 simplifies even further to $R = \gamma L_K$. Below the skin effect onset, both R and L_K are frequency-independent, even at frequencies above the scattering rate. In this regime, the kinetic inductance is given by

$$L_K = {\sigma_0}^{-1}A^{-1}\gamma^{-1}. \tag{3.7}$$

In contrast to the Faraday inductance, the kinetic inductance increases with current crowding (i.e., when the conduction area becomes smaller); lines with a dominant kinetic inductance suppress current crowding because current favors a distribution of lowest total impedance.

3.2 Geometric Dependence of Circuit Parameters

Nanoscale lines are where the kinetic inductance typically exceeds the Faraday inductance. Generally, the Faraday inductance of a transmission line is scale-invariant $L_F = L_0 \ln(w/g)$, where L_0 is a geometry dependent constant [8]. Thus, given a specific aspect ratio for the conductor size and separation $t/w = m$ and $g/w = m'$, where $m = m' = 1/2$ in our design, the size threshold at which the kinetic inductance exceeds the Faraday inductance is given by

$$w_{K,3D} = \frac{1}{\sqrt{\sigma_0 \gamma m L_0 \ln(1/m')}} \quad (3.8)$$

$$w_{K,2D} = \frac{1}{\sigma_0 \gamma L_0 \ln(1/m')} \quad (3.9)$$

for 3D conductors and 2D conductors, respectively. For the transmission line configurations chosen in this chapter, $w_{K,3D}$ and $w_{K,2D}$ are on the order of 100 nm and 100 μm for copper and graphene, respectively. Copper's much lower threshold is partly due to the square root dependence in Eqn. 3.8 and partly due to its much larger DC conductivity (Fig. 3.2). If a lower intrinsic scattering rate can be achieved, the threshold can be increased, with more mileage being gained in 2D materials.

In transmission lines with conductors that are below the thresholds given in Eqn. 3.8 and Eqn. 3.9, the onset of the LC region is

$$\omega_{LC} = \frac{R}{L_K} = \gamma. \quad (3.10)$$

This surprisingly simple relationship suggests that the LC region and its associated constant attenuation can be found immediately above the intrinsic scattering rate. This is in contrast to transmission lines which are Faraday inductance dominated, where ω_{LC} depends strongly on the geometry. Therefore, two design conditions must both be satisfied to achieve a broadband kinetic LC response: $w < w_K$ and $\omega > \gamma$.

Finite element modeling confirms the above conditions through the inductive and resistive impedances (Fig. 3.3) that have been calculated directly from the TEM mode's field distribution. We consider a 25$\times$ size scaling of a copper (Fig. 3.3a) and a graphene (Fig. 3.3b) CPS, from w = 20 nm to 500 nm. The conductor separation (as well as the copper conductor thickness) are equal to $w/2$ (i.e. $m = m' = 1/2$ in Eqn. 3.8 and Eqn. 3.9). The resistance and the kinetic inductance of the CPS lines both decrease, by 25$\times$ in the graphene lines and by 625$\times$ in the copper lines, while the Faraday inductive impedances remain unchanged (grey curves). Both the large and small graphene CPS designs are kinetic inductance-dominated but with copper, only in the smaller of the two lines is kinetic inductance-dominated. In the

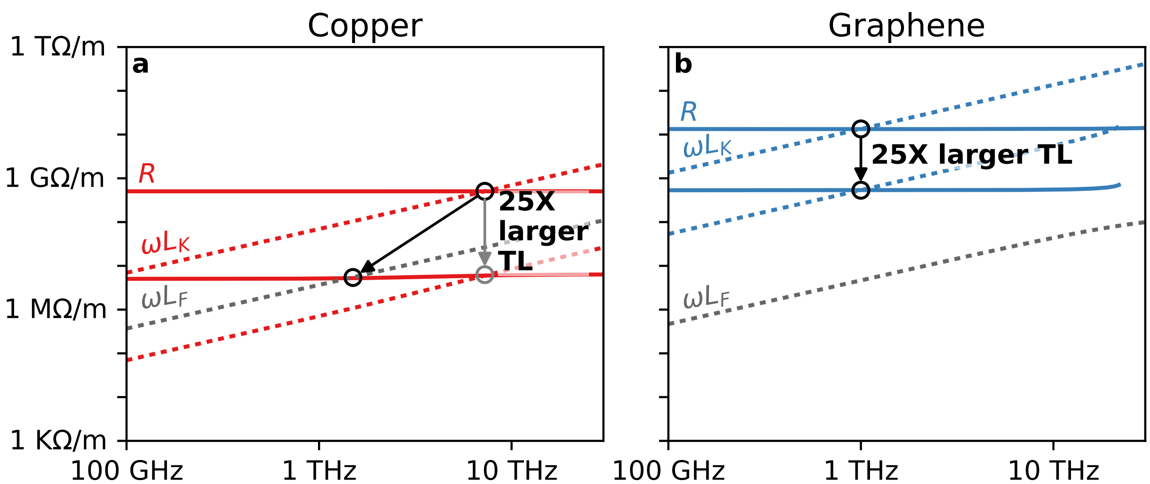

Figure 3.3: Effect of geometric scaling on the distributed circuit parameters of CPS line made of (a) copper and (b) graphene. A 25× size increase, from (w = 20 nm, g = 10 nm) to (w = 500 nm, g = 250 nm) (and additionally t = 10 nm to 250 nm for copper), reduces both R (solid curves) and ωL_K (dashed curves) by 625× for copper and 25× for graphene. ωL_F (gray curves) remains unchanged under scaling in both the copper and graphene CPS due to a fixed w/g ratio.

graphene lines, the two electrode widths are both below the threshold predicted by Eqn. 3.9 but the widths of the copper lines straddle the threshold given by Eqn. 3.8. Thus, the $w = 20$ nm and $w = 500$ nm graphene CPS lines have an LC onset frequency that is exactly equal to the intrinsic scattering rate of graphene (1 THz). In the $w = 500$ nm copper CPS, although R and ωL_K intersect at the same frequency, ω_{LC} is instead determined by the intersection of R and ωL_F, at approximately 1.5 THz.

3.3 Spectral- and Size- Performance Mapping

The classifications of the performance made above are also reflected in the spectra of $\alpha(\omega)$ and $\beta(\omega)$ that were calculated from modal eigenvalue simulations. We consider copper and graphene CPS's in Fig. 3.4 and Fig. 3.5 with several electrode widths in addition to those from Fig 3.3. The LC onset corresponds to the divergence of $\alpha(\omega)$ and $\beta(\omega)$ from their shared values in the RC region. All of the graphene CPS's (Fig. 3.5), regardless of width, have LC regions that start at precisely the intersection frequency of ωL_K and R in Fig. 3.3a; the copper CPS's have an

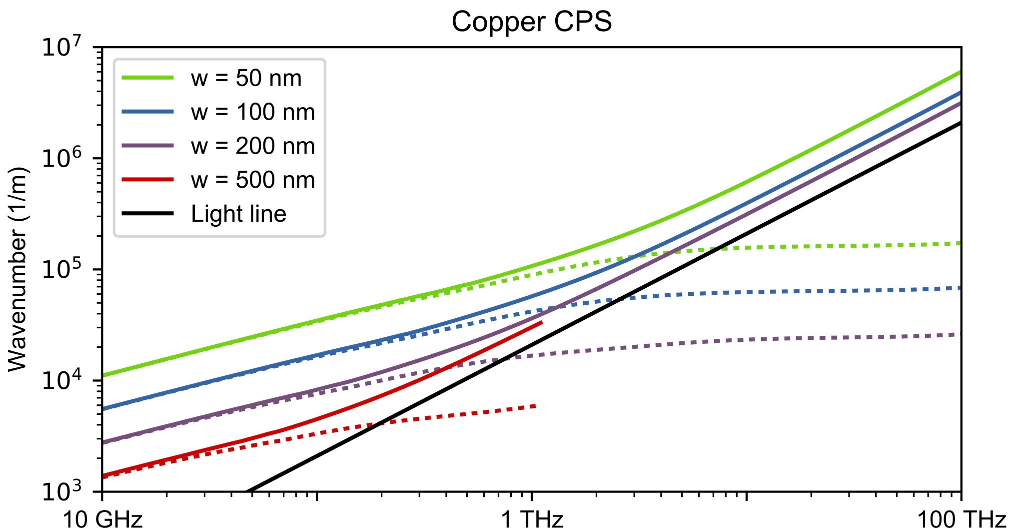

Figure 3.4: Attenuation and dispersion spectra for copper CPS transmission lines for various conductor widths.

LC onset frequency that shifts to lower values for larger electrode sizes (Fig. 3.4). This indicates that most of the electrode widths that we have considered result in a dominant Faraday inductance in copper. In fact, only the copper CPS with the narrowest width, $w = 50$ nm, exhibits a clearly dominant kinetic inductance while the $w = 100$ nm CPS lies on the threshold that was predicted by Eqn. 3.8.

The high frequency boundary of the LC region in nanoscale transmission lines is determined by a different set of mechanisms than in micro and macroscale transmission lines. In copper and other metals, for frequencies below their intrinsic scattering rate, γ the skin depth is collisional and scales as $1/\sqrt{\omega}$. However, above γ the skin depth converges to a fixed value, which is known as the collisionless or surface-wave skin depth [53]. In copper transmission lines with electrode sizes below 100 nm, no skin effect is observed (Fig. 3.6b), and the kinetic LC region extends into the plasmonic regime at optical frequencies.

In nanoscale graphene lines, the upper frequency limit for the LC region is not defined by the skin effect. At high frequencies, the self-capacitance introduces significant intra-electrode fields and lateral currents. This effect is similar to the transition between metal optics and plasmonics in metallic nanostructures [53]. This so-called capacitive "edge effect" increases attenuation sharply beyond

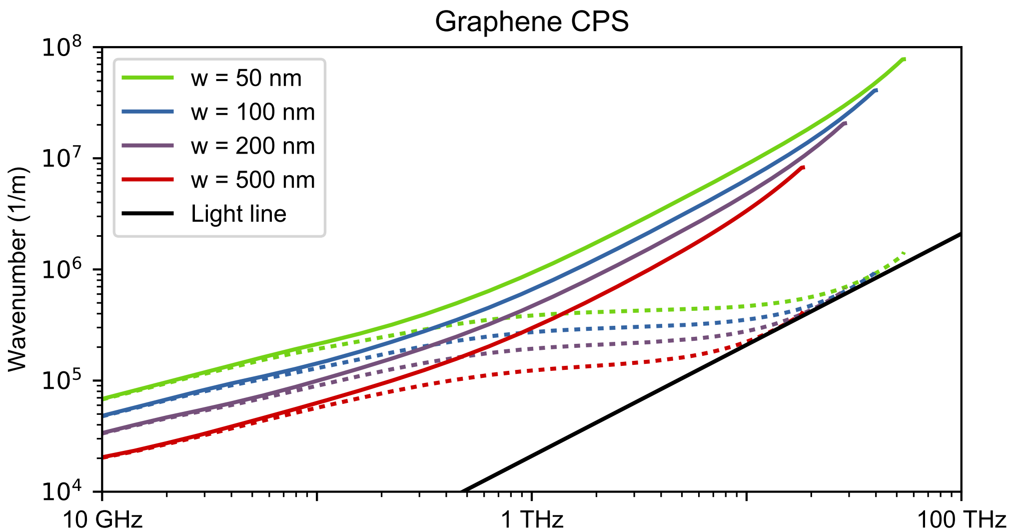

Figure 3.5: Attenuation and dispersion spectra for graphene CPS transmission lines for various conductor widths.

approximately 30 THz.

For graphene and copper (Fig. 3.6), the overall landscape of TEM wave propagation and attenuation is defined by the boundaries separating the previously unrecognized kinetic-LC region (green), the conventional RC region [61] (pink), the skin/edge effect region (yellow), and the plasmonic region [47] (blue). All of the transmission line dimensions are proportionally scaled with respect to the electrode width, along the horizontal axes, from 10 nm up to 1 cm. We reiterate that the specific value of γ or σ_0, while it can cause a spectral shift of the boundaries between different regimes, does not affect the existence of these regimes or the trends and main points presented in this chapter.

3.3.1 RC Regime

The lower bound of the LC region (the dark red curve), $\omega_{LC} = R/\left(L_F + L_K\right)$, manifests itself as a size-independent horizontal line at nanoscales, given by the conductor's scattering rate, where the kinetic inductance dominates. When the width exceeds the threshold of 100 nm for copper and 100 μm for graphene, the line becomes Faraday inductance-dominant and the LC onset is strongly width-

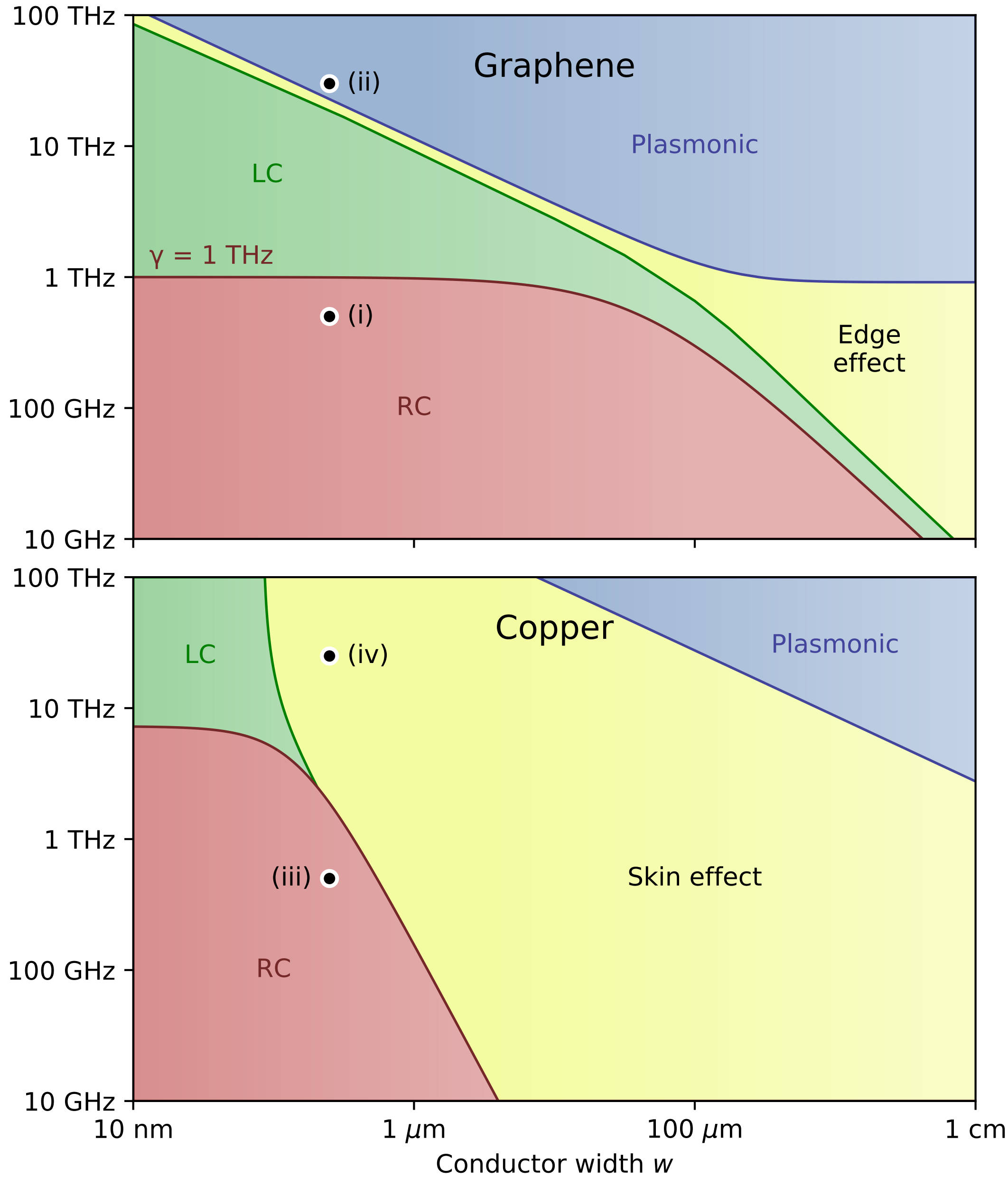

Figure 3.6: Performance regimes of graphene and copper CPS transmission lines scaled from nanoscale to macroscale. Note that the conductor separation (and conductor thickness for copper) according to $g = w/2$ and $t = w/2$. The points indicated as (i), (ii), (iii), and (iv) have their magnetic energy density and conduction current distributions shown in Fig. 3.7.

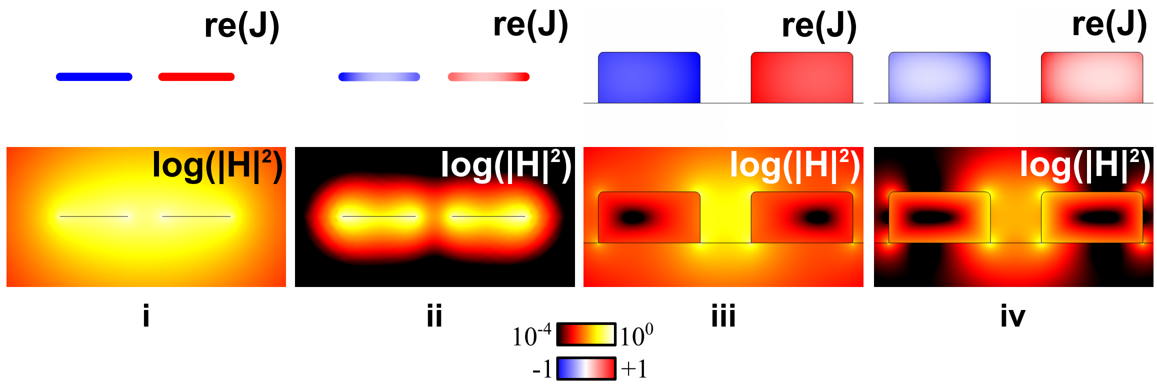

Figure 3.7: The magnetic energy density and conduction current on the graphene and copper CPS designs with w = 250 nm are plotted at 500 GHz and 30 THz (25 THz for copper), corresponding points indicated in Fig 3.6.

dependent. The slope of this transition is a function of the material dimensionality with a steeper w^{-2} dependence in the copper CPS and a more gradual w^{-1} dependence in the graphene CPS. At very low frequencies in the RC region, the current distribution is highly uniform and the mode energy is concentrated predominantly in the region between the conductors (Fig. 3.7i and Fig. 3.7iii).

3.3.2 LC Regime and the Skin and Edge Effects

The upper bound of the LC region (the dark green curve) is defined by the onset of the skin or edge effect region where the current shifts strongly towards the surface of the conductor (Fig. 3.7iv). For the copper line, this boundary is defined as the frequency at which the skin depth is equal to half of the electrode width, $\delta = w/2$. This boundary follows the same, w^{-2} geometric dependence of the LC region onset. In copper at frequencies above the intrinsic scattering rate, this boundary becomes a vertical asymptote as the skin depth converges to its constant collisionless value (Fig. 3.8). Therefore, the overall behavior of copper-based lines is characterized predominantly by the skin effect in lines with electrode widths exceeding 100 nm, and by a surprisingly large bandwidth kinetic-LC region at frequencies above the scattering rate. For graphene, the LC region transitions into the edge effect rather than the skin effect region. We define the lower boundary of the edge effect region empirically as the frequency at which the numerically computed resistance exceeds that of a spatially uniform current by 5%. This is essentially a me-

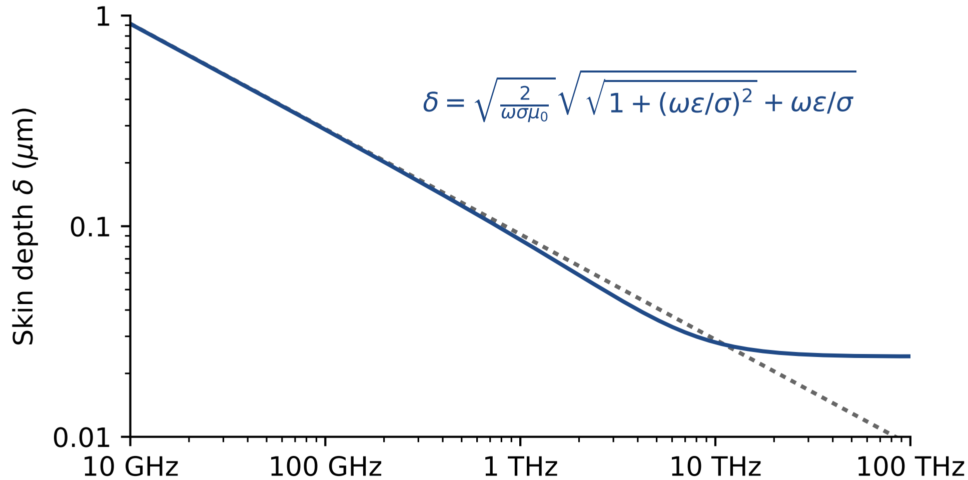

Figure 3.8: The skin depth of copper as a function of frequency. Above the scattering rate the skin depth approaches its collisionless (minimum) value [53]. The dashed line represents the low frequency approximation for the skin depth. Another way of viewing the collisionless skin depth is that because the kinetic inductive impedance exceeds the resistance above the scattering rate, current can no longer redistribute itself to minimize the overall impedance.

asure of how non-uniform the current distribution becomes. Above the graphene scattering rate, the edge effect boundary has approximately a $1/\sqrt{w}$ dependence, while below the graphene scattering rate, it closely follows the RC-LC boundary. This strongly suggests that graphene ribbons can exhibit edge-current crowding whenever their widths exceed 100 μm.

3.3.3 Plasmonic Regime

The third boundary for graphene (the dark blue curve) separates the skin and edge effect region from the plasmonic region. In the plasmonic region the transmission line becomes multi-moded since the geometry is capable of supporting individual and hybridized ribbon plasmons. For graphene, this boundary occurs when the wavelength of an infinitely-wide-graphene plasmon falls below twice the ribbon width, and runs parallel to the LC-edge-effect boundary. This implies that the observed edge effect is associated with the transition from quasi-TEM modes to ribbon plasmons where the field concentrates highly on the graphene and the current becomes non-uniform (Fig. 3.7ii). In the macroscale graphene lines that we consider (Fig. 3.6, right), this cutoff approaches a frequency nearly equivalent to the graphene intrinsic scattering rate. In general, however, this asymptotic value will be influenced by the magnitude of graphene's conductivity through its Fermi level. In Fig. 3.6, the horizontal portion of the boundary overlapping with the scattering rate is coincidental.

In copper, the cutoff for guided plasmonic modes lies at much higher frequencies for a given waveguide size, or much larger waveguide sizes at a given frequency, due to copper's larger DC conductivity. However, at microwave frequencies, the more practical boundary is the one that separates single-mode (TEM) operation form multi-mode (TEM and TE/TM) operation.

3.3.4 Comparison of Copper and Graphene Designs

If we contrast the overall performance of graphene transmission lines to their copper counterparts, we observe that graphene lines can provide a much lower onset frequency for the kinetic LC region. Furthermore, graphene's LC region is supported in much larger lines, up to widths of about 100 μm. For larger structures, graphene's reduced dimensionality also results in a more gradual shift towards a Faraday inductance-dominated LC response.

High quality graphene with a sub-THz scattering rate would be extremely valuable for realizing nanoscale traveling-wave transducers and sensors, which would otherwise be in the RC region with 3D conductors. On the other hand, when the absolute lowest attenuation is desired and dispersive attenuation can be tolerated, copper (and other metal) transmission lines are more preferable. Multilayer graphene can be used to reduce attenuation, but will also present a reduced kinetic inductance; multilayer graphene transmission line performance will scale similarly to 3D copper. Finally, it's worth noting that at conductor sizes below 100 nm, copper lines will suffer from a reduced conductance due to scattering at grain boundaries and surface roughness [62]. These effects have been partially accounted for in this analysis through a reduced copper DC conductivity of 2×10^7 S $\cdot$ m. Graphene will also encounter deviations from the Drude model in sub-100 nm widths through contributions from conducting edge modes and changes in the electronic bandstructure. Although these effects are expected to shift the propagation-constant spectra, the overall propagation regimes depicted in Fig. 3.6 and the existence of a constant-attenuation LC region remain unchanged.

Finally, it is worth pointing out that in comparison to graphene plasmons, which are known for their exceptional wavelength reduction [48], [49], the TEM modes of a graphene transmission lines exhibit even greater wavelength reduction in the few-THz frequency range (Fig. 3.5a). The dispersion relation of a graphene plasmon [50] suggests a low-frequency radiative cutoff (e.g. 1.5 THz for $E_F = 0.4$ eV, see Fig. 3.5), while the TEM mode remains guided throughout the entire spectral range. Finite-width graphene ribbons support plasmons possessing even larger β than those of the infinitely-wide graphene films, and therefore experience even higher cut-off frequencies. Thus, in the spectral range between 1 and 10 THz, the graphene TEM mode provides the optimal combination of wavelength-reduction, linear phase propagation, and constant attenuation.

3.4 Discussion

In conclusion, our analysis of graphene and copper transmission lines has revealed that the well-known TEM modes enjoy a previously unnoticed broadband constant-attenuation regime, when the lateral dimensions are reduced to the nanoscale for both 2D and 3D conductors. This so-called kinetic-LC regime is induced by a predominant kinetic inductive impedance. The threshold dimension for this regime in a 3D line is defined by the collision-less skin depth of the conductor, about 100 nm for copper. Graphene transmission lines are remarkable in that their kinetic-LC region extends to relatively large micron-scale widths. The onset frequency of the kinetic-LC region is fixed at the free-carrier scattering rate, a material property, and therefore high-quality graphene with a low scattering rate would be desirable for THz/sub-THz applications. The upper frequency cutoff, on the other hand, depends on the material dimensionality: 2D graphene lines exhibit a width-dependent upper cutoff induced by plasmonic edge effects, whereas 3D lines have no upper cutoff in the spectral range in which the Drude model is valid. Although graphene lines exhibit constant attenuation at larger dimensions, copper lines of comparable widths provide lower attenuation. However, graphene's large kinetic inductance drastically reduces the mode wavelength by $10\times$ to $40\times$, approaching 1 μm at 10 THz. This deep subwavelength operation and the inherent tunability of graphene open up new opportunities for conventional signaling and sensing applications, as well as emerging applications involving metamaterials.

Chapter 4

Sub-Diffraction Graphene Photonic Crystals *

During the past two decades, photonic crystals have revolutionized the field of nanophotonics, as their periodically modulated structure gives rise to a wide range of unprecedented phenomena in manipulating the flow of light [63], [64]. Photonic crystal slabs [65]–[67], in particular, have emerged as one of the most practical variety of photonic crystals because their 2D periodicity and planar structure is highly compatible with standard lithographic fabrication processes [68], [69].

Unfortunately, a fundamental limitation of photonic crystal slabs is that their periodicity is proportional to the operating free-space wavelength. This translates to device sizes and mode volumes that are only slightly below the diffraction limit, even when materials with a high refractive index are used. In a silicon photonic crystal slab for instance, the lattice constant defining the in-plane periodicity is generally only about 0.30 to 0.40 times the free space wavelength [63], [65]. Additionally, because total internal reflection provides the out-of-plane confinement, only an incomplete band gap is obtained due to the presence of radiation modes that extend above and below the slab. The size of the in-plane photonic band gap is also significantly reduced from that of a purely 2D crystal, because of the incomplete overlap between the Bloch mode and the slab. Additionally, out-of-plane radiation losses limit the quality factor of point-defect resonators [70]. Thus, an alternative means to further the wavelength reduction and out-of-plane light confinement is highly desirable for miniaturization and system integration.

One well-known solution for improved confinement is to employ a 3D structure that is uniform in the out-of-plane direction and sandwiched between two truncated reflecting boundaries, which are closely spaced such that only the lowest-order mode with a pure polarization is supported (e.g. the TM polarization with electric fields out-of-plane when perfect electrical conductors are used). Widely exploited in microwave photonic crystals, this approach has been realized by sandwiching a 2D slab between two metal plates that form a parallel plate waveguide

*A subset of the work discussed in this chapter is published in Ref [3]. I.W. performed the analytical and numerical modeling using the computational framework for the dispersive graphene model developed by S.H.M.

[71], [72]. As we have shown in the previous chapter, in the terahertz spectrum graphene supports a similar quasi-TEM mode that is largely confined between the two sheets [73] with a wavelength that is over 40 times smaller than in free-space [44].

In this chapter we examine this combination to realize extremely subwavelength guided Bloch modes with strong out-of-plane confinement. Two parallel graphene sheets are necessary, and they behave very differently from photonic crystal slabs interfacing with only one graphene sheet [74], or 1D photonic crystals where graphene is used for absorption [75] and magneto-optical effects [76]. Additionally, the graphene parallel plates we consider are continuous and have no spatial modulation, unlike systems with isolated graphene islands arranged in 2D patterns to modify the photonic band structures [77], [78] or to enhance absorption [79]–[81]. Also, the extreme wavelength reduction and the TM-like mode profile are absent from previous work in integrating graphene sheets with photonic crystal slabs at infrared or visible frequencies, to realize tunability [82], [83] and nonlinearity [84], and to dissipate heat [85].

4.1 Photonic Band Structure

The structure we consider is a triangular lattice of silicon rods ($\epsilon_r = 11.67$) [86] embedded in a low index material ($\epsilon_r = 2.25$). An exploded schematic of the system is shown in Fig. 4.1a where the in-plane periodicity, a is 300 nm and the slab thickness, g is 40 nm. In this chapter we focus on graphene with a Fermi level exceeding 0.1 eV, and a scattering rate of 0.4 meV [49] with a Drude conductivity given by Eqn. 3.1 (Fig. 3.2, low frequencies).

Numerical modeling confirms that the mode profile of the graphene-cladded photonic crystal slab is very close to that of a 2D crystal [63]. Fig. 4.1b shows the magnitude of the electric field across two orthogonal planes cutting through the symmetry planes of the 3D unit cell. We first observe in the vertical cut (Fig. 4.1b, left) that the majority of the mode is concentrated within the slab and between the graphene sheets. It is also apparent that the magnitude of the field between the sheets is nearly uniform in the vertical direction which agrees with the predicted behavior of the TEM mode (which also has negligible in-plane electric field components). Furthermore, we see in the horizontal cut midway through the slab (Fig. 4.1b, right), that the mode pattern resembles the unit-cell field pattern for the lowest band of a purely 2D TM crystal, in which an increased field concentration is encountered in the high-index silicon rod.

Remarkably, the calculated band structure in Fig. 4.1c shows that the addition of the graphene opens up a wide band gap in a slab that would be otherwise too thin to support any gap. In fact, the relative size of the gap for the TEM mode is nearly equal to that of the 2D TM band gap, which is approximately 28%. In principal, the graphene-cladded photonic crystal slab can replicate any feature of the purely 2D band structure, including a second photonic band gap (which occurs at higher frequencies). However, a larger refractive index contrast between the rod and cladding materials is be needed to support a second band gap. Simply replacing the oxide cladding with air to leave free-standing silicon rods may increase fabrication complexity, thus a square lattice of air holes in silicon may be a better approach for obtaining a second band gap.

A notable feature of the graphene-cladded photonic crystal slab is that the lattice constant and Bloch modes have a spatial scale that is nearly 100$\times$ smaller than the free space wavelength. With our chosen lattice constant of 300 nm, the normalized frequency 0.01 (c/a) corresponds to 10 THz, i.e. a free-space wavelength of 30 μm. In other words, the guided THz photons are comparable in size to an ultraviolet photon. The graphene separation in this case is three orders of magnitude smaller than the free-space wavelength which ensures that higher order parallel-plate-waveguide modes can be neglected. If we take graphene's resistive losses into account, we observe that these extremely subwavelength modes actually have significant propagation lengths (Fig. 4.1d), and can easily reach tens of lattice constants. Across the entire Brillouin zone, the propagation length is approximately inversely proportional to the graphene scattering rate [87], with a more significant reduction occurring in the vicinity of the band edge where mode's group velocity is reduced. The variation in the graphene scattering rate from 0.4 to 2.0 meV shown in Fig. 4.1d does not modify the band structure form what is shown in Fig. 4.1c.

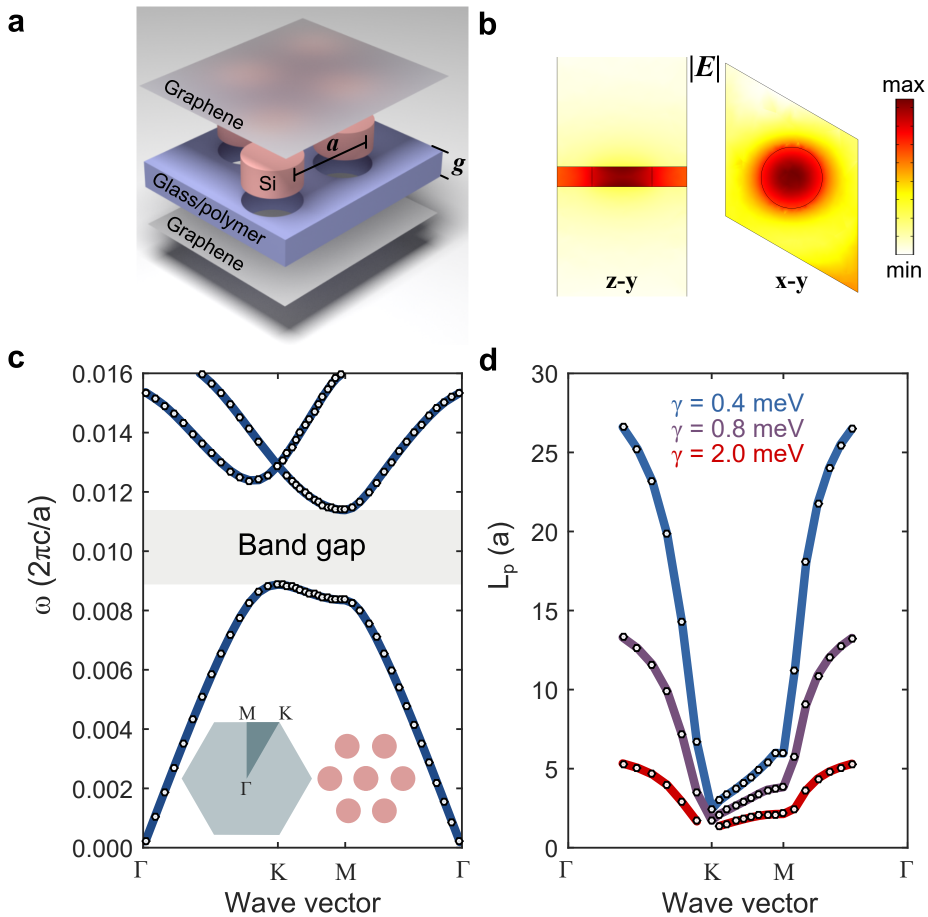

Figure 4.1: (a) Exploded 3D schematic of two single-layer graphene sheets sandwiching a segment of photonic crystal slab, consisting of silicon rods ($r = 0.2a$, $\varepsilon_r = 11.67$) in a triangular lattice embedded within a low-index material ($\varepsilon_r = 2.25$). (b) Electric field magnitude of a mode at a normalized frequency of 0.007 (c/a) on two mirror-symmetry planes in a unit cell. (c) Calculated 2D band structure along the irreducible Brillion zone boundary, with a TEM band gap (shaded in grey) from approximately 0.009 (c/a) to 0.011 (c/a). The left inset depicts the 2D Brillouin zone of the triangular crystal lattice. (d) Propagation length of the 1st bulk band for several graphene scattering rates. Throughout this section, we use the following parameter values (unless otherwise noted): $E_F = 0.4$ eV, $\gamma = 0.4$ meV, $a = 300$ nm, $g = 40$ nm.

4.2 Slab Thickness Tuning

An unusual consequence of the introduction of graphene to the photonic crystal slab is that reducing the slab thickness causes a downward shift in the photonic band gap frequency range with an increase in its relative size. A large band gap is generally preferable in photonic crystal devices, because it translates to a smaller footprint from tighter field confinement, broader operational bandwidth, and stronger spatial and temporal dispersion. The thickness dependence of the gap size is shown in Fig. 4.2a where we have considered only the Γ-K and Γ-M segments of the irreducible Brillouin zone boundary because these segments define the lower and upper edges of the first band gap, respectively. The TEM band gap corresponds to the overlap between the Γ-K and the Γ-M stop gaps which is highlighted in Fig. 4.2b. This scaling behavior is in stark contrast to the trend observed in index-guided photonic crystal slabs, where in slabs with thicknesses below one half the lattice constant ($g = a/2$) the modes become very weakly guided. In such index-guided structures this is observed in the band diagram with the bands shifting to higher frequencies and the band gap closing-off (if the dielectric modulation is even strong enough to support a band gap). However, in the graphene-cladded slab, the reduction in slab thickness translates to an increase in the capacitance experienced by the underlying TEM mode, which in turn, shifts the band gap to lower frequencies and enlarges its relative size as shown in Fig. 4.2b and Fig. 4.2c. We map the location and size of the band gap as a function of thickness from approximately $g = 0.05a$ to $g = 1.25a$, where a = 300 nm. The minimum slab thickness considered in this range is approximately 13 nm. Fig. 4.2c shows that the relative size of the gap approaches an upper limit corresponding to the size of the band gap in the purely 2D system (approximately 28%). This relatively large band gap is made possible only by the introduction of graphene. In this frequency range, an identical photonic crystal slab without the graphene cladding will only support weakly guided modes with fields that extend above and below the slab and no photonic band gap.

The unique scaling behavior of the graphene-cladded slab can be explained by considering the distributed circuit model for the TEM mode, which is valid in the limit that the slab thickness is small compared with the in-plane lattice constant. The parallel capacitance between the graphene sheets is inversely proportional to

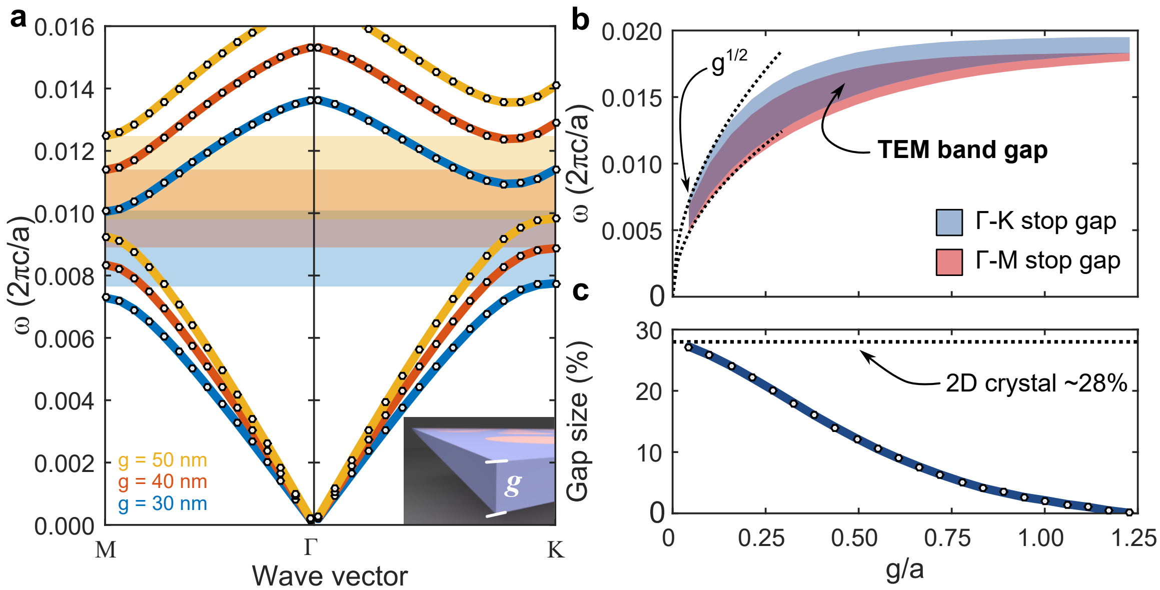

Figure 4.2: (a) Bulk bands in Γ-M and Γ-K directions for several thicknesses with the TEM band gaps shaded. (b) The Γ-K stop gap, Γ-M stop gap, and TEM band gap frequency range are shaded as a function of the slab thickness. (c) Relative size of the band gap approaches that of the purely 2D crystal at small slab thicknesses and decreases significantly for larger thicknesses.

g, whereas the kinetic inductance is independent of g. Since the transmission line circuit model predicts that the effective index of the bulk bands is proportional to $\sqrt{LC}$, the frequency of the band structure scales as $g^{1/2}$. We confirm that this is the case with the two dotted curves below $g/a \approx 0.125$ in Fig. 4.2b, which each correspond to fits to functions of the form, $f(g) = C_0\sqrt{g}$. In the regime where the thickness is on the same order of magnitude as the lattice constant, the underlying mode becomes only quasi-TEM, and can have substantial in-plane electric field components. As the thickness continues to increase, the mode will become less uniform between the sheets and will tend to concentrate in the vicinity of the graphene sheets. At large thicknesses, the mode will no longer "feel" the intermediate photonic crystal which results in a reduced band gap. This is precisely what we observe in Fig. 4.2b and 4.2c above $g/a = 1.00$. In general, this thickness tuning has no precedent in all-dielectric photonic crystal slabs and may prove to be useful for the miniaturization of THz photonic circuits as it eliminates a fundamental field-confinement penalty on ultra-thin planar devices.

4.3 Fermi Level Tuning

Since the optical conductivity of graphene is electrostatically tunable [88], [89], the band structures of the graphene-cladded photonic crystal slab can be proportionally scaled by varying the graphene Fermi level. Here we consider the graphene-cladded slab with a thickness of 40 nm and plot the first two bands under three Fermi levels: 0.25, 0.40, and 0.55 eV, in Fig. 4.3a where, again, we have only considered the Γ-K and Γ-M directions. Larger Fermi levels proportionally shift the overall band structure, including the band gap, to higher frequencies as shown in Fig. 4.3b. Remarkably, the relative size of the band gap remains unchanged, as shown in Fig. 4.3c, at approximately 25% for the entire range of Fermi levels considered here. This scaling behavior is consistent with the kinetic inductance's dependence on the Fermi level through the imaginary part of the surface conductivity, $\mathrm{Im}\left(\sigma^{-1}/\omega\right) = \pi\hbar^2/e^2E_F$.

Experimentally, graphene's Fermi level has been demonstrated [58], [90] to be continuously tunable from -1 eV to 1 eV via electrostatic gating, although the Drude model becomes inaccurate with very small absolute values of the Fermi level [90], i.e. $|E_F| < 0.05$ eV. In the context of wavelength reduction, lowering the Fermi levels may appear to be desirable, because of the resultant decrease in band frequencies. However, smaller values of E_F are in fact associated with larger ohmic losses. Therefore, attenuation-limited applications will impose a lower limit on the Fermi level.

Scaling the photonic band structure with the Fermi level represents a means for dynamically tuning the system after fabrication. Even though graphene-cladded photonic crystal slabs can be designed in a wide frequency range by proper choices of lattice constant and slab thickness, these geometric parameters are fixed upon fabrication. On the other hand, electrostatic gating can be performed and tuned after fabrication, using either an electrostatic field applied via external gating structures [82], [83] or a bias applied across the two parallel graphene sheets [91].

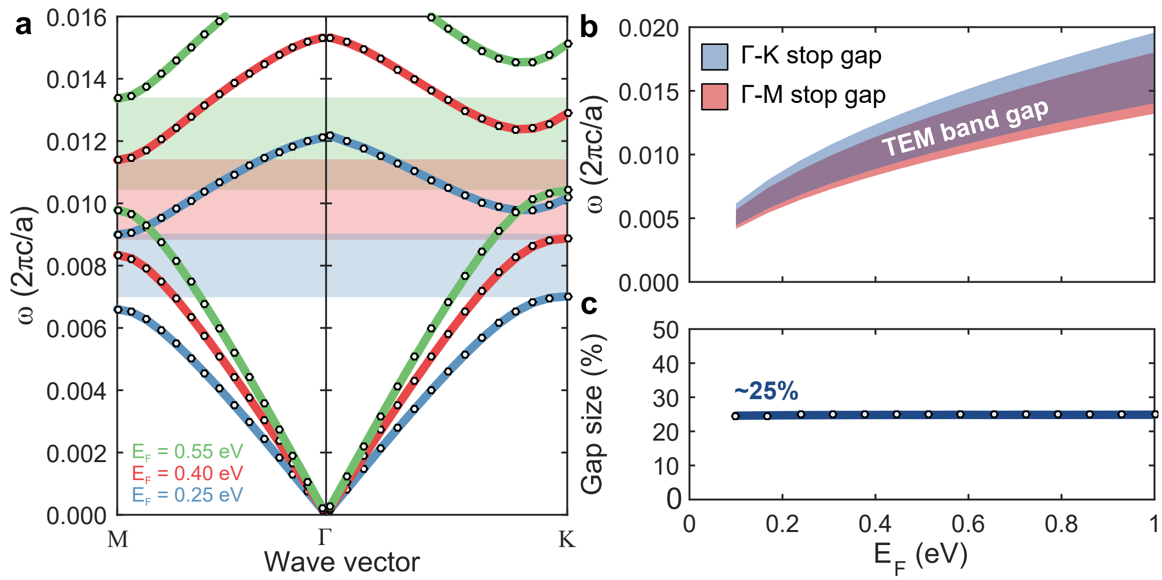

Figure 4.3: (a) Bulk bands in Γ-M and Γ-K directions for several Fermi levels with the TEM band gaps shaded. (b) The Γ-K stop gap, Γ-M stop gap, and TEM band gap frequency range are shaded as a function of the graphene Fermi level. (c) Relative size of the band gap as a function of the graphene Fermi level.

4.4 Scale Invariance

An important consideration is whether the graphene-cladded photonic crystal slab exhibits scale invariance in the presence of graphene's dispersive Drude conductivity, which is quite different from the constant permittivity assumed in dielectric photonic crystals. At first glance, one may expect this to render our use of normalized frequencies and wave vectors invalid, however we will show that this is not necessarily the case. In the first row of Fig. 4.4, we plot the Γ-K stop gap, the Γ-M stop gap, and the TEM band gap of the graphene-cladded slab structure as a function of the in-plane lattice constant, a. The three columns correspond to a different slab thickness: $g = 40$ nm, 80 nm, and 120 nm. The second row of Fig. 4.4 plots the relative size of the TEM band gap for the corresponding structure in the first row, also as a function of the in-plane lattice constant.

Among the three slab thicknesses and across the range of in-plane lattice constants, we see the emergence of two distinct regimes. The first regime corresponds to the lattice constant being on the same order of magnitude as the thickness (the left-most portion of each column), while the second regime corresponds to the lattice constant being much larger than the thickness (the right-most portion of each column). Indeed, this is an expanded picture of our earlier observation and discussion of the band gap's dependence on slab thickness; now we're also considering variation of the in-plane lattice constant. To better understand the differences between these two regimes, we plot the electric field magnitude over a plane through the 3D unit cell of two specimens in the bottom row and middle column of Fig. 4.4. What we observe in the field profile confirms our earlier conclusion: when the thickness is on the order of the lattice constant, the field can become very non-uniform (left inset) and when the thickness is much smaller than the lattice constant, the field is highly uniform in the vertical direction (right inset). These results suggest that when the lattice constant is large relative to the thickness, the graphene-cladded slab will exhibit scale invariance with respect to its in-plane lattice constant, manifested as the horizontal band of the shaded regions in the first row of Fig. 4.4.

Although the band gap for the TEM mode discussed so far is not a complete band gap in the strictest sense, practically it functions as a complete band gap for point and line defects, provided that the z-reflection symmetry is preserved. Only two additional modes traverse the TEM band gap: the light cone which is tightly compressed to the Γ point, and the 2nd-order graphene ribbon plasmon [48], which has a field distribution with the opposite symmetry along the z direction to that of the TEM mode.

In-plane imperfections, such as offsets and roughness, do not break the z-reflection symmetry and thus do not couple the TEM modes with the 2nd-order graphene ribbon plasmons. Radiation from the TEM photonic crystal slab modes into the light cone is also suppressed for two reasons: the fields of the slab modes are tightly confined between the graphene sheets (Fig. 4.4), particularly at small g; the extreme subwavelength nature of the mode results in typical fabrication roughness being far smaller ($1000\times$ or more) than the free-space wavelength, causing them to be extremely inefficient dipole radiators. Thus, for practical purposes the TEM mode band gap can be considered a "complete" band gap.

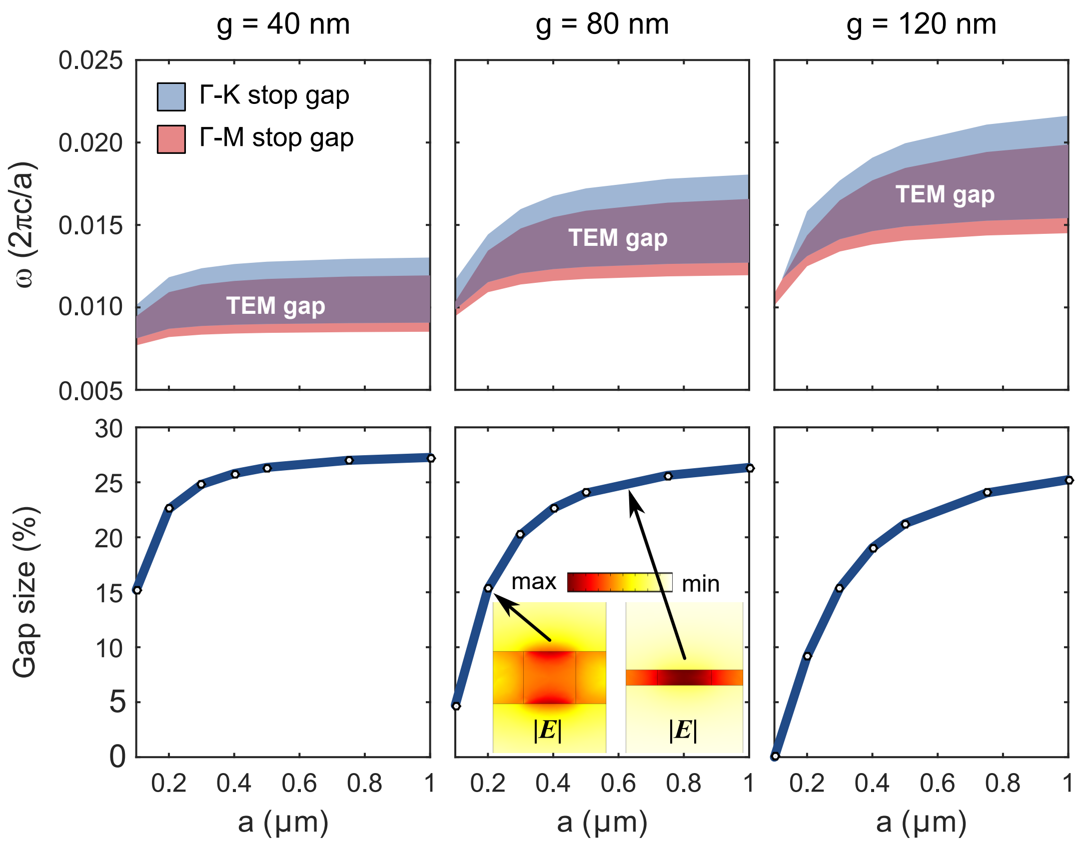

Figure 4.4: (top row) The Γ-K stop gap, Γ-M stop gap, and TEM band gap frequency range are shaded for slab thicknesses of $g = 40$ nm, 80 nm, and 120 nm, as a function of the lattice constant, a. (bottom row) The relative size of the TEM band gap as a function of the lattice constant, for the corresponding thicknesses in the top row. Inset plots show electric field magnitude over a vertical cut (perpendicular to the direction of propagation within the crystal) through the slab with lattice constant of 200 nm and 700 nm. When the lattice constant is much larger than the thickness, the bands are scale invariant and when the lattice constant is on the order of magnitude of the thickness, the field magnitude is no longer uniform in the vertical direction (shown by the left field pattern inset), and the gap bandwidth is reduced.

4.5 Line-Defect Waveguides

Similarly to purely 2D photonic crystals, the graphene-cladded photonic crystal slab can support strongly confined guided modes in defects in the bulk crystal. For example, removing a row of rods from the crystal forms a line defect of width $\sqrt{3}a$, which can be adjusted by laterally shifting the crystal cladding on either side. The dispersion for the defect modes are presented in Fig. 4.5a for several channel widths, and closely resembles those of purely 2D photonic crystals. Another similarity to the 2D systems can be observed in Fig. 4.5b, as the propagation length of the defect mode exhibits a linear dependence on its group velocity. In the widest channel considered ($w = 1.4\sqrt{3}a$) both the largest group velocity and propagation length are observed. In this case the mode can propagate for more than 18 lattice constants. This propagation length is appreciably long, in the context that the guided wavelength is a factor of 40 times smaller than in free space. Much smaller propagation lengths are observed at the edges of the defect bandwidth, which is a direct result of the mode's reduced group velocity. Just like the bulk modes, the propagation length of these defect modes is ultimately limited by the graphene intrinsic scattering rate, i.e. the quality, of the graphene. In terms of the mode profile, these defect modes are strongly confined along the in-plane directions by the band gap (Fig. 4.5c) and in the out-of-plane directions by the graphene sheets. Unlike ordinary 2D photonic crystal slabs affected by the presence of radiation modes in the substrate and superstrate, the defect modes in graphene-cladded photonic crystal slabs can easily span the entire gap range with little field leakage. At very narrow channel widths we observe a flip in the sign of the group velocity.

4.6 Numerical Modeling

All numerical results were calculated using three dimensional eigenmodal simulations performed. The eigen frequencies and the field distributions of the eigenmodes were taken from driven simulations with swept frequency and in-plane wavevector that maximize the volume-average electric energy between the graphene under constant excitation*. These results were verified with a weak form ei-

*MATLAB code available at: `https://github.com/ianwilliamson/mphdrivendispersion`

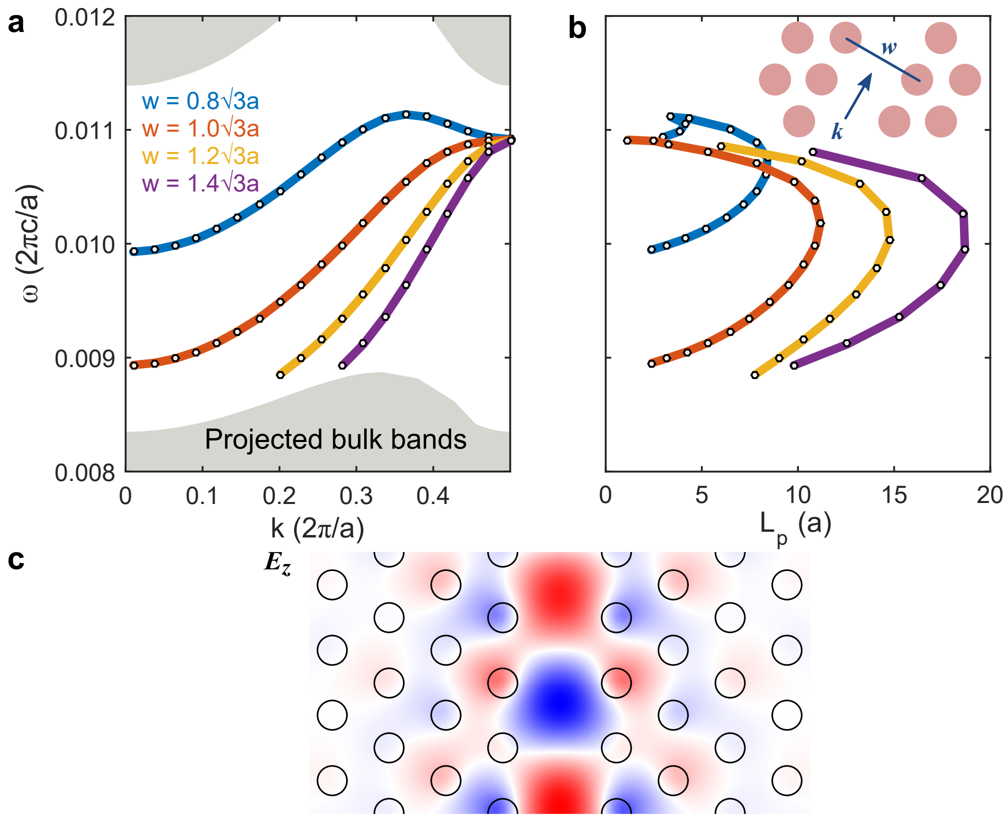

Figure 4.5: (a) Computed dispersion relation of line defects with a range of widths. Shaded regions are projected bands of the bulk crystal. (b) Computed propagation lengths. The inset depicts a schematic of the line defect. (c) Instantaneous out-of-plane electric field (E_z) of a line defect $(w = \sqrt{3}a)$ at $f = 0.0100(c/a)$.

gensolver [92] which solves for the complex-valued wavevector†. The propagation length is computed from the inverse of the imaginary part of the wavevector.

Software for extracting eigenvalue problems from COMSOL to be run in a Linux HPC enviornment was developed to perform rapid parameter sweeps of the photonic crystal structure. The details of this package are described in Appendix A.

4.7 Discussion

In this chapter we have applied graphene parallel plate waveguides to photonic crystal slabs to achieve extremely subwavelength Bloch modes with strong out-of-plane confinement. Unlike conventional all-dielectric photonic crystal slabs, the introduction of graphene facilitates the interaction of THz radiation with feature sizes that are 100 times smaller than its free-space wavelength. This length-scale reduction is sustained in slabs that have thicknesses that are 10 or more times smaller than the in-plane crystal lattice constant.

An unprecedented feature of the graphene-cladded slab is that its thickness and the graphene Fermi level strongly influence the overall photonic band structure while maintaining large band gaps. The thickness, in particular, affects both the relative size and position of the gap, which is a behavior that has no precedent in all-dielectric photonic crystal slabs. The graphene Fermi level on the other hand, uniformly tunes the band gap position while leaving the relative bandwidth unchanged for Fermi levels between 0.1 eV and 1.0 eV. This feature allows significant flexibility in band engineering, since the band gap can be tuned via chemical doping of the graphene, or via an applied electrostatic field. Furthermore, just like in purely 2D photonic crystals, line defects in the crystal of the graphene-cladded slab can support guided modes with strong in-plane confinement and propagation lengths exceeding 10 lattice constants. Ultimately, the propagation lengths of both the bulk and defect modes of the graphene-cladded slab are limited by the ohmic losses of graphene rather than to radiation in the out-of-plane direction. In this case, the graphene quality, i.e. its intrinsic scattering rate, is the key parameter for determining the attainable transmission distances, with lower scattering rates transla-

†MATLAB code available at: `https://github.com/ianwilliamson/mphmodetracker`

Reference	Materials	Scattering rate γ	T (K)	σ_0 (mS)
Yoon et al. [93]	GaAs/AlGaAs	5 GHz	4	30
Renard et al. [94]	GaAs/AlGaAs	45 THz	100	0.1
Braña et al. [95]	AlGaN/GaN	1.6 THz	13	3.2
Burke et al. [96]	GaAs/AlGaAs	1.7 GHz	0.3	500
Mittal et al. [97]	GaAs/AlGaAs	0.32 THz	0.5	11
Asmar et al. [98]	GaAs/AlGaAs	0.31 THz	4	28

Table 4.1: Comparison of experimentally measured properties of various III-V heterostructure two-dimensional electron gases (2DEG's) sorted by publication date. The phenomenological free carrier scattering rate is γ, the temperature is T, and the DC surface conductivity is σ_0.

ting to proportionally larger propagation lengths. An alternative implementation avoiding the use of graphene could use heterostructure two-dimensional electron gases (2DEG's). This approach would provide much lower scattering rates but with the trade off of a very low operating temperature to avoid phonon scattering. Table 4.1 summarizes the relevant properties of several III-V alloy heterostructure 2DEG's.

Chapter 5

Dispersive and Dissipative Optomechanics with Suspended Graphene *

In this chapter, we consider the optomechanical coupling of a graphene membrane-in-cavity system throughout the THz and mid-IR spectra, to obtain a comprehensive understanding of the influence of the optical cavity design, as well as the intrinsic absorption and dispersion of graphene. We first present a closed-form optical response of a high-Q optical cavity loaded with graphene. We then identify the conditions that maximize the optomechanical coupling coefficients and the resulting predominantly dispersive or dissipative coupling regimes at THz and mid-IR wavelengths. Taking into account the inherent optical absorption of graphene, we consider the conditions for resolved-sideband optomechanics. Together, these results point towards the optimal combinations of cavity design and graphene properties that enable various cavity optomechanical phenomena.

5.1 Optical Resonator Configuration

We consider a single-layer graphene membrane suspended within a high quality factor Fabry-Pérot cavity (Fig. 5.1), i.e. a membrane-in-cavity system [99] that has been extensively utilized in cavity optomechanics, for optomechanical cooling, displacement sensing, and dynamical back-action, as well as other effects such as giant Faraday rotation [76], [100]. An asymmetric Fabry-Pérot cavity is formed between two mirrors with complex reflection coefficients $r_1 e^{j\theta_1}$ and $r_2 e^{j\theta_2}$. Each mirror is a Bragg reflector with alternating layers of dielectric with $\varepsilon_{r1} = 21.16$ and $\varepsilon_{r2} = 2.56$ and thickness of $t_1 = 0.9$ μm and $t_2 = 1.8$ μm (Fig. 5.1). The bottom mirror has a reflection coefficient magnitude of nearly unity ($r_2 \cong 1$), making the cavity a Gires–Tournois etalon [101] that can be characterized as a one-port system in scattering-matrix formalism. Without loss of generality, we focus on the interactions between the second-order longitudinal optical mode (inset of Fig. 5.1) and

*A subset of the work discussed in this chapter is published in Ref [4]. I.W. carried out the analytical and numerical modeling using the transfer matrix model developed by S.H.M. I.W. analyzed the results with support from S.H.M.

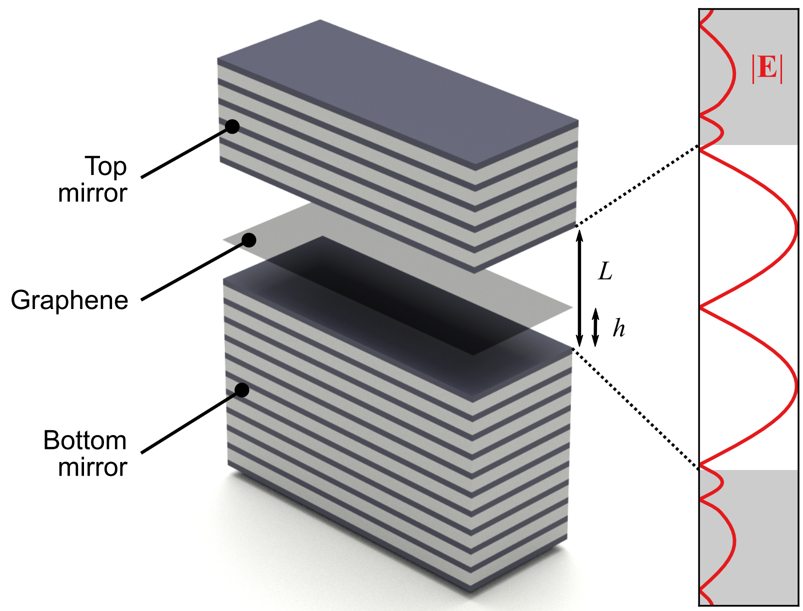

Figure 5.1: Schematic of Fabry-Pérot resonator loaded with graphene and the associated second-order cavity mode magnitude ($|\mathbf{E}|$).

suspended graphene membrane. The second-order longitudinal mode is the lowest order mode that provides a stable optomechanical equilibrium position for graphene in the center of the cavity (Fig. 5.2a), allowing the graphene to be suspended a sufficient distance away from the mirrors so as to avoid the effect of van der Waals forces [102].

5.2 Transfer Matrix Modeling

To quantify the optomechanical response of graphene, we employ the transfer matrix method [103], [104], which analytically relates the optical response of the cavity to the movement of graphene. Throughout this chapter, we refer to the optical cavity as being loaded when the suspended graphene is present or as being unloaded when the cavity is empty (equivalent to setting $\sigma = 0$). The goal of the transfer matrix analysis is to obtain an expression for the fields inside the cavity, the denominator of which, will be mapped into a complex pole whose imaginary and real components define the cavity resonance frequency and linewidth, respectively.

The transfer matrix formulation of the membrane-in-cavity system is

$$\begin{pmatrix} T \\ 0 \end{pmatrix} = \mathbf{T}_{m_2} \cdot \mathbf{T}_2 \cdot \mathbf{T}_{gr} \cdot \mathbf{T}_1 \cdot \mathbf{T}_{m_1} \begin{pmatrix} 1 \\ R \end{pmatrix} \tag{5.1}$$

where R and T represent the reflection and transmission coefficients. The mirror transfer matrix is given by

$$\mathbf{T}_m = \begin{pmatrix} -\frac{r^2+t^2}{t} & \frac{r}{t} \\ -\frac{r}{t} & \frac{1}{t} \end{pmatrix} \tag{5.2}$$

where $r = r_1 e^{j\theta_1}$ $\left(r_2 e^{j\theta_2}\right)$ and $t = t_1$ (t_2) for the front (back) mirror. Note that we don't explicitly define the phase angle of the mirror transmission coefficients (t_1 and t_2) since they do not appear in the final expression for the denominator of the cavity field amplitude. Also note that the mirrors of the cavity are symmetric, meaning that they have N_1 (N_2) periods with a single additional layer of thickness t_1. The transfer matrices for propagation between the graphene and the front mirror and the back mirror are given by,

$$\mathbf{T}_1 = \begin{pmatrix} e^{-jk_0(L-h)} & 0 \\ 0 & e^{jk_0(L-h)} \end{pmatrix} \tag{5.3}$$

$$\mathbf{T}_2 = \begin{pmatrix} e^{-jk_0 h} & 0 \\ 0 & e^{jk_0 h} \end{pmatrix} \tag{5.4}$$

and the transfer matrix for the graphene membrane is given by

$$\mathbf{T}_{gr} = \begin{pmatrix} 1 + \frac{\sigma(\omega)}{2Y_0} & \frac{\sigma(\omega)}{2Y_0} \\ -\frac{\sigma(\omega)}{2Y_0} & 1 - \frac{\sigma(\omega)}{2Y_0} \end{pmatrix} \tag{5.5}$$

where the conductivity $\sigma(\omega)$ is given by the full expression that incorporates both the Drude and interband contributions from Eqns. 3.1 and 3.2 (Fig. 3.2). The forward (a_3) and backward (b_3) propagating field-amplitudes at the inside interface of the front mirror are given by

$$\begin{pmatrix} a_3 \\ b_3 \end{pmatrix} = \mathbf{T}_{m_1} \begin{pmatrix} 1 \\ R \end{pmatrix} \tag{5.6}$$

which can be evaluated by first solving Eqn. 5.1 for R. The denominator of the expressions for a_3 and b_3 is given by,

$$1 - r_1 r_2 e^{-2j(\eta_1+\eta_2)} + \frac{\sigma}{2Y_0}\left(1 + r_1 e^{-2j\eta_1}\right)\left(1 + r_2 e^{-2j\eta_2}\right) \tag{5.7}$$

which can be mapped into a complex pole of the form, $j\left(\omega - \omega_0'\right) + \Gamma'$ where ω_0' and Γ' correspond to the loaded cavity resonance frequency and linewidth. The unloaded cavity resonance frequency, ω_0 satisfies the condition, $\eta_1 + \eta_2 = m\pi$, which causes the field amplitude within the cavity to diverge for perfectly reflecting mirrors ($r_{1,2} = 1$). If we assume that the second term of Eqn. 5.7 is nearly constant in the vicinity of the unloaded resonance frequency, ω_0 then Eqn. 5.7 can be rewritten as

$$r_1 r_2 \frac{\delta\psi}{\delta\omega}\left[j\left(\omega - \omega_0\right) + \Gamma\right] + R + jI, \tag{5.8}$$

where R and I are the real and imaginary parts of the third term of Eqn. 5.7. For a high-Q cavity ($r_{1,2} \approx 1$), the expression in Eqn. 5.8 leads to

$$\omega_0'\left(h\right) = \omega_0 - \frac{2\Gamma}{1 - r_1 r_2}\frac{\mathrm{Im}\left(\sigma\right)}{Y_0}\cos^2\left(\eta_2\left(h\right)\right) \tag{5.9}$$

and

$$\Gamma'\left(h\right) = \Gamma\left[1 + \frac{2}{1 - r_1 r_2}\frac{\mathrm{Re}\left(\sigma\right)}{Y_0}\cos^2\left(\eta_2\left(h\right)\right)\right] \tag{5.10}$$

if ω_0 is near the center of the photonic band gap of the Bragg mirrors and if the quality factor of the cavity is high. Y_0 is the free space wave admittance and the linewidth of the unloaded cavity is given by [105]

$$\Gamma = \left(\frac{\partial\psi}{\partial\omega}\right)^{-1}\frac{1 - r_1 r_2}{r_1 r_2}, \tag{5.11}$$

where $\psi = 2\eta_1 + 2\eta_2$ is the round-trip phase delay between the mirrors and the graphene with,

$$2\eta_1 = 2k_0\left(L-h\right) - \theta_1$$

and $2\eta_2 = 2k_0 h - \theta_2$ where $k_0 = \omega/c$. θ_1 and θ_2 are the phase angles of the reflection coefficients of the top and bottom mirror, respectively.

Graphene's influence on the optical cavity is apparent in the reflection spectrum, where both the resonance frequency and linewidth of the cavity resonance follow sinusoidal shifts (Fig. 5.2a) with respect to the graphene suspension height h. Eqn. 5.9 reveals that when graphene is suspended at exactly the maximum of the optical mode's electric field,the cavity experiences maximal frequency detuning

$$\max\left(\Delta\omega_0'\right) = \frac{-2\Gamma\,\mathrm{Im}\left(\sigma\right)}{Y_0\left(1-r_1r_2\right)}. \tag{5.12}$$

Due to the change in sign of the imaginary part of graphene's conductivity, the induced detuning corresponds to a blue shift at THz/mid-IR frequencies and a red shift above the interband transition frequency $\omega_{inter} = 2E_F/\hbar$, which is consistent with predictions for the coupling between graphene and other types of optical resonances [106]. The maximal linewidth broadening also occurs when graphene is suspended at the maximum of the electric field (Fig. 5.2b), and is dominated by the graphene absorption

$$\max\left(\Gamma'\right) \cong \frac{c\,\mathrm{Re}\left(\sigma\right)}{Y_0 L}. \tag{5.13}$$

In contrast, when graphene is suspended exactly within the electric field null of the cavity mode, the total cavity quality factor is the same as that of the unloaded cavity, no matter how large the scattering rate of the graphene. The locations of the electric field nulls also correspond to the stable equilibrium positions of the graphene membrane in the 1D optomechanical system (Fig. 5.2a).

5.3 Optomechanical Coupling Regimes

In this section, we identify the spectral range and graphene material constants that lead to predominantly dispersive or dissipative optomechanical coupling. Other constraints, such as maintaining a high optical quality factor, which

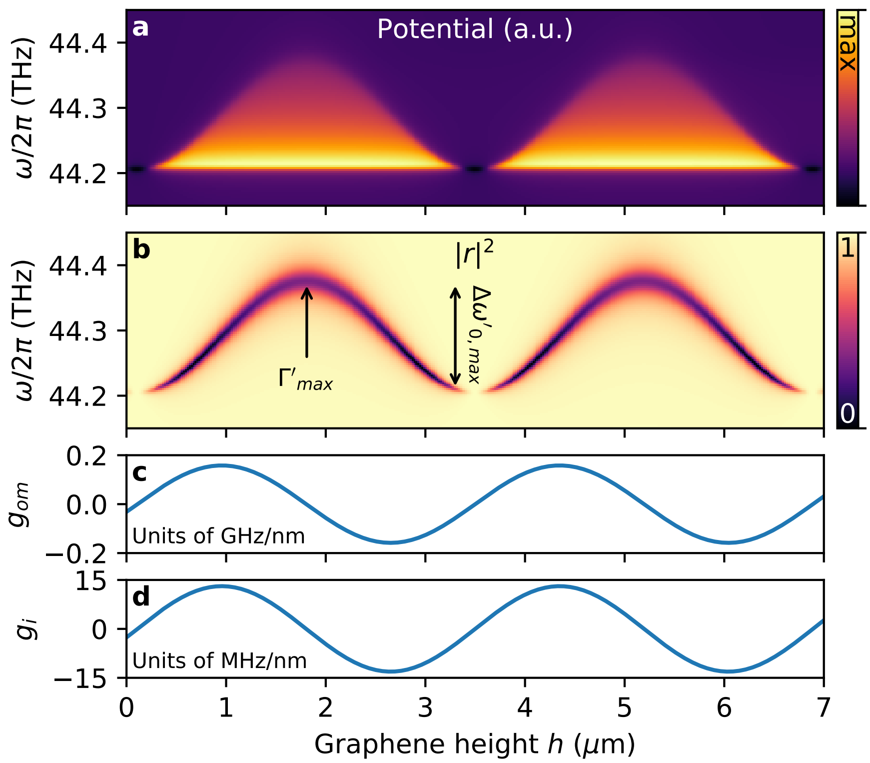

Figure 5.2: (a) Optomechanical potential and (b) power reflection coefficient of graphene membrane-in-cavity system as a function of suspension height h and excitation frequency ω. (c) Dispersive optomechanical coupling coefficient g_{om} and (d) dissipative optomechanical coupling coefficient g_i as a function of suspension height h. The cavity length is $L = 7\ \mu$m, defined by two mirrors with $N_1 = 4$, and $N_2 = 20$. Graphene is characterized at room temperature by a scattering rate $\gamma = 3$ THz and Fermi level of $E_F = 0.3$ eV.

is relevant for operating in the resolved sideband regime, will be considered in the next section. Following directly from Eqn. 5.9 and Eqn. 5.10, the dispersive and internal dissipative optomechanical coupling coefficients (Fig. 5.2c,d), are given by

$$g_{om} = \frac{\partial \omega_0'}{\partial h} = \frac{2k_0\Gamma}{1 - r_1 r_2} \frac{\mathrm{Im}\,(\sigma)}{Y_0} \sin\left(2\eta_2\right) \tag{5.14}$$

and

$$g_i = \frac{\partial \Gamma'}{\partial h} = -\frac{2k_0\Gamma}{1 - r_1 r_2} \frac{\mathrm{Re}\,(\sigma)}{Y_0} \sin\left(2\eta_2\right). \tag{5.15}$$

All quantities are frequency-dependent through σ and the free-space wave number k_0. g_{om} and g_i also have the same dependence on the graphene height h (shown in Fig. 5.2c,d), implicitly through η_2 and the optical cavity properties. Both coupling coefficients are inversely proportional to the cavity length and increasing the optical quality factor of a high-Q cavity ($r_{1,2} \approx 1$) does not change $\max\left(|g_i|\right)$ or $\max\left(|g_{om}|\right)$ because the unloaded linewidth Γ scales proportionally with the term $(1 - r_1 r_2)$ (Fig. S4). g_{om} and g_i differ only by the imaginary part and the real part of σ. Note that the expressions for the coupling coefficients in Eqn. 5.14 and Eqn. 5.15 are similar to those describing an optical cavity coupled to a subwavelength nanomechanical bar [104], except that in our derivation graphene is accurately modeled as an infinitesimally thin conducting surface. The maximum values of g_{om} and g_i for a given cavity, as a function of unloaded cavity resonance frequencies, which is very close to the operating frequency, as well as the Fermi level and scattering rate of graphene are shown in Fig. 5.3 and Fig. 5.4.

5.3.1 Dispersive Coupling

For a fixed graphene scattering rate of 3 THz (Fig. 5.3a), two distinct regions of large dispersive optomechanical coupling emerge: a narrowband peak at the interband-transition threshold frequency ω_{inter} (white dotted line in Fig. 5.3a), and a broadband peak with its maxima approximately 50% lower in frequency (white dashed line in Fig. 2a). Except for very low doping levels (E_F < 0.1 eV), an increased doping, i.e. a higher E_F, translates to an increased dispersive optomechanical coupling, especially between 10 and 100 THz where graphene's plasmonic response becomes dominant (Fig. 5.3a). For E_F = 0.5 eV, the dispersive coupling peaks at approximately 2 GHz/nm for the high-frequency narrowband region (inset of Fig.

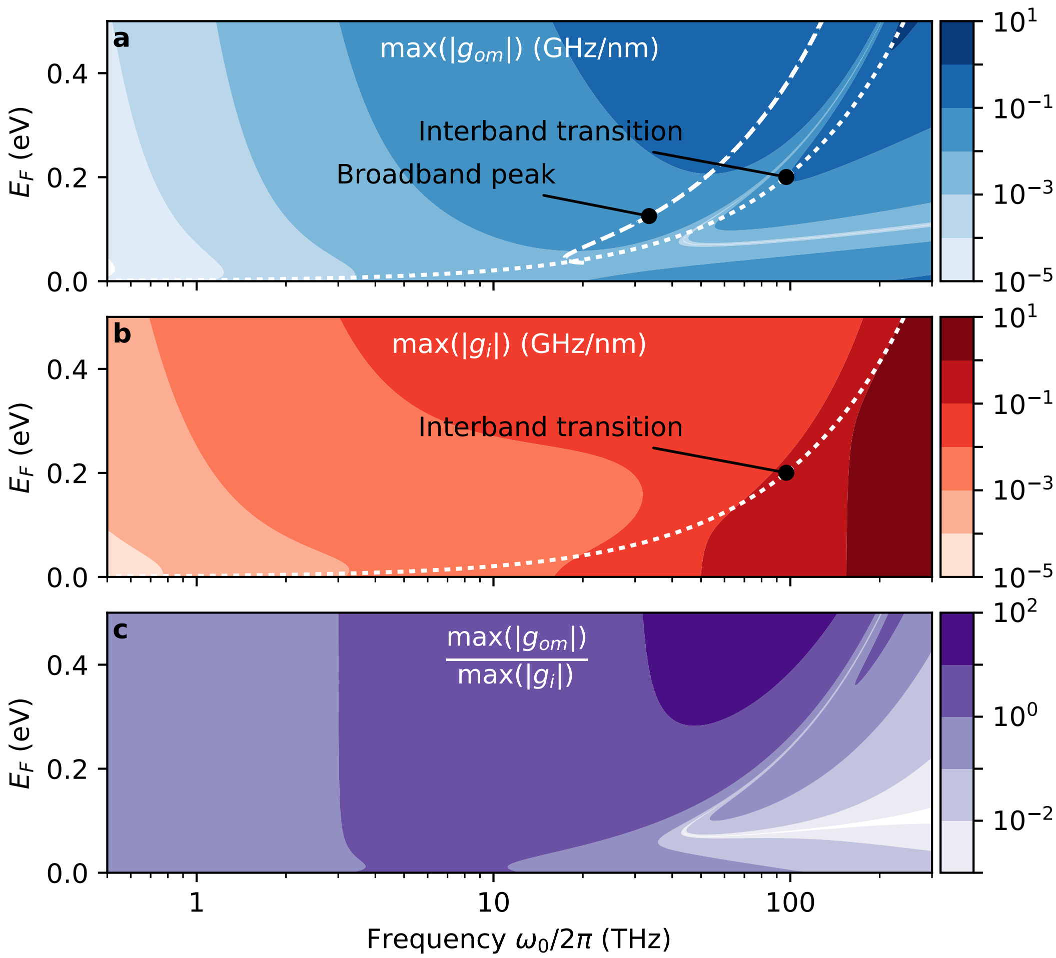

Figure 5.3: (a) Maximum $|g_{om}|$ and (b) $|g_i|$ for a range of optical cavities characterized by the unloaded resonance of the second-order mode ω_0 and for various Fermi levels E_F of graphene. (c) Ratio of $|g_{om}|$ / $|g_i|$ indicating the dispersive coupling regime ($|g_{om}|$ / $|g_i| \gg 1$) and the dissipative coupling regime ($|g_{om}|$ / $|g_i| \ll 1$).

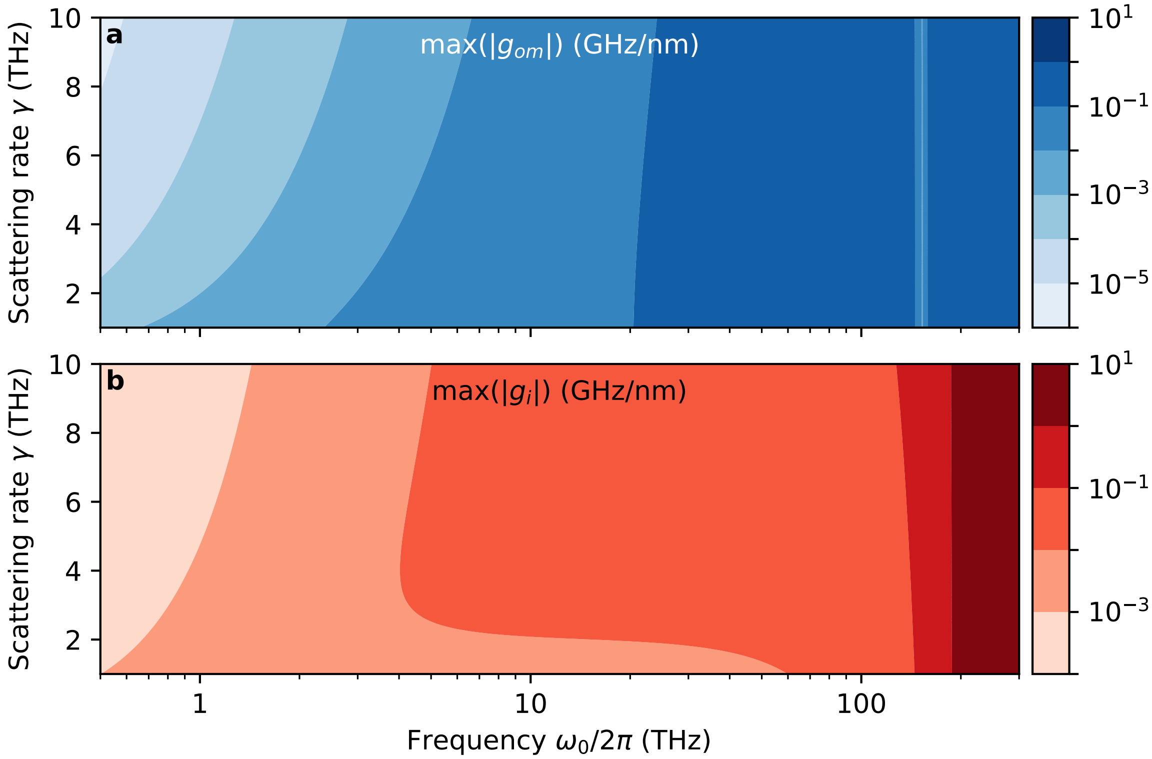

Figure 5.4: (a) Maximum $|g_{om}|$ and (b) $|g_i|$ for a range of optical cavities characterized by the unloaded resonance of the second-order mode ω_0 and for the scattering rate of graphene γ, at a fixed Fermi level of 0.375 eV.

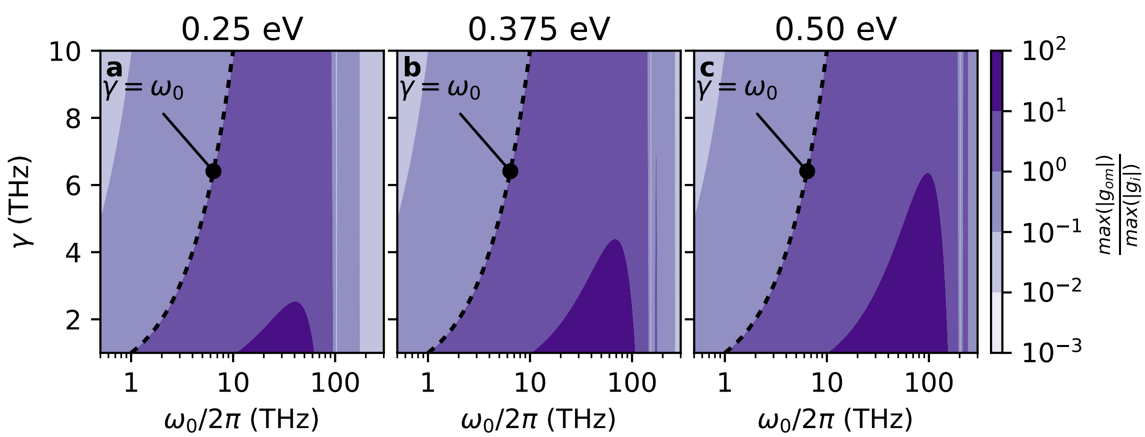

Figure 5.5: Ratio of $|g_{om}|$ / $|g_i|$ indicating dispersive coupling regime ($|g_{om}|$ / $|g_i| \gg 1$) and dissipative coupling regime ($|g_{om}|$ / $|g_i| \ll 1$) for three levels of E_F: 0.25 eV, 0.375 eV, and 0.50 eV.

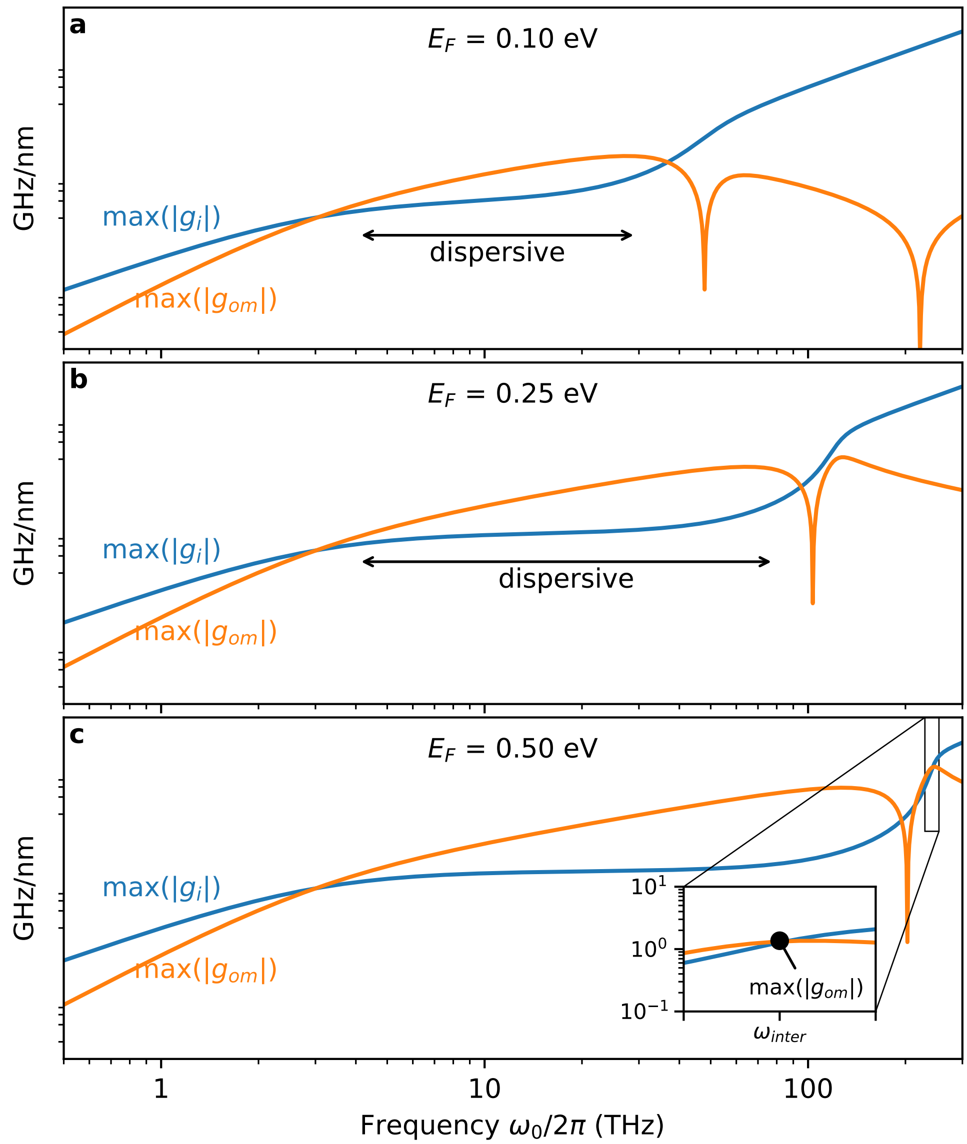

Figure 5.6: Maximum $|g_{om}|$ and $|g_i|$ at three E_F levels: (a) 0.10 eV, (b) 0.25 eV, and (c) 0.50 eV. Graphene's scattering rate in (a-c) is fixed at $\gamma = 3$ THz.

5.6c). In the lower frequency broadband region, above the scattering rate but below the interband transition frequency ($\gamma \ll \omega < \omega_{inter}$), the maximum dispersive coupling coefficient, following from Eqn. 3.1 and 5.14, is given by

$$\max\left(|g_{om}|\right) = \frac{2e^2 E_F}{Y_0 L h^2 \left(r_1 r_2\right)} \qquad \left(\gamma \ll \omega < \omega_{inter}\right), \tag{5.16}$$

which reaches approximately 0.5 GHz/nm. Such large coupling in the mid-IR represents a 1000-fold increase over previous experimentally demonstrated graphene cavity optomechanical coupling of around 0.2 MHz/nm in the near-IR [31]. The resultant vacuum optomechanical coupling coefficient g_0 for a typical [25] $x_{zpf} = \sqrt{h/\left(2m\Omega_m\right)}$ of 1.28 pm is 640 kHz, comparable to state-of-the-art on-chip cavity optomechanical systems [107]. Furthermore, g_{om} = 0.5 GHz/nm at ω_0 = 130 THz corresponds to a value approaching several percent of ω_0/λ_0. Such large coupling strengths in graphene are especially surprising considering that dispersive coupling is driven by the induced change in the effective cavity length and graphene is only a single layer of carbon atoms thick.

Despite its 75% smaller peak g_{om}, the low-frequency broadband region produces a much greater ratio between g_{om} and g_i (dark purple region of Fig. 5.3c) and a much narrower optical linewidth that make it much more experimentally favorable for cavity optomechanical phenomena which require predominantly dispersive coupling. Relatively high Fermi levels ($E_F \geq 0.25$ eV) are required to achieve a 10$\times$ contrast between dispersive and dissipative coupling (Fig. 5.3c), and at very high Fermi levels ($E_F \geq 0.45$ eV) a 100$\times$ contrast is achievable with a scattering rate as high as 6 THz. In contrast, lightly doped graphene ($E_F < 0.1$ eV) exhibits a washed-out peak that is orders of magnitude smaller. The low-frequency boundary ($g_{om} = g_i$) of this broadband dispersive-coupling region coincides with γ (Fig. 5.5).

Well above the scattering rate ($\omega_0 \gg \gamma$), g_{om} becomes largely independent of γ (vertical dark blue contours of Fig. 5.4a), and the high-frequency boundary of the predominantly dispersive coupling is linearly proportional to the Fermi level, which agrees with Eqn. 5.16. Thus, both the bandwidth and the peak coupling strength of this region benefit from simultaneously minimizing γ and maximizing E_F. Interestingly, a similar "sweet spot" in the THz spectrum has been predicted for transmission lines with broadband frequency-flat attenuation [2]. At operating frequencies below the scattering rate, g_{om} drops off quickly and g_i dominates (Fig. 5.4), which qualitatively agrees with graphene behaving as a lossy conductor in the microwave regime. Here, graphene would be more suited as an electrode in electrostatic devices [22]–[24] rather than as a reflective membrane within an optical cavity.

Near the interband transition frequency, although the dispersive coupling reaches its highest strength across all frequencies, predominantly dispersive coupling is much more challenging to realize, and is reliant on a Fermi level of at least 0.375 eV and scattering rates below 1.25 THz. As previously mentioned, this spectral range coincides with a strong absorption edge that results in an optical cavity linewidth nearly 10$\times$ greater than that of the low-frequency broadband dispersive coupling region. More problematic is a significant increase in g_i which reduces the contrast between dispersive and dissipative coupling. For relatively low doping (E_F = 0.1 eV), g_{om} never outpaces the rising g_i (Fig. 5.6a); only for sufficiently high E_F > 0.25 eV, does the ratio $|g_{om}|$ / $|g_i|$ exceed unity (Fig. 5.6b,c). In general, the ratio $|g_{om}|$ / $|g_i|$ in this narrow interband peak is highly sensitive to the scattering rate. For γ = 3 THz, the narrow interband peak has $|g_{om}|$ / $|g_i| \approx 1$ throughout the range of Fermi levels that we consider in Fig. 5.3c. For higher quality graphene (γ $\sim$ 1 THz), a 10$\times$ contrast between g_{om} and g_i can be achieved, corresponding to the narrow dark purple region in bottom right of Fig. 5.5b. Alternatively, the simultaneously large dispersive and dissipative coupling in this region can be combined to maximize the overall displacement readout sensitivity, since both types of coupling contribute to the total optomechanical gain of the system [26]. Again, maximal sensitivity relies on achieving a large Fermi level and a small scattering rate in graphene. Overall, these optomechanical coupling peaks are of practical interest given that high-power and low-noise coherent sources are available in the mid-IR region.

5.3.2 Dissipative Coupling

At operating frequencies above the interband absorption edge (to the right of the dotted line in Fig. 5.3b), dissipative coupling dominates, making graphene-loaded cavities good candidates for phenomena such as unresolved sideband cooling, photothermal backaction [108], [109], and optomechanical squeezing. Here, $|g_i|$ increases linearly with frequency and is independent of the Fermi level. The interband absorption leads to values of g_i exceeding 1 GHz/nm, while the ratio of $|g_i/g_{om}|$ rapidly reaches more than an order of magnitude (with $|g_i| \gg |g_{om}|$ in the bottom right of Fig. 5.3c). Note that this ratio is largely independent of the scattering rate at operating frequencies above the interband transition frequency (Fig. 5.5a,b,c). In particular, at moderate doping levels (i.e. E_F = 0.1 eV) the ratio of dissipative coupling to dispersive coupling can reach two orders of magnitude in the near-IR spectrum (Fig. 5.3c), while simultaneously providing g_i on the order of many GHz/nm (Fig. 5.6a). In contrast, for frequencies below the interband transition threshold (dotted line in Fig. 5.3c), predominantly dissipative coupling is difficult to realize, and high Fermi levels are required ($E_F \approx 0.5$ eV) to reach just 0.1 GHz/nm of dissipative coupling.

5.3.3 Resolved Sideband Regime

Maximum optomechanical coupling discussed requires that graphene be suspended at a height that broadens the cavity optical linewidth to half of its peak value $\Gamma'_{max}\cos^2(\pi/4) = \Gamma'_{max}/2$ (Fig. 5.2c,d). Thus, a necessary tradeoff must be made between the optical linewidth and the realized optomechanical coupling. Maintaining a cavity optical linewidth that is significantly narrower than the mechanical resonance frequency Ω_m is known as resolved sideband operation, which is important for side-band cooling, quantum state transfer, displacement detection, and parametric amplification [110]. Small optical linewidths are also crucial for minimizing optical heating of graphene. Even for high-quality graphene with $E_F = 0.5$ eV and γ = 1 THz, the peak optical linewidth is on the order of several GHz (Fig. 5.7a), which is too broad for state-of-the-art graphene mechanical resonators with $\Omega_m \sim 200$ MHz [14], [16], [21]. Fortunately, suspending graphene at heights with acceptable optical linewidths (shaded regions of Fig. 5.7a,b), with $\Omega_m/\Gamma' \geq 2$ (optical linewidths below 100 MHz), leads to a maximum g_{om} of about 0.18 GHz/nm for a cavity with $N_1 = 10$, or approximately 36% of the maximum coupling strength obtained in the unresolved sideband regime.

In general, resolved sideband operation demands the reduction of the unloaded optical linewidth to less than 1/10 of the mechanical resonance frequency.

In our cavity, this is accomplished by increasing the number of periods in the front mirror, which reduces the unloaded optical linewidth Γ. Mapping the relationship between g_{om} and the loaded optical linewidth Γ' (Fig. 5.7c) where both quantities are determined by the graphene suspension height, from Fig. 5.7a and Fig. 5.7b, illustrates the need for a smaller Γ to achieve a large g_{om} in the resolved-sideband regime. The $N_1 = 10$ configuration has an unloaded cavity linewidth almost as low as 10 MHz, which is more than an order of magnitude smaller than the mechanical resonance frequencies achieved in graphene mechanical resonators. Further decreasing the unloaded optical linewidth by using more reflective mirrors would only marginally benefit g_{om}.

In terms of material parameters, the maximally realizable optomechanical coupling in the resolved sideband regime depends strongly on the scattering rate of graphene. For a fixed Fermi level of 0.5 eV, as the impurity scattering rate is increased from 1 THz to 20 THz (Fig. 5.7d), the operating point with g_{om} = 0.18 GHz/nm, denoted (i), shifts from a linewidth of 100 MHz to 2 GHz. Resolved sideband operation requires g_{om} to be reduced to 30 MHz/nm, because greater optical absorption increases the slope of Γ' as a function of h, thereby reducing the width of the shaded region in Fig. 5.7a.

This degradation in performance for higher scattering rates is also apparent in the maximally realizable optomechanical coupling $|g_{om}\,(\Gamma' = \Omega_m/2)|$ for a range of mechanical resonance frequencies (Fig. 5.7e). Although this result confirms the general rule of thumb in cavity optomechanics involving lossy materials that minimizing absorption is the key to maximizing optomechanical coupling, even for γ = 20 THz, 10's of MHz/nm in sideband-resolved dispersive coupling can be realized. Note that, as mentioned previously, in the unresolved sideband regime a large scattering rate has a negligible impact on the maximally realizable coupling coefficient, corresponding to the approximately 0.55 GHz/nm peak values of $|g_{om}|$ in Fig. 5.7d. The larger scattering rate mostly results in greater optical heating, which limits the maximal optical power that the system can tolerate.

Irrespective of the resolved sideband regime, the single-photon (vacuum) optomechanical coupling strength g_0 of graphene compares favorably with those of other chip-scale cavity optomechanical systems (Fig. 5.8a), such as photonic crystal cavities [111]–[113] and micro-ring resonators [114] in the near-IR spectrum.

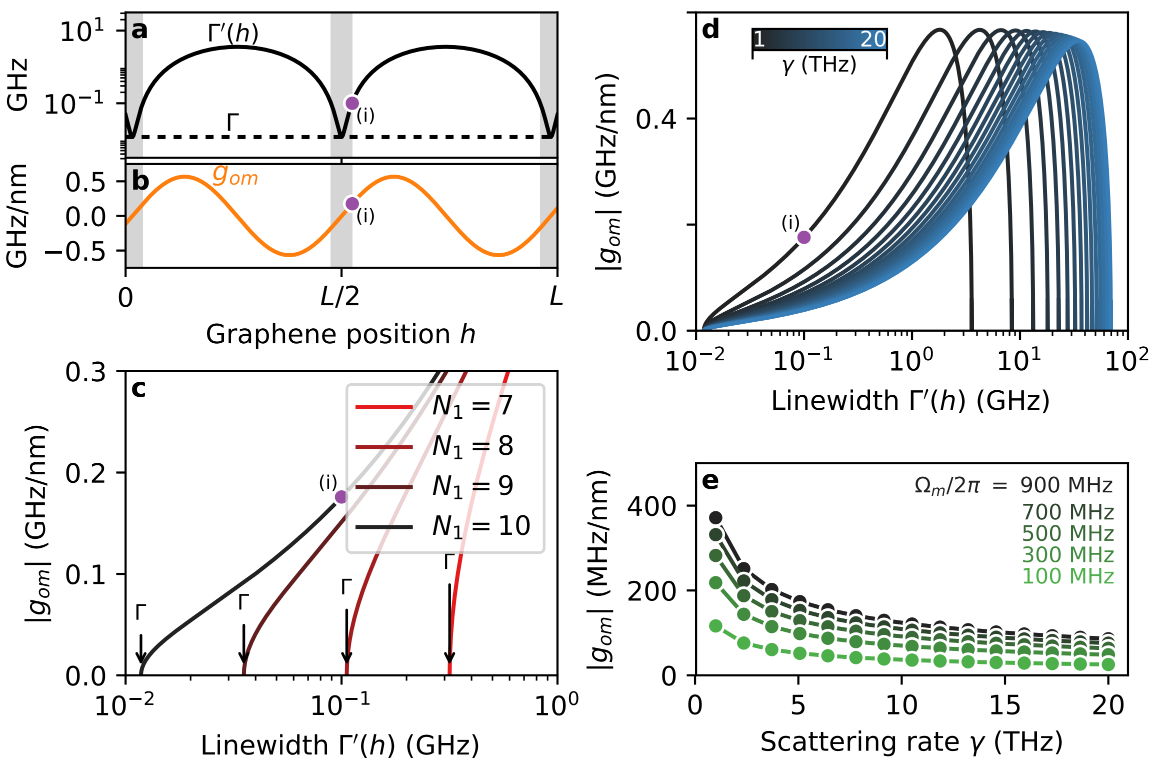

Figure 5.7: (a) Optical linewidth and (b) dispersive optomechanical coupling coefficent as a function of graphene height h. Shaded grey regions correspond to height ranges around the optical cavity mode's electric field null and where it is possible to enter the resolved sideband regime. (c) Absolute value of dispersive optomechanical coupling coefficent as a function of the optical cavity linewidth, which is implicitly dependent on the graphene height, h. Point (i) in part (a) and part (b) correspond to the x and y coordinates of point (i) in part (c). (d) Absolute value of dispersive optomechanical coupling cofficent as a function of optical linewidth for a range of graphene phenomenological scattering rates. (e) Absolute value of dispersive optomechanical coupling coefficent as a function of graphene scattering rate for several example mechanical resonance frequencies. Line series created from data plotted in panel (d) by interpolating $g_{om}\,(\Gamma' = \Omega_m/2)$ across the lines corresponding to each γ.

Assuming a mechanical resonance frequency of 100 MHz and a mass of 2 fg, and using the same cavity discussed in Fig. 5.7a and Fig. 5.7b, the purple curve in Fig. 5.8a illustrates the maximum obtainable g_0 as a function of the sideband resolution. An increased resonator mass reduces g_0 (corresponding to the shaded purple region), while a larger (smaller) mechanical resonance frequency will shift the purple region to the right (left). Additionally, smaller values of E_F shift the purple region downward, while larger values of γ shift the purple region to the left. Microwave cavity optomechanical systems, including those incorporating graphene, lie out of range to the lower right for their extremely small cavity linewidths and optomechanical coupling coefficients, both a result of the low electromagnetic resonance frequencies in microwave cavities. Moreover, the single-photon cooperativity, defined as $C_0 = 4{x_{zpf}}^2{g_{om}}^2/\left(\Gamma'\Gamma_m\right)$, which quantifies the ability of an optomechanical system to support coherent photon-phonon coupling ($C_0 > 1$), is shown in Fig. 5.8b, again for the graphene cavity discussed for Fig. 5.7a and Fig. 5.7b. A $Q_m f_m$ on the order of 10^{13}, i.e. $Q_m = 10^5$, is sufficient for enabling coherent coupling, which is nearly within reach of current graphene mechanical resonators (Fig. 1.3).

5.4 Discussion

Our analysis reveals that despite its significant optical absorption, graphene can provide large optomechanical coupling in a membrane-in-cavity system that is comparable to state-of-the-art cavity optomechanical systems [111]–[114]. For quantum-limited force and displacement readout, predominantly dispersive coupling occurs in the mid-IR frequency range, between the scattering rate and the interband transition frequency of graphene, with a strength of up to 0.5 GHz/nm in graphene with the Fermi level above 0.45 eV. Generally speaking, short cavity lengths and large Fermi levels are essential to realizing the largest dispersive coupling, while small scattering rates suppress dissipative coupling and optical heating. Surprisingly, even for graphene with a scattering rate as large as 6 THz, dispersive optomechanical coupling can dominate the dissipative coupling by more than 100-fold. On the other hand, a graphene Fermi level around 0.1 eV leads to a predominantly dissipative coupling region in the near-IR above the interband transition threshold. The contrast ratio exceeds 100-fold regardless of the scattering rate

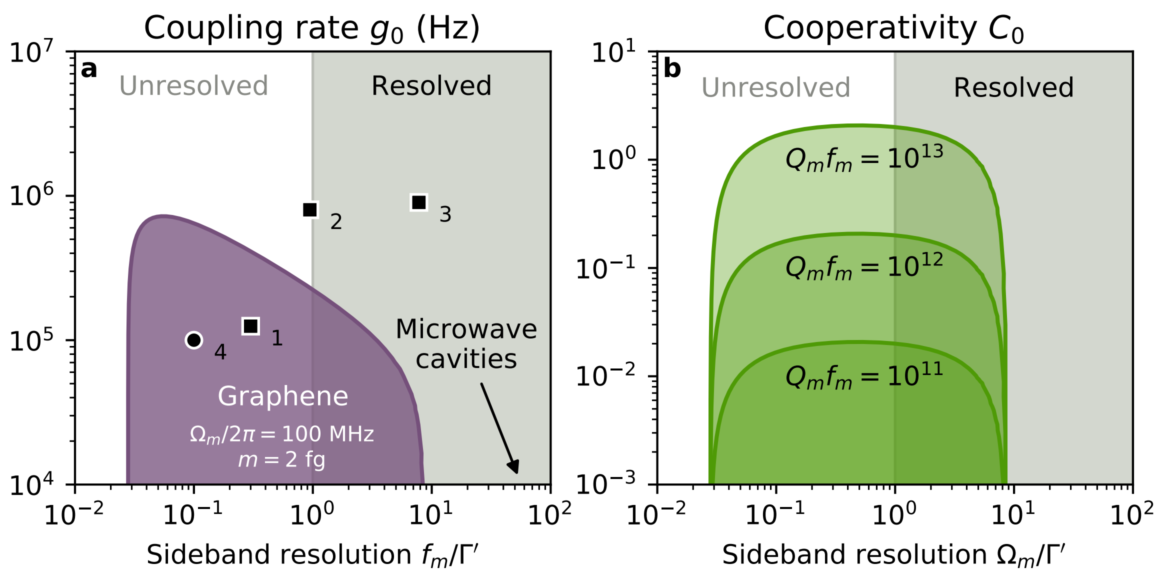

Figure 5.8: (a) Single-photon coupling rate versus mechanical sideband resolution Ω_m/Γ' for graphene cavity optomechanical system operating in the broadband dispersive coupling regime, compared with photonic crystal (1: [111], 2: [113], 3: [112]), micro-ring (4: [114]), and microwave optomechanical systems that lie out of range to the lower right. (b) Single-photon cooperativity for the graphene optomechanical system with $Q_m f_m$ of 10^{11}, 10^{12}, 10^{13}.

of graphene, making the graphene an excellent candidate for exploring dissipative optomechanical cooling. Additionally, near the interband transition frequency, simultaneously large dispersive and dissipative optomechanical coupling are useful for maximizing sensitivity in displacement and force readout, at the expense of significant optical heating.

For optomechanics requiring resolved sideband operation and an associated narrow optical cavity linewidth, the optical loss of graphene can be managed by suspension near the electrical-field nulls of a cavity with sufficiently high unloaded optical quality factor. Dispersive optomechanical coupling around 180 MHz/nm at 100 THz is realizable with graphene mechanical resonators with resonant frequencies above 100 MHz and with a graphene scattering rate of several THz. For graphene with higher scattering rates, advances in raising graphene mechanical resonance frequencies into the few-GHz range would be necessary. On the other hand, coherent photon-phonon coupling is within reach of existing graphene resonators with mechanical quality factors on the order of 10^5. Even though we have focused on membrane-in-cavity systems, our general conclusions regarding the viability of graphene cavity optomechanics in the mid-IR regime and the trade-off between coupling strength and cavity linewidth are applicable to other cavity optomechanical systems that couple graphene with quantum dots, single-particle emitters [29], [30], or traveling-wave resonators [31].

Part III

Magnet-Free Nonreciprocal On-Chip Optics

Chapter 6

Review of Schemes for Realizing Nonreciprocal Responses

A circulator is a nonreciprocal device with at least three ports that circulates waves in only one direction among its ports (Fig. 6.1). In an ideal three port circulator, a wave incident on port one is completely transmitted to port two and a wave incident on port two is completely transmitted to port three. Meanwhile, a wave incident on port three is completely transmitted to port one $(1 \to 2 \to 3 \to 1)$. This ideal nonreciprocal response corresponds to the scattering matrix

$$S = \begin{pmatrix} 0 & 0 & 1 \\ 1 & 0 & 0 \\ 0 & 1 & 0 \end{pmatrix} \tag{6.1}$$

which is not symmetric, $S \neq S^{\mathrm{T}}$.

Circulators play an essential role in many modern optical systems and the functionality that they provide can not be replicated by a linear time-invariant system that exhibits asymmetric transmission for a particular mode. For examples, circulators shield low-noise lasers and amplifiers from undesired reflections that are induced by environmental factors or by fabrication defects [115], [116]. Because the form of parasitic reflections (mode content, polarization, phase, etc) is not known during the design of the system, a component providing protection must reject propagation of *all* waves in the backward direction. Such isolation from reflections is critical for achieving stability and optimal noise performance [117]. Broadening and narrowing of the laser cavity linewidth can be observed for feedback power levels on the order of -90 dB depending on the reflection phase (Fig. 6.2). In more complicated optical circuits and networks, circulators are used to suppress unwanted multi-path interference. In particular, for interferometric sensing applications, where the reflected signal from a sample is measured, circulators are used for splitting and isolation of the incident and reflected signals from the sample where a very high signal-to-noise ratio (SNR) requires a high degree of isolation [118]. These issues highlight the need for extremely large isolation ratios, well beyond the 30 dB level that is typically quoted in the data sheets of commercially available compo-

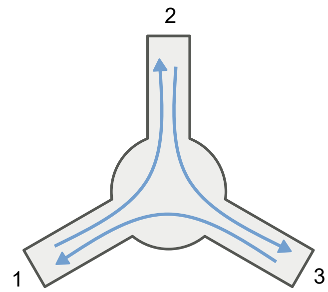

Figure 6.1: Sketch of the nonreciprocal transmission characteristics of a generic three-port circulator. Port one transmits to port two, port two transmits to port three, and port three transmits to port one. The scattering matrix for this system is given by Eqn. 6.1.

nents.

In communications, the nonreciprocal response of a circulator is key for realizing full-duplex transceivers in which a single port (or fiber) is used to simultaneously transmit and receive. This paradigm effectively doubles the system data rate without an associated trade-off in spectrum overhead. Full-duplex schemes also reduce the overall footprint and complexity of transceiver circuitry by allowing front end components to be reused. Full-duplex communication is emerging in next generation communications systems in both radio frequency wireless systems [119] and in single-fiber optical WDM systems [120], [121]. In quantum computing and sensing, circulators play a similar role in protecting sensitive readout circuitry from undesired interference [122], [123].

In real-world systems the scattering response of Eqn. 6.1 is dispersive, which means that there is typically an operating bandwidth and other non-idealities. Two figures of merit are used to quantify the non-ideal response. The isolation ratio or just *isolation* is defined as

$$\mathrm{IR} = 20 \log_{10} \frac{|S_{21}|}{|S_{12}|}, \tag{6.2}$$

and quantifies the contrast between the (desired) forward transmission and (undesired) backward transmission. Applying this to the ideal scattering responses in

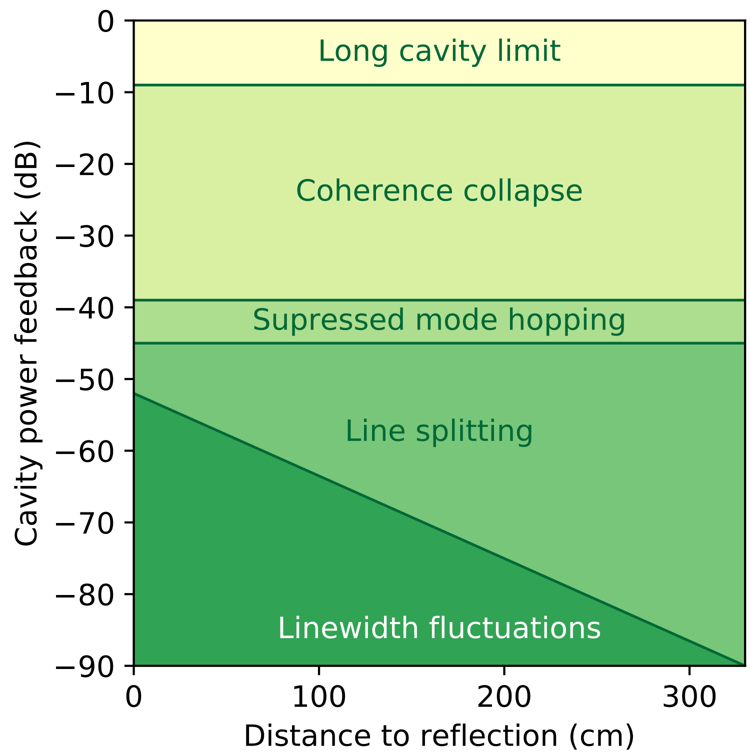

Figure 6.2: TC feedback diagram summarizing the effects of laser cavity feedback as a function of power ratio and reflection distance [117]. Fluctuations in the laser linewidth can be observed as low as -90 dB. Above this threshold feedback-induced mode hopping occurs which results in a splitting of the emission linewidth. Coherence collapse occurs with the formation of auxiliary modes with an associated broadening of the linewidth. At very high levels of feedback, which are challenging to reach due to the high reflectivity of the cavity mirrors, the system resembles a very long cavity with a very small active region.

Eqn. 6.1 yields an infinite isolation ratio. The insertion loss is given by

$$\mathrm{IL} = -20\log_{10}|S_{21}|, \tag{6.3}$$

and characterizes the loss of the circulator when transmitting in the (desired) forward direction.

In the following sections of this chapter we review the various approaches for breaking reciprocity. Note that in this discussion we are not trying to disparage any of the cited works. Rather, we are attempting to present a picture of the overall trade offs between the compatible materials, the required biasing conditions, the applicable operating frequencies (e.g. RF v.s. optical), the operating bandwidth, and the resulting footprint of the devices.

6.1 Magneto-Optical Materials

The standard approach for breaking reciprocity is with materials that lack symmetry in their permittivity or permeability tensors $\left(\epsilon_r \neq \epsilon_r^T \text{ or } \mu_r \neq \mu_r^T\right)$. Under the bias of a static magnetic field ferromagnetic materials exhibit a gyrotropic permeability response at radio frequencies*,

$$\mu_r = \begin{pmatrix} \mu_\perp & +j\mu_a & 0 \\ -j\mu_a & \mu_\perp & 0 \\ 0 & 0 & \mu_\parallel \end{pmatrix}, \tag{6.4}$$

assuming an applied magnetic field in the z-direction. The gyrotropic permeability response induces an effective modal rotation, or *handedness*, at the junction of the transmission lines to realize resonant nonreciprocal scattering of the incident waves. We emphasize that these devices are *resonant*, and require that the spatial distribution of the ferrite material at the junction be engineered to realize the required modal symmetries for the number of ports. These devices benefit from the relatively strong magnetic material response at radio frequencies where significant rotation of the modal field patterns can be achieved.

*Where the two relative permeability components are $\mu_\perp = 1 + \omega_0\omega_m/\left(\omega_0^2 - \omega^2\right)$ and $\mu_a = \omega\omega_m/\left(\omega_0^2 - \omega^2\right)$ with an operating frequency ω. The ferromagnetic resonance properties are $\omega_0 = \mu_0\gamma H_0$ and $\omega_m = \mu_0\gamma M_S$ from an applied magnetic field strength of H_0 [42].

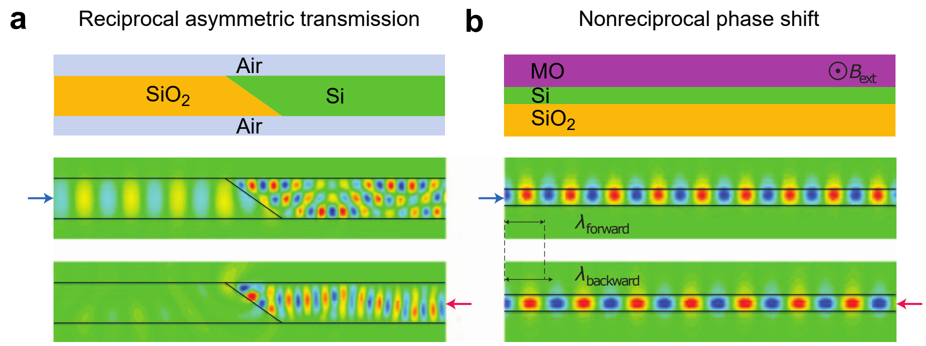

Figure 6.3: Comparison of (a) asymmetric transmission and (b) nonreciprocal waveguide phase shift achieved through application of MO material. Reproduced from [126].

At optical frequencies natural materials do not exhibit a magnetic response, $\mu_\perp \approx 1$ and $\mu_a \approx 0$ in Eqn. 6.4. This makes it impossible to use the same approach in optical systems. Although there is sometimes confusion in the literature, magneto-optical (MO) effects manifest through the material's permittivity tensor [124], [125],

$$\epsilon_r = \begin{pmatrix} \epsilon_\perp & +j\epsilon_a & 0 \\ -j\epsilon_a & \epsilon_\perp & 0 \\ 0 & 0 & \epsilon_\parallel \end{pmatrix}. \tag{6.5}$$

Two orientations of the biasing magnetic field are used with the gyrotropic magneto-optical permitivitty response: the *Faraday* configuration, where the magnetic bias is *parallel* to the direction of light propagation, and the *Voigt* configuration where the magnetic bias is *perpendicular* to the direction of light propagation. In free-space optics, Faraday rotators nonreciprocally rotate the polarization of a beam and, when positioned between two polarizers whose axes are rotated by 45° with respect to each other, they act as an isolator. However, in on-chip systems polarization rotation is not commonly used because MO-induced transverse electric (TE) to transverse magnetic (TM) mode conversion in on-chip waveguides requires additional phase matching considerations. More commonly, the Voigt configuration is used to break the degeneracy of the dispersion of the forward- and backward-propagating waveguide modes. This results in a nonreciprocal phase shift when an on-chip waveguide is evanescently coupled to an MO material (Fig. 6.3b).

Many devices have exploited the Voigt configuration's nonreciprocal phase shift, but all of the approaches can generally be classified into two categories. The first category are waveguide interferometers that use the nonreciprocal phase shift to produce constructive interference for propagation in the forward direction and destructive interference for propagation in the backward direction [127]–[130]. This class of systems can be thought of as an interferometer with a gyrator[†] inserted into one of its arms. Both circulators and isolators can be realized with this approach depending on the particular configuration of the multiplexing and demultiplexing on either end of the nonreciprocal phase shifter. The second class of systems are traveling-wave resonators that use the nonreciprocal phase shift to break the degeneracy of their two counter-propagating modes. In a side-coupled geometry, the broken degeneracy causes the resonant dip in transmission seen by light propagating in the waveguide to split into two different frequencies [131]–[135]. Using this approach both circulators and isolators can be designed, depending on whether the ring resonator is critically coupled to a second waveguide (that allows for nonreciprocal dropping of the wave into another port) or to material absorption or radiation loss.

Note that neither of the above two classes of systems lead to a so-called one-way waveguide, which would imply that there exists *no mode* capable of propagating in the backward direction. The realization of a one-wave waveguide requires an underlying waveguide structure supporting specific features in its dispersion. For example, a photonic crystal waveguide with a defect mode that lies well within the photonic band gap would be a good candidate for realizing a one-way waveguide. The MO response could be engineered to shift the band of the defect mode up or down in frequency to create a bandwidth that has a defect mode with only one allowable propagation direction. Another option would be any mode that has an asymptote at some frequency in its band. One realization of such a system has been proposed using the interface between a 2D photonic crystal and a plasmonic metal [136].

A significant drawback of nonreciprocal schemes that rely on magnetic effects is that magnetically active materials are not compatible with the fabrication

[†]A gyrator is a two-port nonreciprocal phase shifter with an ideal scattering matrix $S = \begin{pmatrix} 0 & 1 \\ -1 & 0 \end{pmatrix}$.

processes or material systems used with photonic integrated circuits. It's also worth noting that these incompatibilities also apply to chip-scale microwave systems that rely on CMOS fabrication processes. Ferrite compounds have a significant mismatch in lattice constant and thermal properties with respect to silicon and the III-V alloys. Although a variety of techniques such as direct wafer bonding and the integration of spacing layers have been considered, they all have associated trade-offs that limit their applicability to large-scale integration. Additionally, spacing layers have the effect of reducing the strength of evanescent coupling between optical waveguides and the MO materials.

Another issue is that natural magnetic responses at optical frequencies are very weak. This leads to the requirement of large device footprints to achieve a substantial nonreciprocal response. For example, the waveguide interferometer schemes mentioned above require waveguide lengths on the order of $\sim 1000\lambda_0$. Although resonant realizations can reduce this by about an order of magnitude, they come with an the trade off of a reduced operating bandwidth. Overall, the large footprints associated with magnetic schemes eat into the limited real estate available in integrated photonic systems and has hindered their adoption in state-of-the-art all-optical communications systems. Finally, even at relatively low frequencies, where magnetic material responses are typically strong, quantum computing applications which incorporate superconducting components are not compatible with the required magnetic biasing fields [137].

6.2 Nonlinear Wave-Mixing

Nonlinear wave interactions have been used for realizing a form of optical isolation that breaks the degeneracy of forward and backward propagating pulses within a certain range of signal intensities [138], [139]. In a structure with an asymmetric permittivity distribution, waves incident from one direction will *feel* a different permittivity distribution due to the nonlinearity. These approaches are not subject to Lorentz reciprocity but are susceptible to dynamic reciprocity because they are not capable of isolating so-called small signals that lie outside of the associated nonlinear operating regime [140]. This limitation has inhibited their adoption in applications that require linear isolation with respect to the signal waves, such as in optical communications.

Another approach using nonlinear wave-mixing can rely on adiabatic frequency conversion in a chirped quasi-phase matched (QPM) grating [141]. In the matched (forward) propagation direction, the signal wave is completely converted into the sum-frequency wave (SFG) or difference-frequency wave (DFG). The grating configuration ensures a directionally dependent conversion, relative to the pump wave, and by matching the conversion rate to the absorption rate at the converted frequency, a relatively broadband isolation is realized, nearly 40 dB across a bandwidth $\Delta\lambda_0 = 50$ nm. This approach is linear with respect to the signal waves because it operates in the undeleted pump regime. However, a significant drawback is the requirement of a total grating length on the order of centimeters to realize complete conversion with matched absorption at the generated frequency. A similar approach has also been proposed using phase-matched parametric amplification through four-wave mixing in a microtoroid resonator [142].

6.3 Time-Varying Systems

A very broad class of systems that break reciprocity and where frequency is no longer a conserved quantity are those which vary in time. Previously electro-absorption modulators and cascaded traveling-wave phase modulators have been proposed as magnet-free optical isolators [143]–[145]. However, these schemes have the drawback of significant energy leakage into higher order sidebands, high insertion loss, and very large device footprints.

The true potential of time-varying systems for realizing nonreciprocal responses lies in transition-matched systems. These *periodically* time-driven systems are capable of realizing diverse nonreciprocal responses through the modulation of coupled resonances and waveguide modes. By targeting the spatial symmetry of the modes and imparting a momentum within the applied modulation, a particular optical transition and nonreciprocal coupling between sets of modes can be induced.

The seminal realization of this idea is nonrecipriocal mode conversion between the first and second-order modes of a dielectric waveguide [146]. This scheme is analogous to indirect electronic transitions in semiconductors and excels in its compatibility with photonic material systems due to a wide range of suitable optical modulation schemes. The key difference between this scheme and previous approaches using traveling-wave modulators [143]–[145] is that the modulation waveform and the optical waveguide dispersion are engineered to target a particular mode transition (e.g. the fundamental TM even mode to the TM odd mode). Additionally, the applied modulation has an asymmetric profile to account for the different symmetries of the optical modes involved in the transition.

However, nonrecipriocal mode conversion within a waveguide still requires a long interaction length due to relatively weak optical modulation effects. For example, complete nonreciprocal mode conversion requires a distance comparable to that of interferometric magneto-optical schemes $L \sim 1000\lambda_0$, or on the order of millimeters for $\lambda_0 = 1550$ nm. An additional challenge is bridging the distance between the bands of the two modes in frequency-momentum space. Relying on practical optical modulation frequencies ($\sim$20 GHz) means that the required modulation momentum needs to be extremely large, orders of magnitude greater than what's available in state-of-the-art optical phase modulators. Additionally, compensating for the symmetry in the even and odd-mode conversion scheme requires a laterally asymmetric modulation profile across the waveguide core. An experimental realization of this resulted in a very complex network of p-type and n-type doped regions with interdigitated control electrodes to allow for forward and reverse biasing of the individual junctions [147]. Off-chip experimental realizations of this approach have used on acoustic wave modulation within a fiber, which is more challenging to translate *directly* to on-chip photonic systems [148]. However, this approach is closely related to nonreciprocal on-chip schemes that rely on stimulated Brillouin scattering (SBS), which is a nonlinear (or optomechanical) approach that we will review in more detail in the next section of this chapter.

Another approach to nonreciprocal mode coupling with time-modulation has instead used an applied modulation with an angular phase dependence, or an angular momentum [149]. This has been used to break the degeneracy of counter propagating modes in an optical ring resonator, resulting in a response similar to evanescently coupling with magneto-optical rings. The resulting system acts as a nonreciprocal add-drop filter when the rings are side-coupled to two waveguides. However, this design presents the inherent trade-off in simultaneously realizing a high isolation and a low insertion loss. Ideal operation requires a large mode splitting which results from a strong coupling of the two counter propagating modes (strong modulation). The resultant absorption from the modulation increases the linewidth and creates the need to further increase the mode splitting to realize a comparable insertion loss. In general there are simply not enough degrees of freedom within the system to simultaneously realize perfect isolation and zero insertion loss. This applies regardless of whether magnetic or time-modulation schemes are used to break the mode degeneracy. The additional challenge in implementing this approach at optical frequencies is in realizing a well-defined angular modulation phase.

As a general comment, the experimental realization of circulators and isolators with the schemes discussed above have had much greater success at radio frequencies [150]–[153]. This is largely due to much stronger modulation at much greater *relative* speeds. Also, the availability of subwavelength lumped elements at microwave frequencies allows for the realization of extremely compact nonreciprocal device structures.

6.4 Optomechanical Interactions

The coherent coupling of photonic and *phononic* systems has recently been demonstrated as a means for realizing strongly nonreciprocal responses. These can be realized in both co-localized optical and mechanical resonances [154]–[156] and waveguide geometries [157]–[159].

In essence, the first class of systems consists an optical and mechanical mode that are spatially coupled to a waveguide (or set of waveguides, depending on the topology). The overall response resembles nonreciprocal electromagnetically induced transparency (EIT). When the mechanical mode is pumped at one of the mechanical sidebands through the waveguide(s), a secondary probe signal will *feel* the mechanical mode when it is co-propagating with the pump but not when propagating in the opposite direction of the pump. This phenomena is essentially due to the pump and probe signals beating at the mechanical resonance frequency and the directionality of the optomechanical interaction is what leads to a nonreciprocal response for the *probe* signal. If the pumping of the mechanical mode is strong, the co-propagating probe will see a complete splitting of the mode and if the pumping is weak, the probe will see a narrow transparency window with larger insertion loss. Depending on whether the optical resonator is critically coupled to a second waveguide or to a loss channel, an isolator or circulator response can be realized.

At a high level, the class of systems based on photon-phonon interactions in waveguides can be seen as analogous to modulation-induced nonreciprocity, with phonons replacing the role of the modulation to induce an optical waveguide mode transition. This similarity is especially clear in the frequency-momentum picture of Brillouin scattering where co-localized propagating photon and phonon modes can realize both nonreciprocal amplification and nonreciprocal mode conversion [157].

Generally, nonreciprocal cavity optomechanics requires resolved sideband operation, which means that the mechanical resonance frequency must exceed the optical cavity linewidth. Additionally, the realization of a low insertion loss and large isolation requires a strong coherent coupling between the optical and mechanical modes, quantified by the optomechanical cooperativity $C = 4g^2/\Gamma\Gamma_m$. The parameter g quantifies the strength of the optomechanical coupling (proportional to the change in optical resonance frequency per unit mechanical displacement) The parameters Γ and Γ_m are the optical and mechanical linewidths, respectively.

As was the case with time-modulation nonreciprocity, nonreciprocal cavity optomechanics excel at microwave frequencies where large values of C can be readily obtained from the reduced cavity linewidths (Γ) and generally larger optomechanical coupling strengths (g). In general, noise performance of nonreciprocal cavity optomechanical systems is improved with stronger coupling *or* through operations at low temperatures. This has been demonstrated recently using dissipative optomechanical coupling in superconducting microwave circuits [137], [160]. However several recent efforts at optical frequencies have been able to demonstrate strong nonreciprocal absorption using red-detuned pumping in on-chip resonators [155]. Additionally, it has been shown that nonreciprocal optomechanical *amplification* can be realized in the case of a blue-detuned pump wave [156]. These cases both represent specific examples in a more general framework of reservoir engineering [161].

6.5 Topological Photonics

When combined into periodic lattices and arrays, nonreciprocal devices provide the broken time-reversal symmetry needed to create topologically protected photonic edge states that are immune to disorder-induced backscattering [162]. In this section we briefly mention several relevant aspects of this emerging field.

Extended lattices of time-modulated resonators have been proposed to realize topologically protected edge states in both acoustics [163] and photonics [164]. Several other proposals have extended this concept towards realizing an additional dimension in frequency space through the coupling of multiple physical modes through modulation at the free spectral range [165], [166]. Such systems present opportunities to realize and study topological effects in classical systems and for realizing spin (polarization) locked one-way edge modes that are immune to disorder-induced backscattering. However, in the context of on-chip nonreciprocal optical signal processing these systems are large: extended lattices of resonators are required with a prescribed periodic distribution of phasing in the modulation signals. Although the tolerance on the phasing scheme can be relaxed considerably, by considering unit cells with rotational symmetry [163]. Overall this class of systems provides a route towards realizing broadband nonreciprocal effects, but at the cost of a large footprint for realizing the necessary topological effects.

Chapter 7

Floquet Resonators: Nonreciprocal Phase Shifters and Dual-Carrier Circulators

A linear time-invariant (LTI) system is transformed into a Floquet system by an externally applied periodic modulation. In such linear periodically time-varying (LPTV) systems every static eigenstate of the time-invariant system is transformed into a set of Floquet states. The new set of Floquet resonances are are periodically separated in frequency and their individual amplitudes (or equivalently, fraction of energy stored) and phases are determined by the functional form of the modulating wave. Purely sinusoidal modulation, with only a single frequency component, produces a Floquet state amplitude distribution defined by Bessel functions of the first kind (Fig. 7.1a), which is identical to the sideband amplitudes produced in optical phase modulators defined by the Jacobi-Anger expansion [167].

However, these amplitudes can be individually tailored with more general forms of modulation beyond pure single-frequency sinusoidal waveforms [168], [169]. For example, a modulation waveform consisting of a combination of first and second harmonic waves, i.e. frequency components Ω and 2Ω, leads to an entirely different Floquet amplitude distribution (Fig. 7.1b). More general sideband distributions, beyond the distribution defined by the Jacobi-Anger expansion, are well known in the context of parametric resonances in quantum field theory and in single-sideband (SSB) modulation as applied to radio frequency wireless systems. However, the deliberate control these of resonances remains to be exploited as a degree of freedom in nonreciprocal optical and acoustic responses.

In this chapter we explore the possibility of controlling the amplitude of individual Floquet sidebands in a new compact device structure to realize nonreciprocal spectral responses. We first examine the nonreciprocal phase shift and general scattering properties of a single parametrically modulated (Floquet) resonator side-coupled to two waveguides. We then apply temporal coupled-mode theory to study the necessary conditions that produce unique circulator responses from a low-symmetry cascade of two such Floquet resonators. A compact three-port circulator based on individually coupled Floquet sidebands is demonstrated that

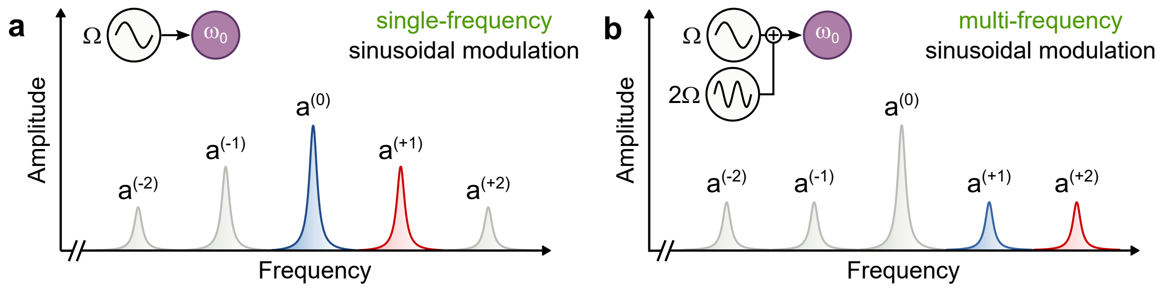

Figure 7.1: Sketch of the Floquet sideband frequency distributions from (a) single-frequency sinusoidal modulation and (b) multi-frequency sinusoidal modulation waveforms. Single-frequency modulation results in a sideband amplitude distribution defined by the Jacobi-Anger expansion, analogously to optical phase modulators. Bessel functions of the first kind define the amplitudes of the sidebands which are spaced at intervals of the fundamental modulation frequency Ω. Multi-frequency sinusoidal modulation, in this case where the modulation signal has frequency components Ω and 2Ω, can be approximated as a superposition of two distributions defined by the Jacobi-Anger expansion. However, no closed-form analytical expression exists for its solution.

provides broadband nonreciprocal transmission that is distinct from conventional circulators and a photonic crystal realization is then presented from the results of first-principle simulations (see Appendix C).

7.1 Single Floquet Resonator: Nonreciprocal Phase Shifter

The proposed circulator is based on modulated standing-wave resonators that support a set of Floquet sidebands spectrally distributed on both sides of the intrinsic structural resonance frequency ω_a at intervals given by the fundamental modulation frequency Ω (Fig. 7.1a). When coupled to two narrowband waveguides that target individual sidebands, highly nonreciprocal scattering pathways can be realized. A sketch of the spectral features of the system, namely the resonance spectrum and the waveguide spectrum, is shown in Fig. 7.2 to illustrate the sideband-selective coupling.

For the first part of this work we do not make an explicit choice for the modulation waveform. Instead, we consider only a general sideband distribution and denote the complex instantaneous amplitude of the n-th sideband by $a^{(n)}$. In a high quality factor resonator, where the modulation-driven energy exchange rate

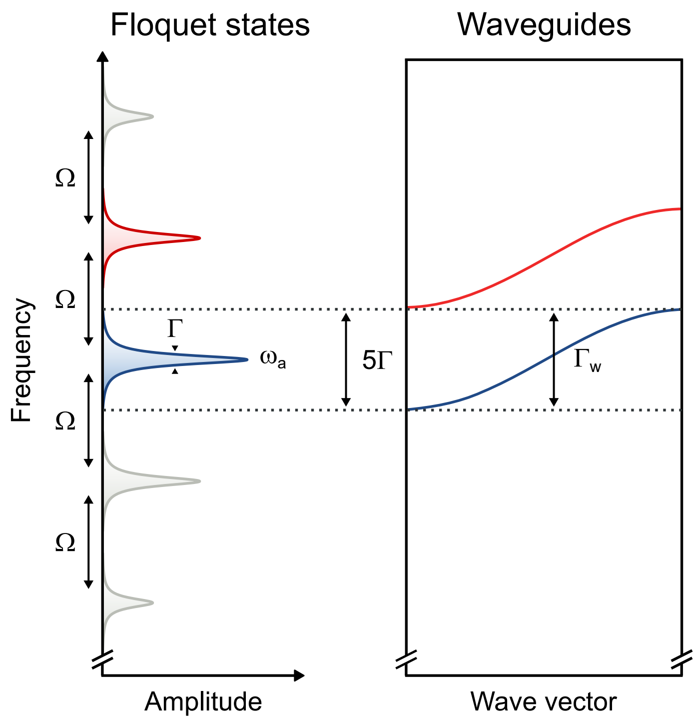

Figure 7.2: Summary of the spectral features of the Floquet system. The modulation frequency defines the distance between the sidebands and the resonator linewidth, Γ determines the bandwidth of the nonreciprocal response. The bandwidth of the waveguide given by Γ_w must satisfy $\Gamma_w < \Omega$ and similarly, the linewidth (full-width half-max) of the resonator must satisfy $\Gamma \leq \Gamma_w/5$.

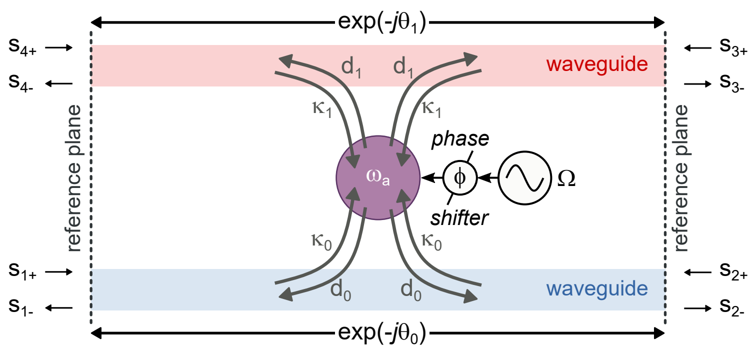

Figure 7.3: Schematic of a single Floquet resonator supporting an intrinsic mode at frequency ω_a. The resonator is modulated by single-frequency sinusoidal waveform with fundamental frequency Ω and an applied phase shift of ϕ. The top waveguide (red) targets the $n = 1$ sideband with an evanescent coupling rate of γ_1, and the bottom waveguide (blue) targets the $n = 0$ sideband with an evanescent coupling rate of γ_0. The overlap of the sideband spectrum and the waveguide spectrum is sketched in Fig. 7.2. The phase delay between the port reference planes in the top and bottom waveguides are θ_0 and θ_1, respectively.

between the sidebands exceeds the external coupling rate, the amplitudes of the sidebands are coherently correlated. Thus, the amplitude $a^{(n)}$ can be expressed as the product $a^{(n)} = u^{(n)}a$, between the total mode amplitude a and the relative sideband amplitude $u^{(n)}$. The expression $|a|^2$ is proportional to the total energy stored in the resonator, aggregated over all Floquet sidebands and $u^{(n)}$ is the solution of Hill's differential equation for the case of a periodic modulation waveform [169], [170].

Although the amplitudes of the sidebands are correlated, each sideband can couple very differently to the external environment, such that the non-trivial phase between the modulating waveform and the optical carrier waves produces a nonreciprocal response. For example, similar to the well-known channel add-drop filter configuration [171], we side-couple two parallel narrowband waveguides to either side of the Floquet resonator (Fig. 7.3), with each waveguide having such a narrow bandwidth that it can couple to only one of the sidebands. The top waveguide (red) is selective of the $n = +1$ sideband and the bottom waveguide (blue) is selective of the $n = 0$ sideband. The evanescent coupling from the resonator to the bottom (top) waveguide results in a decay rate γ_0 (γ_1).

7.1.1 Coupled Mode Theory

In a resonator with a sufficiently high quality factor, temporal coupled mode theory (CMT) accurately describes the time evolution of the Floquet sideband amplitudes. Unlike unmodulated frequency-conserving CMT [172] (see Appendix B), the approach for time-modulated resonators begins by considering the amplitudes of the $n = 0$ and $n = +1$ sidebands that coexist within the same resonator site, which appears similar to the notation used to describe the coupling of several separate structural modes.

For the system considered in Fig. 7.3, two coupled mode equations are used to capture the time evolution of each sideband,

$$\frac{d}{dt}u^{(0)}a = (j\omega_a - \gamma)\, u^{(0)}a + \begin{pmatrix} \kappa_0 & \kappa_0 \end{pmatrix} \begin{pmatrix} s_{1+} \\ s_{2+} \end{pmatrix} \tag{7.1}$$

$$\frac{d}{dt}u^{(1)}a = (j\omega_a + j\Omega - \gamma)\, u^{(1)}a + \begin{pmatrix} \kappa_1 & \kappa_1 \end{pmatrix} \begin{pmatrix} s_{3+} \\ s_{4+} \end{pmatrix} \tag{7.2}$$

where s_{m+} is the instantaneous amplitude of the incident wave from the m-th port and $\gamma = \gamma_0 + \gamma_1 + \gamma_L$ for the absorption or radiation rate given by γ_L. Note that only two sidebands need to be explicitly considered, and all other sidebands are maintained at their individual relative amplitudes dictated by the modulation waveform. The coefficients $\kappa_{0(1)}$ represent the geometric coupling between the incoming wave and the $n = 0$ $(n = +1)$ Floquet sideband.

The system considered here is distinct from conventional nonreciprocal systems involving Floquet states, in that the signal can be carried simultaneously by multiple sidebands. To clearly differentiate the signal wave from the sideband carriers, we decompose the instantaneous amplitudes of the incoming and outgoing waves at the m-th port, $s_{m\pm}(\omega) = \tilde{s}_{m\pm}(\Delta)\, e^{j(\omega_a + n\Omega)t}$ to a slowly varying envelope $\tilde{s}_{m\pm}(\Delta)$, i.e. the signal wave, and the sideband carriers $e^{j(\omega_a + n\Omega)t}$. The instantaneous frequency ω is related to the frequency detuning parameter by $\Delta = \omega - (n\Omega + \omega_a)$ where the integer n is the sideband order targeted by the particular waveguide or port. The scattering parameters throughout the remainder of this paper are therefore defined in terms of the signal wave, i.e. $S_{mp} = \tilde{s}_{m-}(\Delta) / \tilde{s}_{p+}(\Delta)$, where the optical carrier frequencies at ports m and p are generally different. The slowly varying envelope of the resonator $\tilde{a}$ is defined similarly.

Using this notation, the instantaneous and baseband quantities have the time dependence,

$$\begin{aligned} a &\sim \exp(j\omega t) & \tilde{a} &\sim \exp(j\Delta t) \\ s_{n\pm} &\sim \exp(j\omega t) & \tilde{s}_{n\pm} &\sim \exp(j\Delta t)\,. \end{aligned}$$

By substituting $d/dt \to j\omega$, Eqns. 7.1 and 7.2 can be combined and rearranged into a transfer function between the incoming wave amplitudes and the overall modal amplitude as

$$\tilde{a} = \frac{1}{j\Delta + \gamma}\begin{pmatrix} d_0 u^{(0)*} & d_0 u^{(0)*} & d_1 u^{(1)*} & d_1 u^{(1)*} \end{pmatrix} \cdot \begin{pmatrix} \tilde{s}_{1+} \\ \tilde{s}_{2+} \\ \tilde{s}_{3+} \\ \tilde{s}_{4+} \end{pmatrix}, \tag{7.3}$$

where d_0 (d_1) represent the structural coupling between the bottom (top) waveguide. The output CMT equation between the resonator and the ports is

$$\begin{pmatrix} \tilde{s}_{1-} \\ \tilde{s}_{2-} \\ \tilde{s}_{3-} \\ \tilde{s}_{4-} \end{pmatrix} = \begin{pmatrix} 0 & e^{-j\theta_0} & 0 & 0 \\ e^{-j\theta_0} & 0 & 0 & 0 \\ 0 & 0 & 0 & e^{-j\theta_1} \\ 0 & 0 & e^{-j\theta_1} & 0 \end{pmatrix} \begin{pmatrix} \tilde{s}_{1+} \\ \tilde{s}_{2+} \\ \tilde{s}_{3+} \\ \tilde{s}_{4+} \end{pmatrix} + \begin{pmatrix} d_0 u^{(0)} \\ d_0 u^{(0)} \\ d_1 u^{(1)} \\ d_1 u^{(1)} \end{pmatrix} \tilde{a}, \tag{7.4}$$

where $\theta_{0(1)}$ defines the phase shift between the port reference planes in the bottom (top) waveguide. Note that we have assumed the symmetry of the resonator mode results in the same coupling coefficient for pairs of ports that share a waveguide (i.e. κ_0, and d_0 for the bottom waveguide and κ_1 and d_1 for the top waveguide). We next use energy conservation and time reversal symmetry to derive the relationships between the linewidth, the coupling coefficients, and the relative sideband amplitudes.

Energy Conservation

We first consider the case of no excitation, meaning that $\tilde{s}_{m+} = 0$ for all m. From Eqns. 7.1 and 7.2, this means that

$$\frac{d}{dt}|\tilde{a}|^2 = -2\gamma|\tilde{a}|^2 \tag{7.5}$$

and from Eqn. 7.4, we have

$$-\frac{d}{dt}|\tilde{a}|^2 = \sum |s_{m-}|^2 = \left(2\left|d_0 \cdot u^{(0)}\right|^2 + 2\left|d_1 \cdot u^{(1)}\right|^2\right)|\tilde{a}|^2. \tag{7.6}$$

By equating the expressions in Eqns. 7.5 and 7.6, we conclude that the coupling rates for the bottom and top waveguide to the resonator are given by

$$\gamma_0 = \left|d_0 \cdot u^{(0)}\right|^2 \tag{7.7}$$

$$\gamma_1 = \left|d_1 \cdot u^{(1)}\right|^2 \tag{7.8}$$

respectively, where (neglecting radiation and absorption loss) the total linewidth is $\gamma = \gamma_0 + \gamma_1$. Note there is *not* a factor of $1/2$ on the right side of Eqn. 7.7 and Eqn. 7.8. When comparing these expressions to other coupled mode theory expressions, especially those involving *two-port* optical systems [172], this may appear to be an error. However, the expressions in Eqn. 7.7 and Eqn.7.8 are correct because γ_0 and γ_1 are defined to represent the coupling rate to the entire bottom and top waveguides, which each have *two* associated ports. To compare with two-port systems, γ_0 and γ_1 would need to be redefined as $\gamma_0 = \gamma_{0,1} + \gamma_{0,2}$ and $\gamma_1 = \gamma_{1,1} + \gamma_{1,2}$ where $\gamma_{0,1}$, $\gamma_{0,2}$, $\gamma_{1,1}$, and $\gamma_{1,2}$ are the individual port coupling rates. For comparison, see Appendix B for the coupled mode theory derivation for several unmodulated two-port optical systems.

When absorption or radiation loss is negligible $(\gamma_L \ll \gamma_0, \gamma_1)$, an ideal non-reciprocal response occurs at critical coupling $(\gamma_0 = \gamma_1)$, which is equivalent to the condition

$$\left|\frac{d_0}{d_1}\right| = \left|\frac{u^{(1)}}{u^{(0)}}\right|. \tag{7.9}$$

This means many system configurations can lead to critical coupling where the

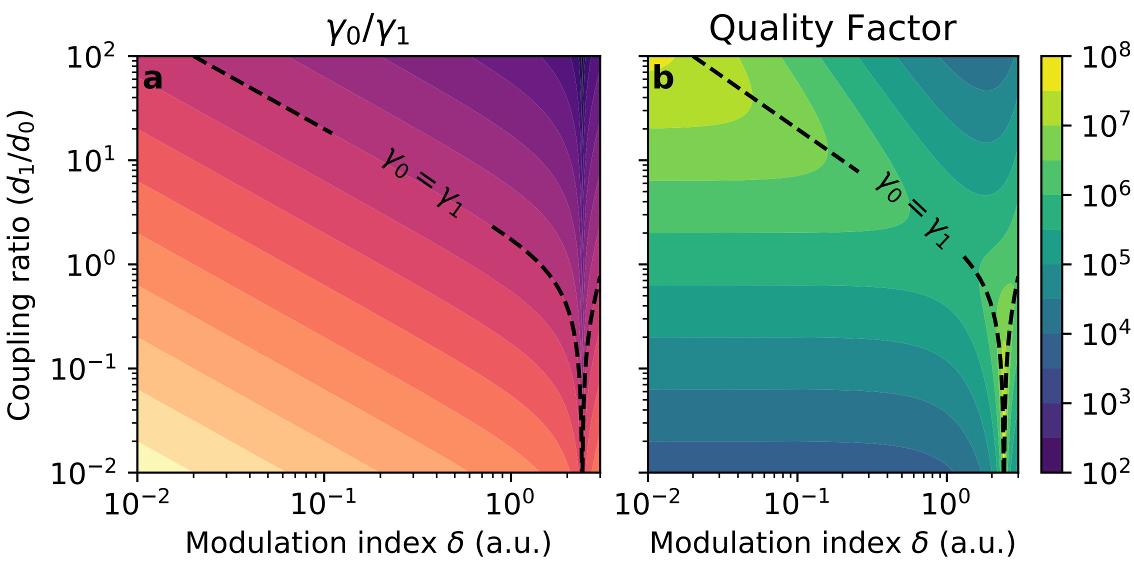

Figure 7.4: (a) Design chart for realizing critical coupling ($\gamma_0 = \gamma_1$) and (b) associated quality factor in terms of modulation index and coupling ratio, defined by the ratio of the structural coupling coefficients.

difference in the sideband amplitudes, quantified by $u^{(1)}/u^{(0)}$, can be compensated by asymmetry in the structural coupling, quantified by d_0/d_1. Figure 7.4a shows contours for the ratio γ_0/γ_1 as a function of the structural coupling ratio d_1/d_0 and the modulation index δ, assuming single-frequency sinusoidal modulation and relative sideband amplitudes that are proportional to Bessel functions of the first kind.

Towards the left of Fig. 7.4a where modulation is weak, a very large asymmetry in structural coupling is required to reach the critical coupling condition because the amplitude of the sideband associated with the top waveguide is extremely small. The dip in the critical coupling countour on the right is where the sideband amplitude associated with the bottom waveguide (the fundamental resonance) becomes depleted due to very strong modulation. At this extreme, the resonator needs to be shifted closer to the bottom waveguide to achieve critical coupling. Fig. 7.4b shows the total quality factor of the resonator, demonstrating that operating at either extreme of the design chart for critical coupling yields a larger total quality factor.

Time-reversal Symmetry

The first condition provided by time reversal symmetry is

$$2\gamma = 2\kappa_0 {d_0}^* + 2\kappa_1 {d_1}^*, \tag{7.10}$$

which, when taken with Eqns. 7.7 and 7.8, implies that $\kappa_m = d_m \left| u^{(m)} \right|^2$. Additionally, the direct scattering process through the waveguides requires that

$$\begin{pmatrix} d_0 \\ d_0 \\ d_1 \\ d_1 \end{pmatrix} = - \begin{pmatrix} 0 & e^{-j\theta_0} & 0 & 0 \\ e^{-j\theta_0} & 0 & 0 & 0 \\ 0 & 0 & 0 & e^{-j\theta_1} \\ 0 & 0 & e^{-j\theta_1} & 0 \end{pmatrix} \begin{pmatrix} {d_0}^* \\ {d_0}^* \\ {d_1}^* \\ {d_1}^* \end{pmatrix}, \tag{7.11}$$

or equivalently, $d_0 = -e^{-j\theta_0} {d_0}^*$ and $d_1 = -e^{-j\theta_1} {d_1}^*$. By selecting the location of the reference planes such that θ_0 and θ_1 are some integer multiple of 2π, the expression in Eqn. 7.11 is satisfied by d_0 and d_1 being purely imaginary and with magnitudes that satisfy Eqns. 7.7 and 7.8. The complete expressions are therefore

$$d_0 = j\frac{\sqrt{\gamma_0}}{\left|u^{(0)}\right|} \qquad d_1 = j\frac{\sqrt{\gamma_1}}{\left|u^{(1)}\right|} \tag{7.12}$$

$$\kappa_0 = d_0 \left|u^{(0)}\right|^2 = j\sqrt{\gamma_0}\left|u^{(0)}\right| \qquad \kappa_1 = d_1 \left|u^{(1)}\right|^2 = j\sqrt{\gamma_1}\left|u^{(1)}\right|. \tag{7.13}$$

Complete Scattering Matrix

Combining Eqn. 7.3 and the output coupling relationship given by eqn Eqn. 7.4, leads to a scattering matrix for the single Floquet resonator system [173] as a function of the detuning,

$$\begin{aligned}
\tilde{a} &= \frac{1}{j\Delta+\gamma}\begin{pmatrix}\frac{\kappa_0}{u^{(0)}} & \frac{\kappa_0}{u^{(0)}} & \frac{\kappa_1}{u^{(1)}} & \frac{\kappa_1}{u^{(1)}}\end{pmatrix}\cdot\begin{pmatrix}\tilde{s}_{1+}\\ \tilde{s}_{2+}\\ \tilde{s}_{3+}\\ \tilde{s}_{4+}\end{pmatrix}\\
&= \frac{1}{j\Delta+\gamma}\begin{pmatrix}\frac{d_0\left|u^{(0)}\right|^2}{u^{(0)}} & \frac{d_0\left|u^{(0)}\right|^2}{u^{(0)}} & \frac{d_1\left|u^{(1)}\right|^2}{u^{(1)}} & \frac{d_1\left|u^{(1)}\right|^2}{u^{(1)}}\end{pmatrix}\cdot\begin{pmatrix}\tilde{s}_{1+}\\ \tilde{s}_{2+}\\ \tilde{s}_{3+}\\ \tilde{s}_{4+}\end{pmatrix}\\
&= \frac{1}{j\Delta+\gamma}\begin{pmatrix}j\sqrt{\gamma_0}e^{-j\angle u^{(0)}} & j\sqrt{\gamma_0}e^{-j\angle u^{(0)}} & j\sqrt{\gamma_1}e^{-j\angle u^{(1)}} & j\sqrt{\gamma_1}e^{-j\angle u^{(1)}}\end{pmatrix}\cdot\begin{pmatrix}\tilde{s}_{1+}\\ \tilde{s}_{2+}\\ \tilde{s}_{3+}\\ \tilde{s}_{4+}\end{pmatrix}.
\end{aligned} \tag{7.14}$$

The output coupling is given by the relationship

$$\begin{aligned}
\begin{pmatrix}\tilde{s}_{1-}\\ \tilde{s}_{2-}\\ \tilde{s}_{3-}\\ \tilde{s}_{4-}\end{pmatrix} &= \begin{pmatrix}0 & e^{-j\theta_0} & 0 & 0\\ e^{-j\theta_0} & 0 & 0 & 0\\ 0 & 0 & 0 & e^{-j\theta_1}\\ 0 & 0 & e^{-j\theta_1} & 0\end{pmatrix}\begin{pmatrix}\tilde{s}_{1+}\\ \tilde{s}_{2+}\\ \tilde{s}_{3+}\\ \tilde{s}_{4+}\end{pmatrix} + \begin{pmatrix}d_0u^{(0)}\\ d_0u^{(0)}\\ d_1u^{(1)}\\ d_1u^{(1)}\end{pmatrix}\tilde{a}\\
&= \begin{pmatrix}0 & e^{-j\theta_0} & 0 & 0\\ e^{-j\theta_0} & 0 & 0 & 0\\ 0 & 0 & 0 & e^{-j\theta_1}\\ 0 & 0 & e^{-j\theta_1} & 0\end{pmatrix}\begin{pmatrix}\tilde{s}_{1+}\\ \tilde{s}_{2+}\\ \tilde{s}_{3+}\\ \tilde{s}_{4+}\end{pmatrix} + \begin{pmatrix}j\sqrt{\gamma_0}e^{j\angle u^{(0)}}\\ j\sqrt{\gamma_0}e^{j\angle u^{(0)}}\\ j\sqrt{\gamma_1}e^{j\angle u^{(1)}}\\ j\sqrt{\gamma_1}e^{j\angle u^{(1)}}\end{pmatrix}\tilde{a}.
\end{aligned} \tag{7.15}$$

By combining Eqn. 7.14 with Eqn. 7.15 and letting $\phi = \angle u^{(1)} - \angle u^{(0)}$, the complete scattering matrix for the system can be solved for,

$$S^{\mathrm{I}}(\Delta) = \begin{pmatrix} 0 & 1 & 0 & 0 \\ 1 & 0 & 0 & 0 \\ 0 & 0 & 0 & 1 \\ 0 & 0 & 1 & 0 \end{pmatrix} - \\ \frac{1}{j\Delta + \gamma} \begin{pmatrix} \gamma_0 & \gamma_0 & \sqrt{\gamma_0\gamma_1}e^{-j\phi} & \sqrt{\gamma_0\gamma_1}e^{-j\phi} \\ \gamma_0 & \gamma_0 & \sqrt{\gamma_0\gamma_1}e^{-j\phi} & \sqrt{\gamma_0\gamma_1}e^{-j\phi} \\ \sqrt{\gamma_0\gamma_1}e^{j\phi} & \sqrt{\gamma_0\gamma_1}e^{j\phi} & \gamma_1 & \gamma_1 \\ \sqrt{\gamma_0\gamma_1}e^{j\phi} & \sqrt{\gamma_0\gamma_1}e^{j\phi} & \gamma_1 & \gamma_1 \end{pmatrix}. \quad (7.16)$$

We use the notation of the superscript I in S^{I} to specify that we are *explicitly* considering the scattering matrix of a single Floquet resonator. Later in this chapter we will use S^{II}, which corresponds to the system formed from a cascade of *two* Floquet resonators. At other times we may just use S when we are referring to no specific system.

7.1.2 Phase Response

The relative phase between the modulation sidebands, defined as $\phi = \angle u^{(1)} - \angle u^{(0)}$, is the key to realizing a nonreciprocal response. Aside from the case of ϕ being an integer multiple of π, S^{I} is *not* symmetric and Eqn. 7.16 describes a nonreciprocal system. The forward pathways from the top waveguide to the bottom waveguide (S^{I}_{13}, S^{I}_{14}, S^{I}_{23}, and S^{I}_{24}) have phase shifts with opposite signs from their backward counterparts (S^{I}_{31}, S^{I}_{41}, S^{I}_{32}, and S^{I}_{42}). Specifically, signal flow in these forward pathways involves energy transfer from the $n = 0$ sideband to the $n = 1$ sideband, resulting in a positive phase shift $e^{j\phi}$, whereas the backward pathways all involve energy transfer in the opposite direction between the sidebands, resulting in the negative phase shift $e^{-j\phi}$. The largest nonreciprocal response is achieved when $\phi = (n + 1/2)\,\pi$, where n is an integer. Note that with a single-frequency sinusoidal modulation like in Fig. 7.1, ϕ is simply the phase difference between the modulating wave and the incoming optical carrier.

7.1.3 Compound Waveguide Mode Filtering

To understand how the nonreciprocal phase response of a single resonator (Eqn. 7.16) can be transformed into an ideal circulator power response, we adopt a frame of compound waveguide modes that are linear combinations of the individual waveguide modes (Fig. 7.6b). We refer the in-phase and out-of-phase combinations of the individual waveguide modes as the even and odd compound modes respectively. This notation is analogous to the Jones vector used to describe polarization states [174] in that the spatially-separated individual waveguide modes, at their own optical carrier frequencies, play the role of two linear polarizations. This approach is mathematically equivalent to a rotation of the four-port scattering matrix into a basis defined by the vectors

$$b_1 = \frac{1}{\sqrt{2}}\begin{pmatrix}1\\0\\0\\1\end{pmatrix}, \quad b_2 = \frac{1}{\sqrt{2}}\begin{pmatrix}1\\0\\0\\-1\end{pmatrix}, \quad b_3 = \frac{1}{\sqrt{2}}\begin{pmatrix}0\\1\\1\\0\end{pmatrix}, \quad b_4 = \frac{1}{\sqrt{2}}\begin{pmatrix}0\\1\\-1\\0\end{pmatrix}. \qquad (7.17)$$

By specifying a change of basis matrix $B = \begin{pmatrix} b_1 & b_2 & b_3 & b_4 \end{pmatrix}$, the scattering matrix S for a four-port system is transformed into the scattering matrix for the compound modes defined by Eqn. 7.17 through the operation

$$S' = B^{-1}SB = B^T SB$$

where where $B^{-1} = B^T$ because the vectors in Eqn. 7.17 are orthonormal. Such a change of basis preserves the symmetry of the original scattering matrix. For the case of $\phi = 0$, the scattering matrix is symmetric $\left(S = S^T\right)$ and therefore

$$\left(S'\right)^T = \left(B^T SB\right)^T = B^T S^T \left(B^T\right)^T = B^T S^T B = B^T SB = S'.$$

Similarly, for $\phi = \pi/2$ the scattering matrix is Hermitian $(S = S^*)$ and therefore

$$\left(S'\right)^* = \left(B^T SB\right)^* = B^T S^* \left(B^T\right)^* = B^T S^* B = B^T SB = S'.$$

The above results imply that reciprocity (and nonreciprocity) are preserved under the change of basis to the compound mode set defined by the vectors in Eqn. 7.17.

In the frame of even and odd compound modes, the single Floquet resonator acts as a notch filter, completely reflecting one "polarization" while completely transmitting the other. The "polarization" being reflected is entirely determined by the modulation phase ϕ. For example, when the fundamental in the applied modulation waveform is in phase with the optical carrier ($\phi = 0$), the even compound mode $\begin{pmatrix} 1 & 1 \end{pmatrix}^{\mathrm{T}}$ is completely reflected while the odd compound mode $\begin{pmatrix} 1 & -1 \end{pmatrix}^{\mathrm{T}}$ does not couple to the resonator and is completely transmitted (Fig. 7.5a,b). Tuning the applied modulation phase for maximal nonreciprocal phase response, with a quadrature phase shift with respect to the optical carrier ($\phi = \pi/2$), does not lead to a response with complete reflection or transmission of the orthonormal mode basis defined by Eqn. 7.17. The condition of $\phi = \pi/2$ leads to complete reflection of a "circular" compound mode $\begin{pmatrix} 1 & j \end{pmatrix}^{\mathrm{T}}$ and the complete transmission of the other circular compound mode $\begin{pmatrix} 1 & -j \end{pmatrix}^{\mathrm{T}}$, which also does not couple to the resonator (Fig. 7.5c,d). Multiple Floquet resonators and reciprocal mode conversion in the passive waveguide segments provide the basis for more functional nonreciprocal responses in terms of scattered power.

7.2 Dual-Resonator Floquet Circulator

Cascading two Floquet resonators not only eliminates the practical challenge of maintaining a locked phase shift between the modulating wave and the optical carrier, which have an orders of magnitude difference in their respective frequencies, but more importantly provides the basis for an asymmetry within the system through the modulation. This asymmetry is the critical requirement for realizing a nonreciprocal response in terms of scattered *power*.

In the configuration we consider, the second resonator is geometrically identical to the first. It supports the same set of Floquet modes and is critically coupled to the same waveguides with coupling rates γ_0 and γ_1. The parameters ϕ_a and ϕ_b refer to the phase delay of the modulation applied to the left and right resonator, respectively.

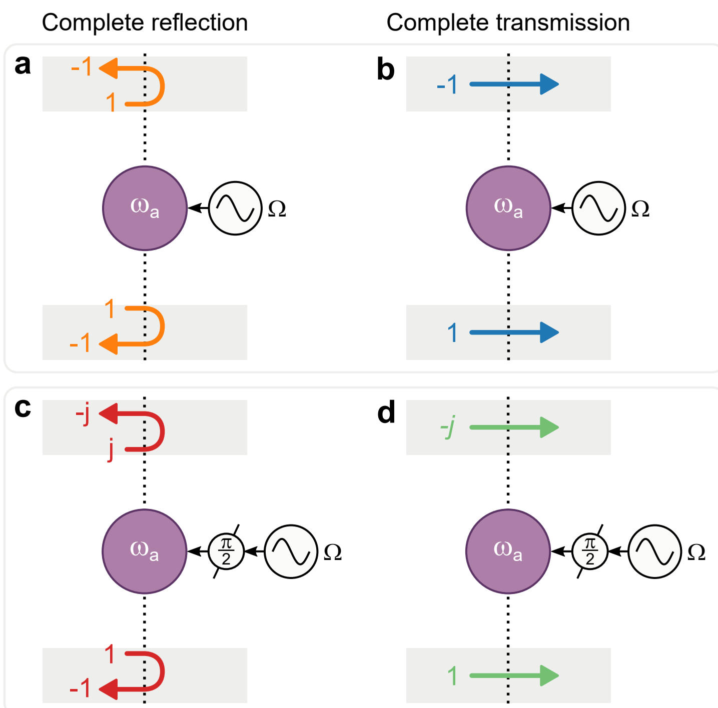

Figure 7.5: A modulation phase of $\phi = 0$ results in (a) complete reflection of the compound even mode $\begin{pmatrix}1 & 1\end{pmatrix}^{\mathrm{T}}$ and (b) complete transmission of the compound odd mode $\begin{pmatrix}1 & -1\end{pmatrix}^{\mathrm{T}}$. A modulation phase of $\phi = \pi/2$ results in (c) complete reflection of the compound even-circular mode $\begin{pmatrix}1 & j\end{pmatrix}^{\mathrm{T}}$ and (d) complete transmission of the compound odd-circular mode $\begin{pmatrix}1 & -j\end{pmatrix}^{\mathrm{T}}$.

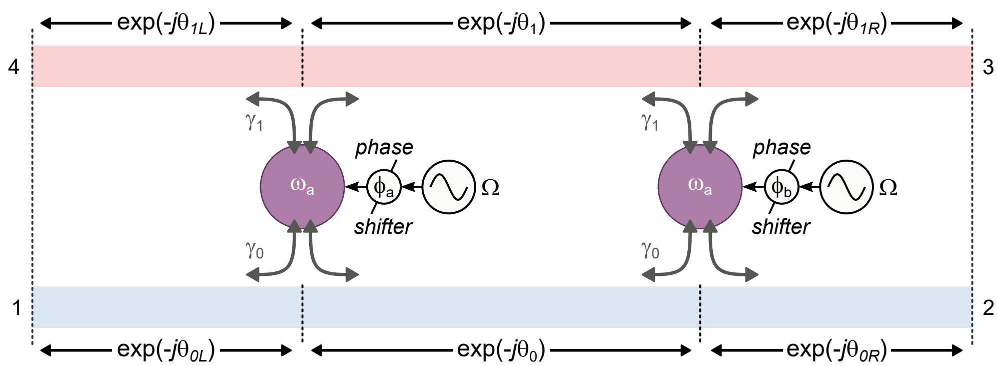

Figure 7.6: Schematic of a dual resonator Floquet circulator with resonators supporting identical modes at frequency ω_a. The resonators are modulated by single-frequency sinusoidal waveforms with fundamental frequency Ω and phases ϕ_a and ϕ_b. The top waveguide (red) targets the $n = 1$ sideband with an evanescent coupling rate of γ_1, and the bottom waveguide (blue) targets the $n = 0$ sideband with an evanescent coupling rate of γ_0. The phase delay between the left reference plane and the left resonator is θ_{0L} and θ_{1L} in the bottom and top waveguide, respectively. The phase delay between the left resonator and the right resonator is θ_0 and θ_1 in the bottom and top waveguide, respectively. The phase delay between the right resonator and the right reference plane is θ_{0R} and θ_{1R} in the bottom and top waveguide, respectively.

7.2.1 Coupled Mode Theory

In terms of the individual waveguide ports modes (rather than the compound waveguide modes), the dual-resonator Floquet system is characterized by the following set of coupled mode equations

$$\frac{d}{dt}\begin{pmatrix}\tilde{a}_1\\ \tilde{a}_2\end{pmatrix} = H\begin{pmatrix}\tilde{a}_1\\ \tilde{a}_2\end{pmatrix} + K\begin{pmatrix}\tilde{s}_{1+} & \tilde{s}_{2+} & \tilde{s}_{3+} & \tilde{s}_{4+}\end{pmatrix}^{\mathrm{T}} \tag{7.18}$$

$$\begin{pmatrix}\tilde{s}_{1-}\\ \tilde{s}_{2-}\\ \tilde{s}_{3-}\\ \tilde{s}_{4-}\end{pmatrix} = C\begin{pmatrix}\tilde{s}_{1+}\\ \tilde{s}_{2+}\\ \tilde{s}_{3+}\\ s_{4+}\end{pmatrix} + D\begin{pmatrix}\tilde{a}_1\\ \tilde{a}_2\end{pmatrix}, \tag{7.19}$$

where $\tilde{a}_1$ and $\tilde{a}_2$ denote the slowly varying envelopes of the modes in the left and the right resonator, respectively and ϕ_a and ϕ_b are their associated modulation phases. For the moment, we assume that the reference planes on the left and right of Fig. 7.6 are moved up to the resonators ($\theta_{0L} = \theta_{1L} = \theta_{0R} = \theta_{1R} = 0$). In this case, the self- and inter-resonator coupling matrix is

$$H = \begin{pmatrix} j\omega_a - \gamma & j\mu - \gamma_0 e^{-j\theta_0} - \gamma_1 e^{-j\theta_1} e^{j(\phi_b - \phi_a)} \\ j\mu - \gamma_0 e^{-j\theta_0} - \gamma_1 e^{-j\theta_1} e^{j(\phi_a - \phi_b)} & j\omega_a - \gamma \end{pmatrix}, \tag{7.20}$$

the input port coupling matrix is

$$K = \begin{pmatrix} j\sqrt{\gamma_0} & j\sqrt{\gamma_0}e^{-j\theta_0} & j\sqrt{\gamma_1}e^{-j\theta_1}e^{-j\phi_a} & j\sqrt{\gamma_1}e^{-j\phi_a} \\ j\sqrt{\gamma_0}e^{-j\theta_0} & j\sqrt{\gamma_0} & j\sqrt{\gamma_1}e^{-j\phi_b} & j\sqrt{\gamma_1}e^{-j\theta_1}e^{-j\phi_b} \end{pmatrix}, \tag{7.21}$$

the output port coupling matrix is

$$D = \begin{pmatrix} j\sqrt{\gamma_0} & j\sqrt{\gamma_0}e^{-j\theta_0} \\ j\sqrt{\gamma_0}e^{-j\theta_0} & j\sqrt{\gamma_0} \\ j\sqrt{\gamma_1}e^{-j\theta_1}e^{j\phi_a} & j\sqrt{\gamma_1}e^{j\phi_b} \\ j\sqrt{\gamma_1}e^{j\phi_a} & j\sqrt{\gamma_1}e^{-j\theta_1}e^{j\phi_b} \end{pmatrix}, \tag{7.22}$$

and the direct port-to-port scattering matrix is

$$C = \begin{pmatrix} 0 & e^{-j\theta_0} & 0 & 0 \\ e^{-j\theta_0} & 0 & 0 & 0 \\ 0 & 0 & 0 & e^{-j\theta_1} \\ 0 & 0 & e^{-j\theta_1} & 0 \end{pmatrix}. \tag{7.23}$$

θ_0 and θ_1 are the transmission phases of the bottom and top waveguides between the resonators shown in Fig. 7.6. Note that $D \neq K^T$ and $\gamma = \gamma_0 + \gamma_1 + \gamma_L$. Throughout the remainder of this chapter we assume that evanescent coupling between the two resonator sites is negligible ($\mu = 0$). The full scattering matrix as a function of the detuning frequency is [173]

$$S^{\mathrm{II}}(\Delta) = C + D \cdot \left[\begin{pmatrix} j\Delta & 0 \\ 0 & j\Delta \end{pmatrix} - H \right]^{-1} \cdot K. \tag{7.24}$$

The phase delays between the individual ports and the resonators can be accounted for through a reference plane shift:

$$S^{\mathrm{II}'} = \begin{pmatrix} e^{-j\theta_{0L}} & 0 & 0 & 0 \\ 0 & e^{-j\theta_{0R}} & 0 & 0 \\ 0 & 0 & e^{-j\theta_{1R}} & 0 \\ 0 & 0 & 0 & e^{-j\theta_{1L}} \end{pmatrix} \cdot S^{\mathrm{II}} \cdot \begin{pmatrix} e^{-j\theta_{0L}} & 0 & 0 & 0 \\ 0 & e^{-j\theta_{0R}} & 0 & 0 \\ 0 & 0 & e^{-j\theta_{1R}} & 0 \\ 0 & 0 & 0 & e^{-j\theta_{1L}} \end{pmatrix} \tag{7.25}$$

where the individual phases are shown in Fig. 7.6. In the expression above, $S^{\mathrm{II}'}$ refers to the full scattering matrix of the system in Fig. 7.6. For the remainder of this chapter we drop the $(\cdot)'$ notation and use S^{II} in reference to the system in Fig. 7.6. The compound modes on the left and the right reference planes constitute the four ports of the system after rotation into the compound mode basis. We denote the ports as $\alpha_E = \begin{pmatrix} 1 & 1 \end{pmatrix}^{\mathrm{T}}$ and $\alpha_O = \begin{pmatrix} 1 & -1 \end{pmatrix}^{\mathrm{T}}$ on the left, and $\beta_E = \begin{pmatrix} 1 & 1 \end{pmatrix}^{\mathrm{T}}$ and $\beta_O = \begin{pmatrix} 1 & -1 \end{pmatrix}^{\mathrm{T}}$ on the right. Here the first (second) vector element indicates the amplitude of the mode in the bottom (top) waveguide.

7.2.2 Operating Conditions

Realization of a circulator using the system in Fig. 7.6 requires the second resonator have a $\pi/2$ relative phase shift applied to its modulating wave, e.g. ϕ_b - ϕ_a = $\pi/2$, as well as critical coupling of the resonators to the individual waveguides, e.g. γ_0 = γ_1 = $\gamma/2$. Additionally, the bottom and top waveguides are designed to introduce different propagation phase delays at each stage within the system, which we characterize using the following *relative* phase delay parameters

$$\Delta\theta_L = \theta_{1L} - \theta_{0L} \tag{7.26}$$

$$\Delta\theta = \theta_1 - \theta_0 \tag{7.27}$$

$$\Delta\theta_R = \theta_{1R} - \theta_{0R}. \tag{7.28}$$

A variety of pathways for circulation can be realized, depending on the particular combination of $\Delta\theta_L$, $\Delta\theta$, and $\Delta\theta_R$. First we consider the case of $\Delta\theta_L = 0$, $\Delta\theta = \pi/2$, and $\Delta\theta_R = \pi/2$ which corresponds to the first row of Table 7.1. In this configuration circulation occurs between three of the four modes (α_O, β_O, and β_E) while one out of the four modes is functionally disconnected from the system (α_E). On-resonance power transmission is unity in the forward direction, defined as $\alpha_O \to \beta_O \to \beta_E \to \alpha_O$, and is completely suppressed in the backward direction.

Considering the relationship $\theta_0 = \theta_1 + \Delta\theta$, the condition for ideal isolation between α_O and β_O is

$$e^{2j\theta_0}\left(e^{j\Delta\theta} - j\right)\left(je^{j\Delta\theta+2j\theta_0} + e^{2j\Delta\theta+2j\theta_0} - je^{j\Delta\theta} - 1\right) = 0 \tag{7.29}$$

which is satisfied by $\Delta\theta = \pi/2$, independently of the value of θ_0. Ideal operation between β_E and α_O translates to a slightly different expression given by

$$-e^{2j\theta_0}\left(e^{j\Delta\theta} - j\right)\left(e^{2j(\Delta\theta+\theta_0)} - je^{j(\Delta\theta+2\theta_0)} + je^{j\Delta\theta} - 1\right) = 0 \tag{7.30}$$

which is satisfied by the same condition $\Delta\theta = \pi/2$. The overall dispersive scatte-

Reflected	Circulation	$\phi_b - \phi_a$	$\Delta\theta_L$	$\Delta\theta$	$\Delta\theta_R$
α_E	$\alpha_O \to \beta_O \to \beta_E \to \alpha_O$	$\frac{\pi}{2}$	0	$\frac{\pi}{2}$	$\frac{\pi}{2}$
	$\alpha_O \to \beta_O \to \beta_E \to \alpha_O$	$\frac{\pi}{2}$	0	$\frac{3\pi}{2}$	$\frac{\pi}{2}$
	$\alpha_O \to \beta_E \to \beta_O \to \alpha_O$	$\frac{\pi}{2}$	0	$\frac{\pi}{2}$	$\frac{3\pi}{2}$
	$\alpha_O \to \beta_E \to \beta_O \to \alpha_O$	$\frac{\pi}{2}$	0	$\frac{3\pi}{2}$	$\frac{3\pi}{2}$
α_O	$\alpha_E \to \beta_O \to \beta_E \to \alpha_E$	$\frac{\pi}{2}$	π	$\frac{\pi}{2}$	$\frac{\pi}{2}$
	$\alpha_E \to \beta_O \to \beta_E \to \alpha_E$	$\frac{\pi}{2}$	π	$\frac{3\pi}{2}$	$\frac{\pi}{2}$
	$\alpha_E \to \beta_E \to \beta_O \to \alpha_E$	$\frac{\pi}{2}$	π	$\frac{\pi}{2}$	$\frac{3\pi}{2}$
	$\alpha_E \to \beta_E \to \beta_O \to \alpha_E$	$\frac{\pi}{2}$	π	$\frac{3\pi}{2}$	$\frac{3\pi}{2}$

Table 7.1: Summary of on-resonance reflection and nonreciprocal scattering for various waveguide phase delay configurations.

ring matrix of the system becomes a unique circulator response given by

$$S_c^{\mathrm{II}} = \begin{array}{c} \begin{array}{cccc} \alpha_E & \alpha_O & \beta_E & \beta_O \end{array} \\ \begin{pmatrix} -\frac{\gamma}{\gamma+j\Delta} & -\frac{j\gamma\Delta}{(\gamma+j\Delta)^2} & 0 & \frac{\Delta^2}{(\Delta-j\gamma)^2} \\ 0 & 0 & 1 & 0 \\ 0 & \frac{j\Delta}{\gamma+j\Delta} & 0 & -\frac{\gamma}{\gamma+j\Delta} \\ \frac{j\Delta}{\gamma+j\Delta} & \frac{\gamma^2}{(\gamma+j\Delta)^2} & 0 & -\frac{j\gamma\Delta}{(\gamma+j\Delta)^2} \end{pmatrix} \end{array} \begin{array}{c} \alpha_E \\ \alpha_O \\ \beta_E \\ \beta_O \end{array} . \tag{7.31}$$

The on-resonance operation of the Floquet circulator can be understood by tracing a compound mode, as it travels through the system and becomes transformed by the segments of waveguides and as it reflects and transmits through the resonators (Fig. 7.7). For the $\beta_E \to \alpha_O$ path, the signal enters as the even mode $\begin{pmatrix}1 & 1\end{pmatrix}^{\mathrm{T}}$ on the right, and is transformed into the circular mode, $\begin{pmatrix}1 & -j\end{pmatrix}^{\mathrm{T}}$, by the dual-waveguide segment between the resonator and the ports on the right. This circular mode, $\begin{pmatrix}1 & -j\end{pmatrix}^{\mathrm{T}}$, perfectly transmits through the right resonator (as shown in Fig. 7.5d with $\phi = \pi/2$). Propagation down the middle waveguide segment transforms the signal into the odd mode, $\begin{pmatrix}1 & -1\end{pmatrix}^{\mathrm{T}}$ which then impinges on the left resonator and is perfectly transmitted out the other side (as shown in Fig. 7.5b

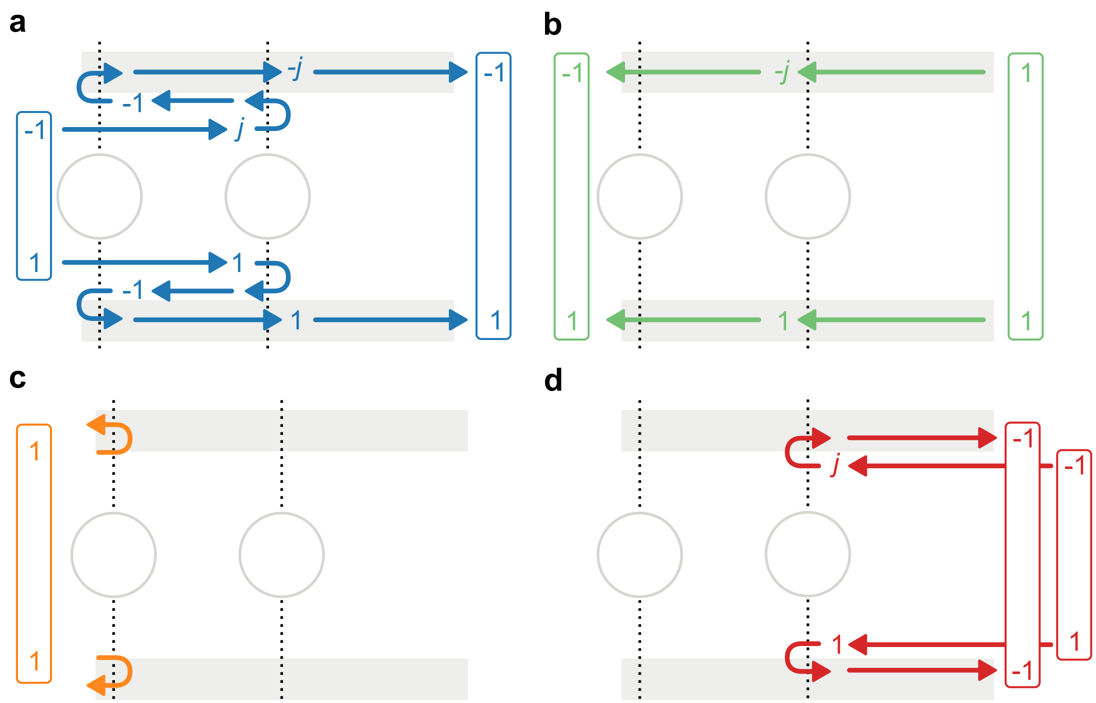

Figure 7.7: (a) Incidence of odd mode $\begin{pmatrix}1 & -1\end{pmatrix}^{\mathrm{T}}$ from the left undergoes two reflections before being resonantly transmitted out of the right side. (b) Incidence of the even mode $\begin{pmatrix}1 & 1\end{pmatrix}^{\mathrm{T}}$ from the right is non-resonantly transmitted to the odd mode $\begin{pmatrix}1 & -1\end{pmatrix}^{\mathrm{T}}$ on the left. (c) Incidence of the even mode $\begin{pmatrix}1 & 1\end{pmatrix}^{\mathrm{T}}$ from the left is resonantly reflected back into the even mode $\begin{pmatrix}-1 & -1\end{pmatrix}^{\mathrm{T}}$. (d) Incidence of the odd mode $\begin{pmatrix}1 & -1\end{pmatrix}^{\mathrm{T}}$ from the right is resonantly reflected back into the even mode $\begin{pmatrix}-1 & -1\end{pmatrix}^{\mathrm{T}}$ on the right. Note that this sketch assumes positive phase accumulation in the waveguides (clock-wise rotation in the complex plane) as is the case in the CROW used in Section 7.3.1.

with $\phi = 0$). Note that the complete forward transmission from $\beta_E \rightarrow \alpha_O$ is due to the lack of coupling to either resonator, which holds even when the input signal is off-resonance. As a result, the forward transmission is unitary regardless of the detuning as expected from the expression in Eqn. 7.31 and as shown in Fig. 7.8a. The backward transmission is resonantly suppressed, with a 30 dB isolation bandwidth of $\sim 0.07\gamma$. Such broadband complete transmission in the forward direction is spectrally distinct from that of conventional three-port junction circulators and four-port circulators.

Transmission along the $\alpha_O \rightarrow \beta_O$ path (Fig. 7.8a, solid blue curve) can be analyzed similarly, with multiple reflections between the two resonators before the signal emerges (Fig. 7.7). This pair of ports provides a $70\times$ larger isolation bandwidth ($\sim 5\gamma$) than the previous pair (Fig. 7.8b), but at a cost of reduced forward transmission off-resonance. Ultimately, γ and the associated operating bandwidth is limited by the fundamental frequency of the modulating wave and the and the propagation of the coupling waveguides. The remaining ports in the system do not participate in any cross-device scattering pathways: the even mode on the left resonantly reflects into itself $\alpha_E \rightarrow \alpha_E$ (Fig. 7.8a, dashed orange curve), and the even mode on the right resonantly reflects into the odd mode on the right $\beta_O \rightarrow \beta_E$ (Fig. 7.8a, solid red curve).

On-resonance this results in the response

$$S_c^{\mathrm{II}}(\Delta = 0) = \begin{pmatrix} -1 & 0 & 0 & 0 \\ 0 & 0 & 1 & 0 \\ 0 & 0 & 0 & -1 \\ 0 & 1 & 0 & 0 \end{pmatrix}, \tag{7.32}$$

while off-resonance the scattering is reciprocal with the response

$$S_c^{\mathrm{II}}(\Delta \rightarrow \infty) = \begin{pmatrix} 0 & 0 & 0 & 1 \\ 0 & 0 & 1 & 0 \\ 0 & 1 & 0 & 0 \\ 1 & 0 & 0 & 0 \end{pmatrix}. \tag{7.33}$$

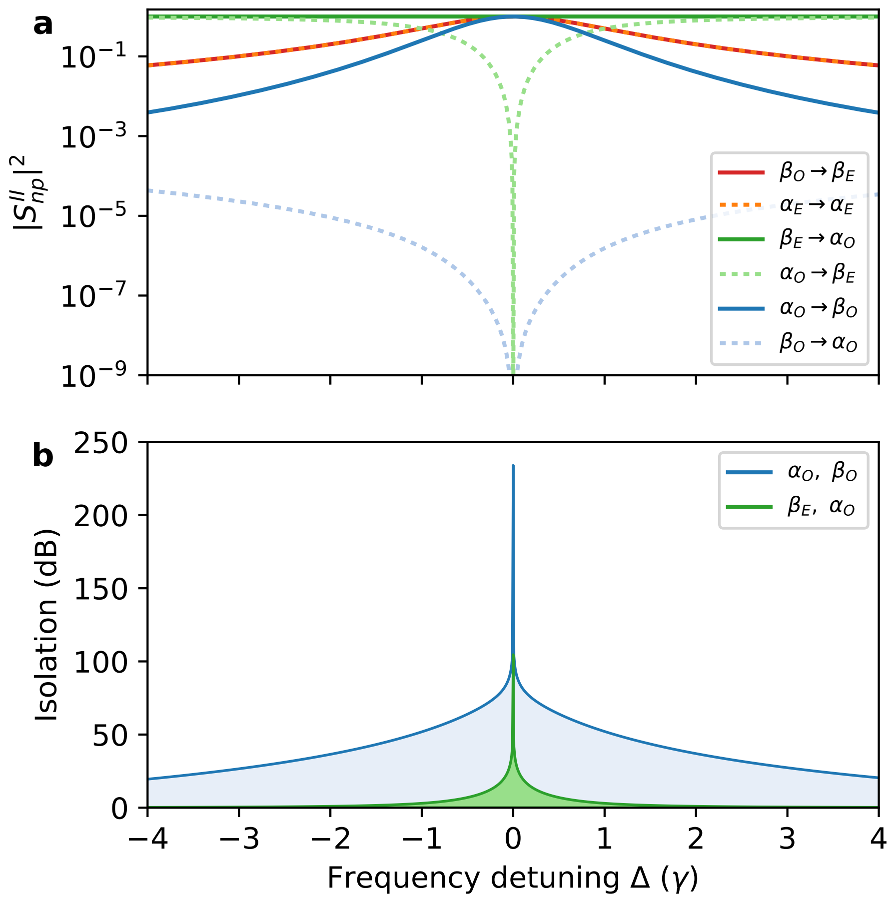

Figure 7.8: (a) Scattering parameter spectra for three forward signal pathways ($\beta_E \to \alpha_O \to \beta_O \to \beta_E$), demonstrating on-resonance signal circulation. Dashed curves show suppressed backward transmission. The frequency detuning parameter Δ represents the signal frequency relative to the optical carrier, in units of γ. (b) Isolation between the two cross-device pathways $\{\alpha_O \to \beta_O, \beta_O \to \alpha_O\}$ and $\{\beta_E \to \alpha_O, \alpha_O \to \beta_E\}$.

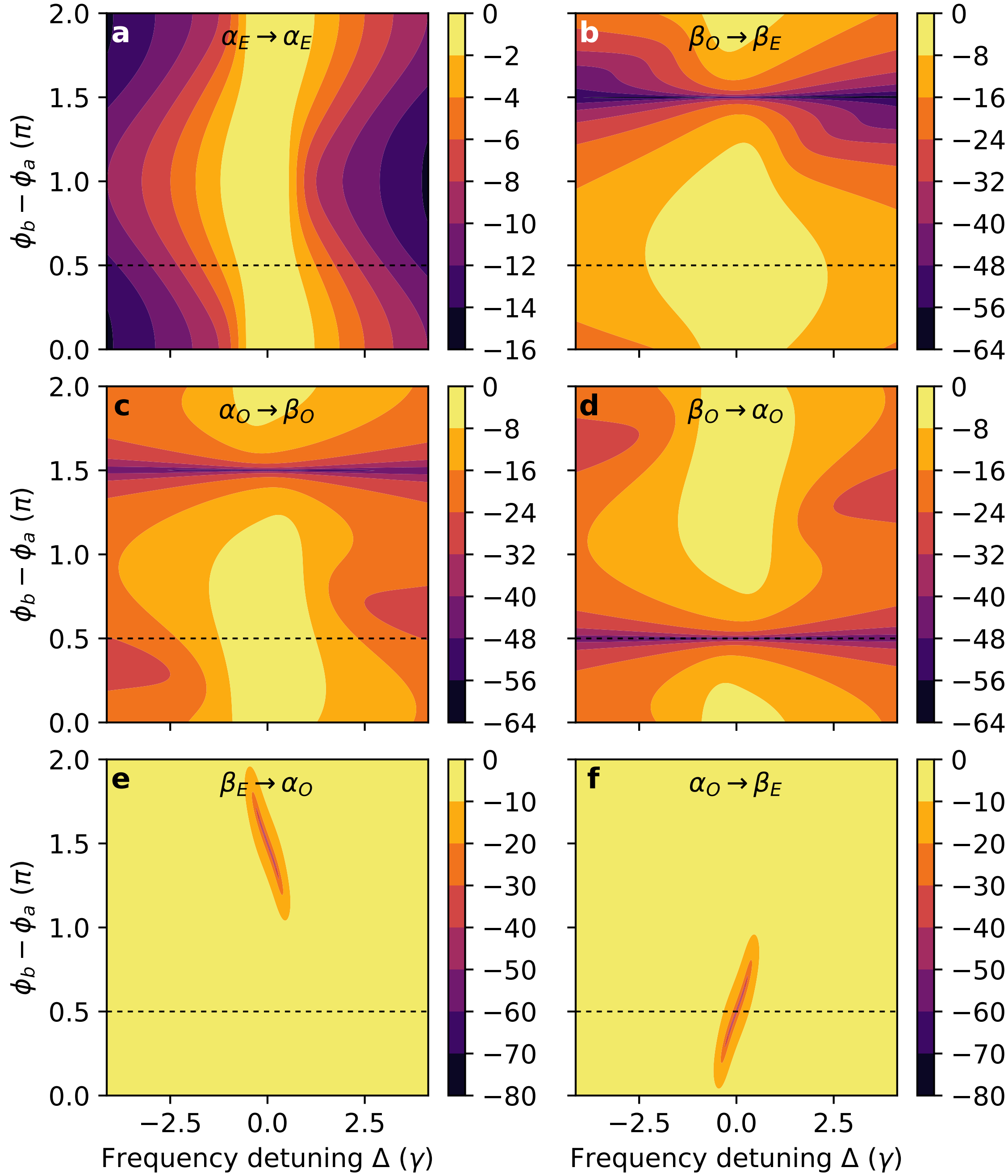

Figure 7.9: Scattering parameter dependence on relative phasing of the modulation waves parameterized by $\phi_b - \phi_a$. In all panels $\phi_a = 0$ and ϕ_b is varied from 0 to 2π (vertical axis). The contours are $|T|^2$ in dB for (a) $\alpha_E \to \alpha_E$, (b) $\beta_O \to \beta_E$, (c) $\alpha_O \to \beta_O$, (d) $\beta_O \to \alpha_O$, (e) $\beta_E \to \alpha_O$, (f) $\alpha_O \to \beta_E$. The horizontal dashed line indicates the $\phi_b - \phi_a = \pi/2$ condition used in the previous sections.

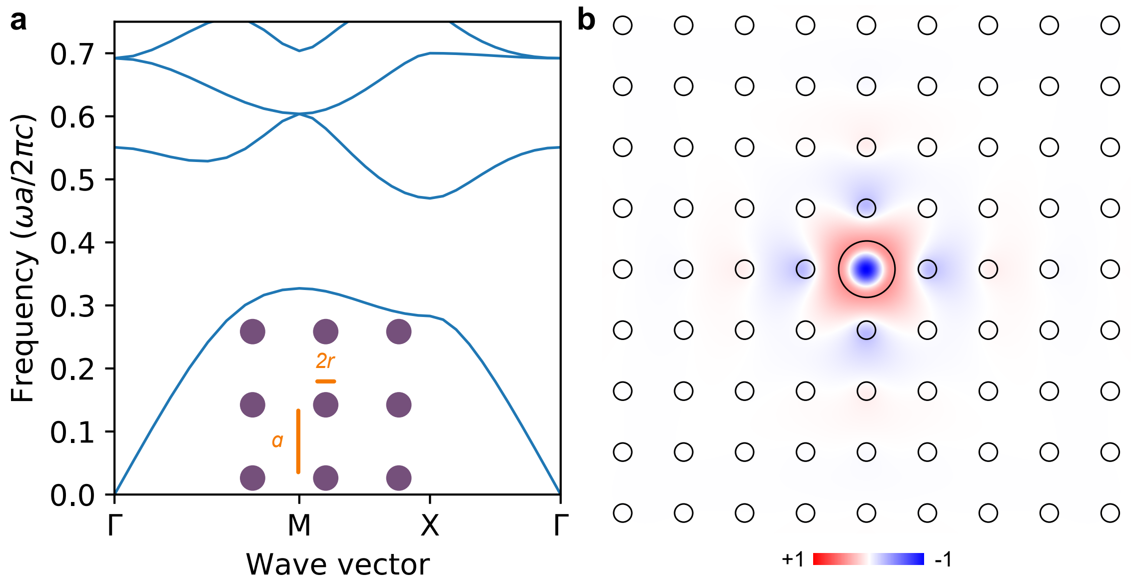

Figure 7.10: (a) Photonic band structure for the TM polarization in a 2D square lattice of silicon rods with $r = 0.15a$, $n_0 = 3.5$ embedded in air. (b) Instantaneous electric field distribution $\mathrm{Re}\,(\mathbf{E}_z)$ of the monopole mode of an enlarged point defect formed by an enlarged silicon rod with $r_c = 0.46a$.

7.3 Implementation

Thus far we have only considered a general coupled mode theory model of the Floquet circulator. We now consider the details of implementing the Floquet circulator in an on-chip photonic platform.

7.3.1 2D Photonic Crystal

The photonic crystal implementation of the circulator system is based on a 2D square lattice of dielectric rods ($r = 0.15a$, $\epsilon_r = 12.25$) embedded in air, which supports a large TM photonic band gap (Fig. 7.10a). The bandwidth of the band gap is orders of magnitude larger than the modulation rate, which eliminates radiation loss of the sidebands not targeted by the two coupling waveguides. Each parametrically modulated resonator is a point defect formed by an enlarged rod that supports a monopole mode (Fig. 7.10b) at frequency $\omega_a = 0.39685\,(2\pi c/a)$, where the refractive index of the rod is modulated by a sinusoid of frequency $\Omega = 0.0025\omega_a$.

The two narrowband waveguides are coupled-resonator optical wavegui-

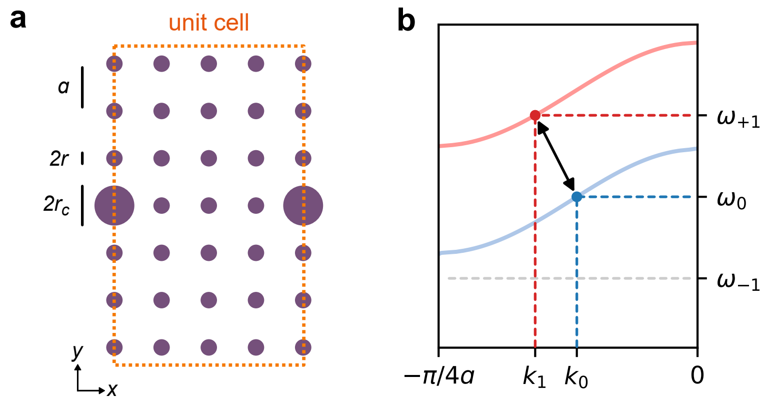

Figure 7.11: (a) A coupled resonator optical waveguide (CROW) is formed in the x-direction by enlarging every fourth rod. The bulk crystal is defined as in Fig. 7.10a. (b) Dispersion for the upper (red curve) and the lower (blue curve) waveguides of Fig. 7.6. The bands are detuned from each other by having $r_c = 0.4630a$ $(0.4649a)$ in the top (bottom) waveguide. ω_n indicates the sideband frequency component for $n = \{-1,\ 0,\ +1\}$ and k_n indicates the associated CROW wavevector.

des (CROWs) [175] formed by a 1D array of enlarged rods (Fig. 7.11a). The CROW period is $4a$, resulting in a propagation bandwidth of $0.0024\omega_a$, and the enlarged rod radius of each CROW is slightly different $r_c = 0.4630a$ v.s. $r_c = 0.4649a$ such that the top waveguide targets only the $n = +1$ sideband (Fig. 7.11b, blue) and the bottom waveguide targets only the $n = 0$ sideband (Fig. 7.11b, red). The $n = -1$ sideband (Fig. 7.11b, dashed grey) and all other sideband orders are dark to the outside environment as they couple to neither the waveguides nor the bulk crystal. The coupling rates γ_0 and γ_1 can be changed in a step-wise fashion through conventional structural tuning (i.e. adjusting the number of crystal periods between the waveguide and resonator), but as predicted by Eqn. 7.7 and 7.8, the modulation index provides continuous tuning of γ_0 and γ_1 to realize critical coupling (Fig. 7.12). Here the coupling rates are obtained from fitting the spectral response of a photonic crystal Floquet resonator to coupled mode theory. To realize the phase delay condition of $\Delta\theta = \pi/2$ in the circulator, the two resonators are separated by a distance of $16a$ (4 CROW periods).

The response of the Floquet circulator is demonstrated using first-principle finite element frequency domain simulations, with no approximations except for discretization. The electromagnetic wave equations at each sideband frequency

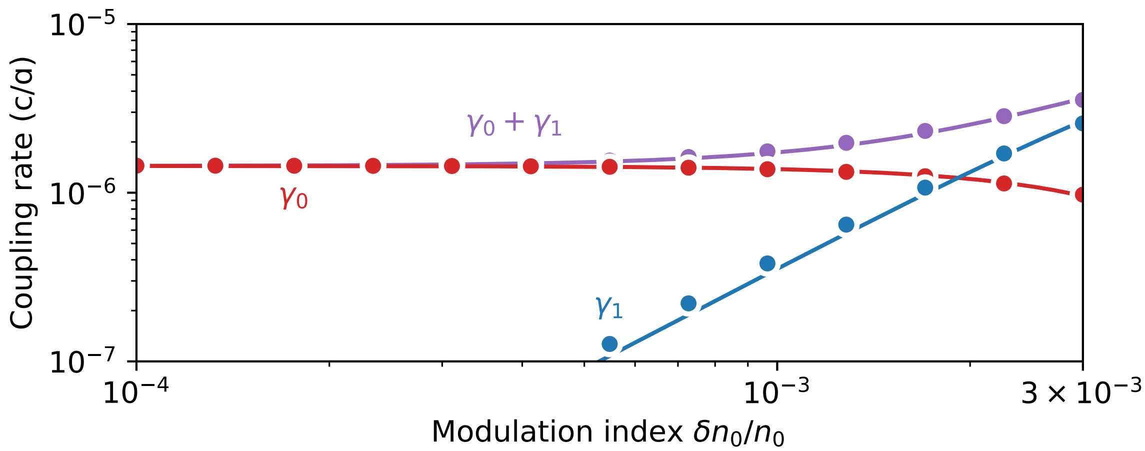

Figure 7.12: Coupling rates to top (γ_1) and bottom (γ_0) waveguide as a function of modulation index, defined by the peak change in refractive index, $\delta n_0/n_0$. Critical coupling $(\gamma_0 = \gamma_1)$ occurs for $\delta n_0/n_0 = 1.84 \times 10^{-3}$. Coupling rates (circles) are calculated by fitting the response of a full-wave simulation of a single side-coupled modulated resonator to coupled mode theory. The lines represent a fitting of the circles to the expressions for the coupling rates given by Eqns. 7.8 and assuming that the relative amplitudes depend on the modulation index through Bessel functions of the first kind. The mismatch between the line and circles for low γ_1 is likely due to a poor fitting of γ_1 when $\gamma_1 \ll \gamma_0$.

are coupled to capture the effect of modulation and are solved simultaneously (see Methods section). As predicted by the coupled mode theory, the calculated transmission for the $\beta_E \rightarrow \alpha_O$ pathway exhibits broadband unity transmission (dark green dots, Fig. 7.13a) while the transmission in the backward direction $\alpha_O \rightarrow \beta_E$ is resonantly suppressed (light green dots, Fig. 7.13a), with over 20 dB isolation (Fig. 7.13b). Meanwhile, the alternative $\alpha_O \rightarrow \beta_O$ pathway exhibits unity transmission on resonance (dark blue dots, Fig. 7.13a) and nearly 80 dB suppression in backward transmission along $\beta_O \rightarrow \alpha_O$ (light blue dots, Fig. 7.13a), with a 30 dB isolation bandwidth of $\sim 4\gamma$. Note that the non-ideal line shape and reduced peak isolation observed in Fig. 7.13b are the result of a numerical mismatch between γ_0 and γ_1 and deviation of the waveguide phase delays from the condition $\Delta\theta = \pi/2$. Although the peak isolation is reduced to 80 dB, the broad bandwidth with above 45 dB isolation is crucial to avoiding coherence collapse in laser diodes1. In practice, a non-sinusoidal modulation waveform can be used to fine-tune the system closer to the critical coupling and phase delay conditions.

The strongly nonreciprocal on-resonance circulator functionality is evident in the field distributions showing the energy density aggregated over all sidebands, $\sum_n \left|\mathbf{E}^{(n)}(\Delta = 0)\right|^2$. The even mode entering from port one is completely disconnected from the other ports and resonantly reflects back into itself (Fig. 7.14a) while the port two odd mode also resonantly reflects back but is converted into the even mode (Fig. 7.14b). In both cases, transmission across the device is strongly suppressed. On the other hand, the odd mode from port one is fully transmitted into the odd mode at port two where a resonant scattering is observed from the greater energy in the resonator sites (Fig. 7.14c). As expected from the discussion earlier, the broadband forward transmission ($\beta_E \rightarrow \alpha_O$) is clearly non-resonant, as seen from the comparable field magnitudes in the resonator and waveguide modes (Fig. 7.14d).

The Floquet circulator can be realized with a wide range of integrated photonic platforms and modulation mechanisms. The 2D photonic crystal structure presented here can be readily extended to photonic crystal slab structures with experimentally demonstrated quality factors that exceed 10^6 [176], [177]. The two narrowband waveguides can, in principle, be merged into a single waveguide with a bandwidth spanning both the $n = 0$ and the $n = 1$ sidebands, provided that

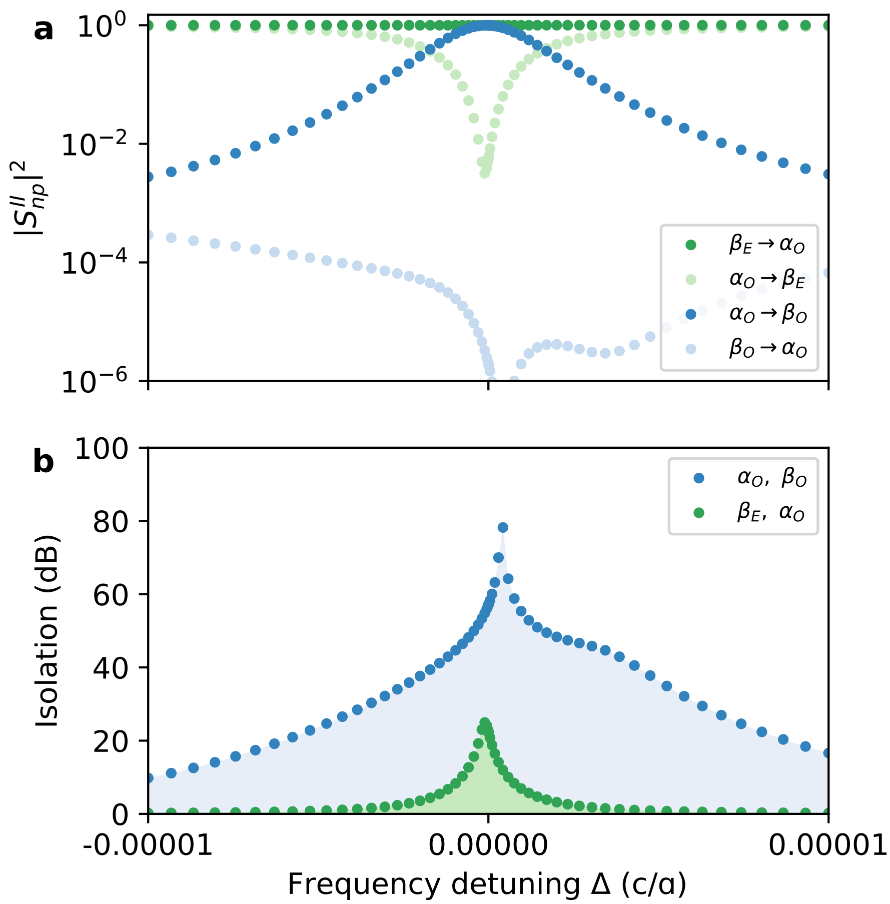

Figure 7.13: (a) Calculated nonreciprocal scattering parameter spectra and (b) isolation spectra for the two cross-device pathways for a Floquet circulator implemented following Fig. 7.11

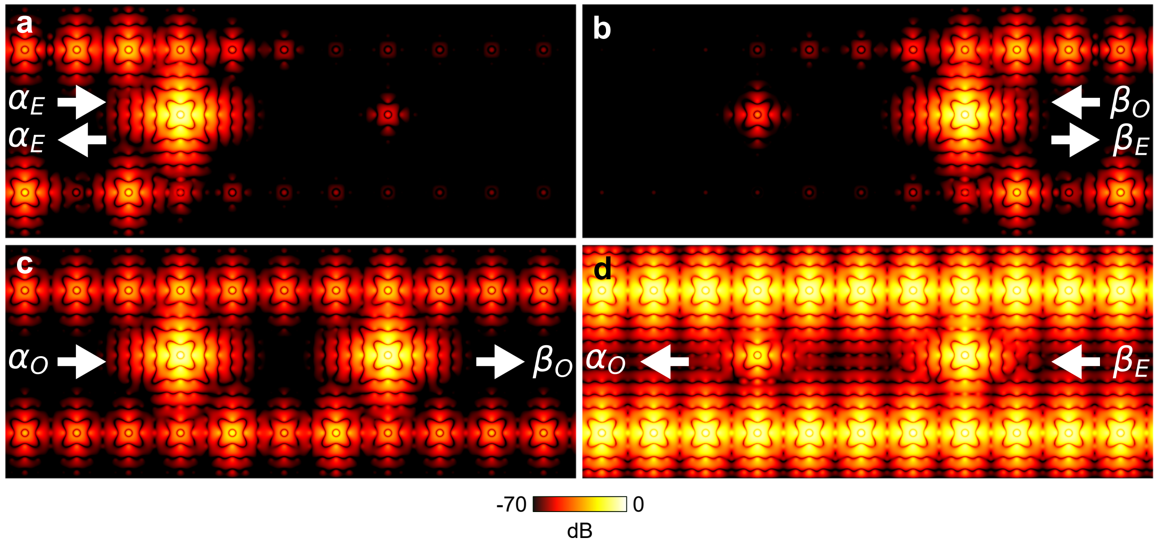

Figure 7.14: On-resonance electric field distributions summed over all sidebands, $\sum_n \left|\mathbf{E}^{(n)}{}_{\Delta=0}\right|^2$ for forward and backward incidence along the cross-device pathways. Complete reflection evident along the backward directions in (a) and (b), while complete transmission is observed along the forward directions in (c) and (d).

the waveguide dispersion is sufficiently large to generate the $\Delta\theta = \pi/2$ differential phase shift. Additionally, the narrowband waveguides could also be realized with mechanisms other than a CROW, such as electromagnetically induced transparency or periodically modulated waveguides.

7.3.2 Operation at 1550 nm

Note that this particular photonic crystal configuration is chosen to clearly illustrate the device operation in a compact area. The structural coupling between the resonator and the waveguides is not highly asymmetric (Fig. 7.14), with a separation of $5a$ $(4a)$ between the resonators and the bottom (top) waveguide. The difference of only one unit cell requires a relatively large modulation index, $\delta n_0/n_0 = 1.84 \times 10^{-3}$ to satisfy the critical coupling condition given by Eqn. 7.9, in this case with a relative sideband amplitude of $u^{(1)} \approx 0.3$ (Fig. 7.15). Additional rods between the two resonators and the bottom CROW would allow the modulation index to be reduced by several orders of magnitude.

To operate at 1550 nm, the lattice constant of the photonic crystal in this design would be a = 615 nm, with a modulation frequency Ω = 484 GHz, and total quality factor $Q = \omega_a / (2\gamma_0 + 2\gamma_1) = 8.3 \times 10^4$ (2.34 GHz linewidth). The resonator linewidth is smaller than the modulation rate by a factor of approximately 200 which means that the CROW bandwidth is the limiting factor for a reduced modulation frequency. Fig. 7.2 at the beginning of the chapter summarizes the requirements of the various spectral features of the system. In order to consider an experimentally achievable modulation frequency of 20 GHz [178], [179], the number of rods between the enlarged defect rods of the CROW's can be doubled (corresponding to a new CROW unit cell width of $7a$). This results in a CROW bandwidth of $9.3 \times 10^{-5}\omega_a$ (18 GHz) that is still nearly an order of magnitude larger than the resonator linewidth used in the existing photonic crystal simulation. Note that this only results in a doubling in size of one dimension of the system. The resulting footprint of the overall device is $56a \times 17a$ $(22.20\lambda_0 \times 6.75\lambda_0)$.

The waveguide mode dispersion could be engineered to provide the required relative phase shifts ($\Delta\theta$ and $\Delta\theta_R$) in a smaller physical footprint. For example, different positions of the band could be sampled to provide a larger phase shift over a distance of a single CROW period. The trade off in this approach is the significant reduction in group velocity towards the edges of the CROW bandwidth. Another option would be to use a *single* waveguide with a bandwidth that spans two adjacent sideband states. In this case, the waveguide dispersion could be sampled by adjusting the modulation frequency Ω to provide the required $\Delta\theta$ and $\Delta\theta_R$.

Deviation from the critical coupling condition $\gamma_1 = \gamma_0$ reduces the isolation performance of the Floquet circulator but not the insertion loss (Fig. 7.16).

7.3.3 Modulation Schemes

A unique advantage of the Floquet circulator is that the use of more general periodic modulation waveforms beyond simple sinusoidal modulation relaxes the need for large modulation frequency and depth. In particular, the large modulation depth required to reach critical coupling between the waveguides of the simulated photonic crystal would result in an overwhelming resonator absorption rate, $\gamma_L \gg (\gamma_0, \gamma_1)$ (Fig. 7.18a). Although the structural coupling factors, d_0 and d_1 can be increased (Fig. 7.18b), that would require a larger modulation frequency and CROW bandwidth.

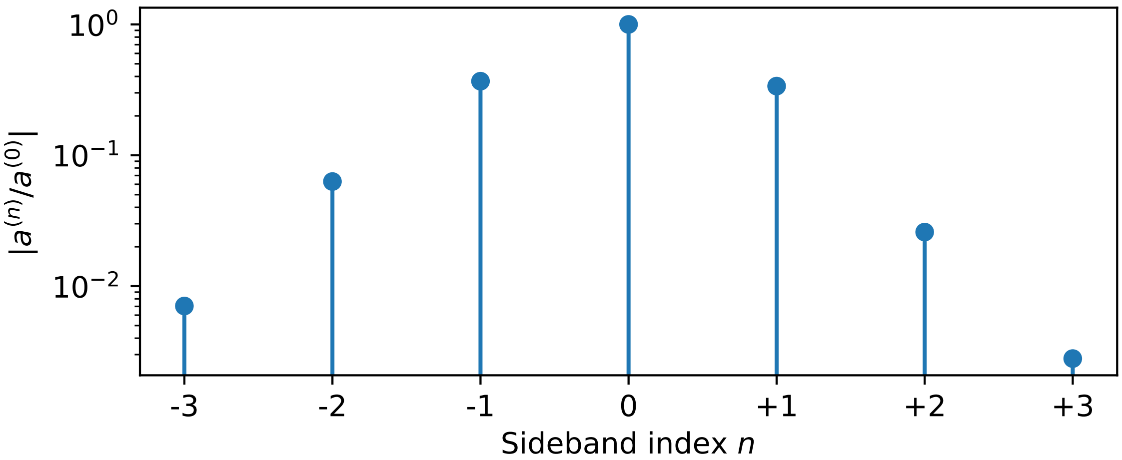

Figure 7.15: Sideband amplitude distribution in the left resonator of the photonic crystal Floquet circulator. The distribution was numerically computed in COMSOL Multiphysics under on-resonance excitation of the compound even mode from the left port (Fig. 7.14a). Note that the sideband amplitude distribution does not qualitatively depend on the compound mode being excited or on the resonator site (left versus right).

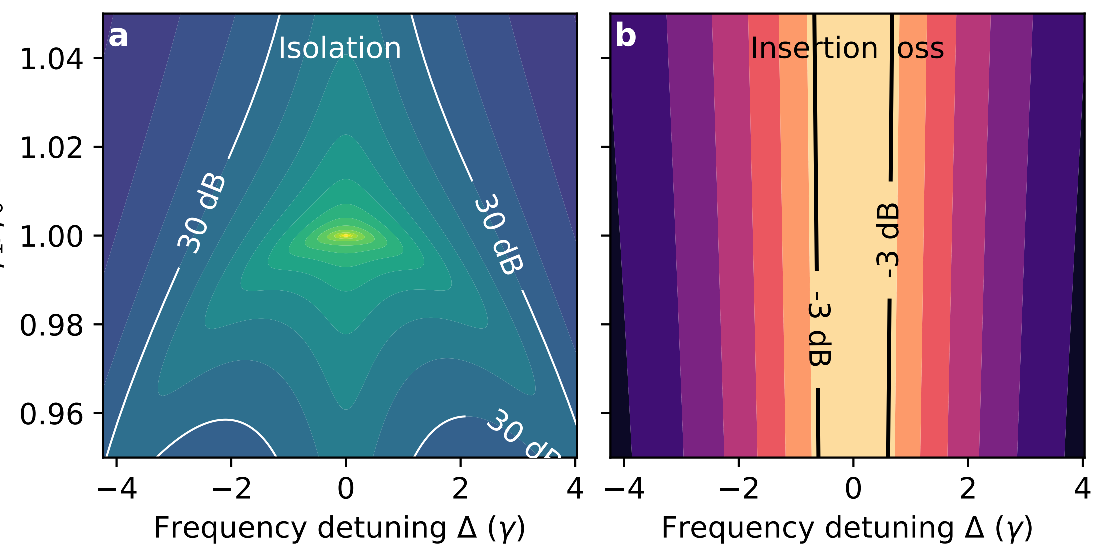

Figure 7.16: Sensitivity of the $\alpha_O \to \beta_O$ pathway to mismatch in the coupling rates to the top and bottom waveguides. (a) Isolation and (b) insertion loss as a function of frequency and the ratio γ_1/γ_0. A values of $\gamma_1/\gamma_0 = 1$ corresponds to a critically coupled system where the isolation is maximized.

However, by using a modulating wave with comparable fundamental and second harmonic components (Fig. 7.17b), equal amplitudes of $u^{(1)}$ and $u^{(2)}$ can be supported without resorting to an extremely large modulation index to boost the amplitudes of higher order sidebands in the Jacobi-Anger expansion (Fig. 7.17a).

The system described in the previous section can be implemented using the $n = 1$ and the $n = 2$ sidebands, with the $n = 2$ sideband playing the role of the $n = 0$ sideband. The critical coupling condition given in Eqn. 7.9 results in a nearly symmetric structure where $|d_0| \sim |d_1|$. In practice, the exact critical coupling condition could be satisfied by fine-tuning the relative ratio between the fundamental and the second harmonic components in the modulating waveform, which in turn determines the required ratio $\left|u^{(1)}\right| / \left|u^{(2)}\right|$. This would allow a wide range of absolute modulation index $\left|u^{(1)}\right|$ to be used from various modulation schemes. In contrast, under practical single-frequency modulation, $\left|u^{(0)}\right|$ is expected to be nearly unity and only one particular modulation index $\left|u^{(1)}\right| = |d_0| / |d_1|$ satisfies the critical coupling condition given in Eqn. 7.9. The only constraint for such a system under the generalized modulation is that radiation and absorption loss need to be small to ensure complete transmission on resonance, e.g. $|d_0|^2 \left|u^{(2)}\right|^2 + |d_1|^2 \left|u^{(1)}\right|^2 \gg \gamma_L$ as shown in Fig. 7.18c. As γ_L becomes comparable to γ_0 and γ_1, the $\alpha_O \rightarrow \beta_O$ pathway experiences higher insertion loss but maintains a high isolation. However, the $\beta_E \rightarrow \alpha_O$ pathway experiences reduced isolation for larger γ_L with no increase in insertion loss (Fig. 7.19).

7.3.4 Single-carrier to Dual-carrier Conversion

The unusual dual-carrier response necessitates an additional photonic circuit to modulate and demodulate traditional single-carrier optical signals to the dual-carrier format (Fig. 7.20), or a spatial mode multiplexer to separate the even and odd compound modes on the right-hand side of the device. The signal incident through port one of Fig. 7.20 can be resonantly split into the compound mode defined over ports two and three. This device can also operate in the opposite direction to convert a dual-carrier signal back to a single-carrier signal. Entire photonic circuits using such Floquet circulators can be constructed to use the dual-carrier compound modes as signal carriers, thereby reducing the need for such

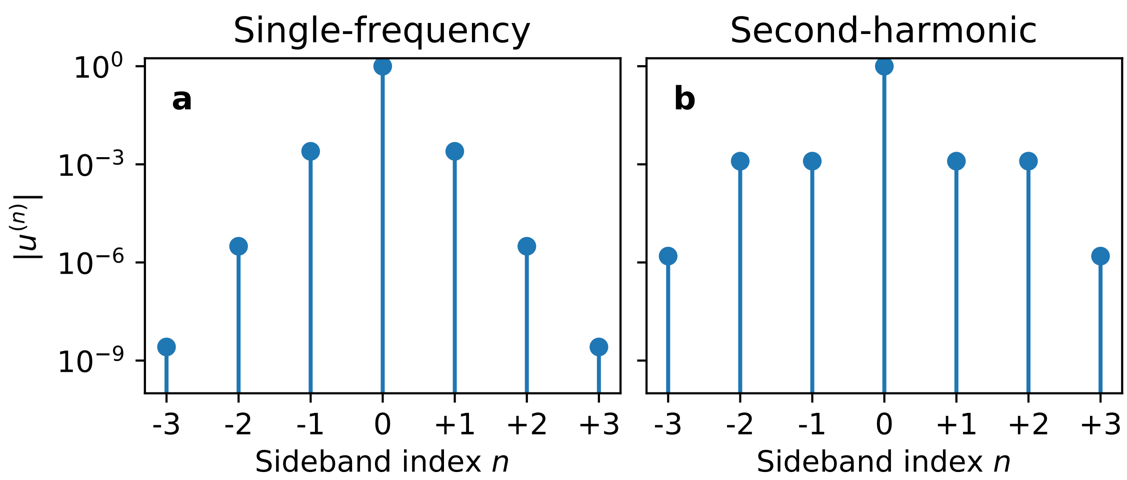

Figure 7.17: Floquet sideband amplitude distributions for single frequency and second harmonic parametric modulation. Single frequency modulation (left) has modulation of the form $f(t) = 1 + \delta \cos(\Omega t)$ and second harmonic (right) has the form $f(t) = 1 + \delta_1 \cos(\Omega t) + \delta_2 \cos(2\Omega t)$ where $\delta_2 = 2\delta_1$. Sideband amplitudes were computed by numerically solving the Mathieu equation using the harmonic balance method [180], [181].

mode converters only at the input and the output of the overall circuit. Systems which consider sideband states as an additional dimension would be compatible with this idea [165], [183].

7.4 Comparison

A key advantage of the Floquet circulator over conventional junction circulators is that its operation does not rely on breaking the degeneracy of two resonant modes with high rotational symmetry. The Floquet circulator requires no such rotational symmetry, resulting in relaxed design constraints and robustness towards fabrication imperfections. More importantly, all sidebands of the two Floquet resonators remain matched in frequency, and by introducing a functionally disconnected fourth port (α_E in the configuration considered previously) the system achieves simultaneous broadband and unity transmission in the forward direction with perfect on-resonance isolation.

Although there is a superficial structural resemblance between the Floquet circulator and circulators based on parametric conversion and commutation [150],

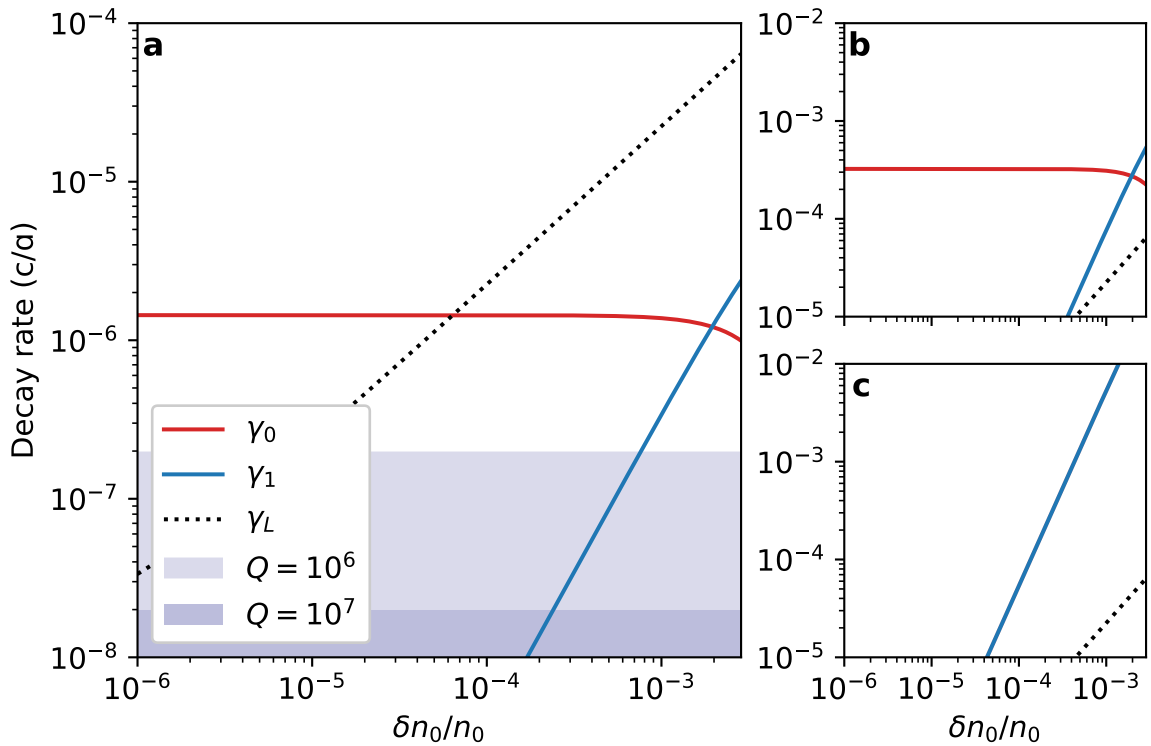

Figure 7.18: Resonator decay rates to bottom waveguide γ_0, top waveguide γ_1, and absorption where γ_L is the intrinsic decay rate from an eigenmode simulation of the point defect (Fig. 7.10b) where the dielectric loss tangent applied to the enlarged defect rod was mapped to the relative change in refractive index through the data in [182]. The top edges of the shaded regions represent the decay rate associated with an out-of-plane quality factor of 10^6 and 10^7, respectively. (a) Resulting decay rates from the simulated system in the previous section showing that absorption is too high to achieve critical coupling. (b) Configuration where d_0 and d_1 have been increased by $15\times$ to realize critical coupling without being overwhelmed by γ_L. (c) Configuration where the top and bottom waveguide have been configured to use the first and second order sideband and the modulating waveform gives $u^{(1)} = u^{(2)}$. In this configuration γ_0 and γ_1 are overlapping and critical coupling is always achieved.

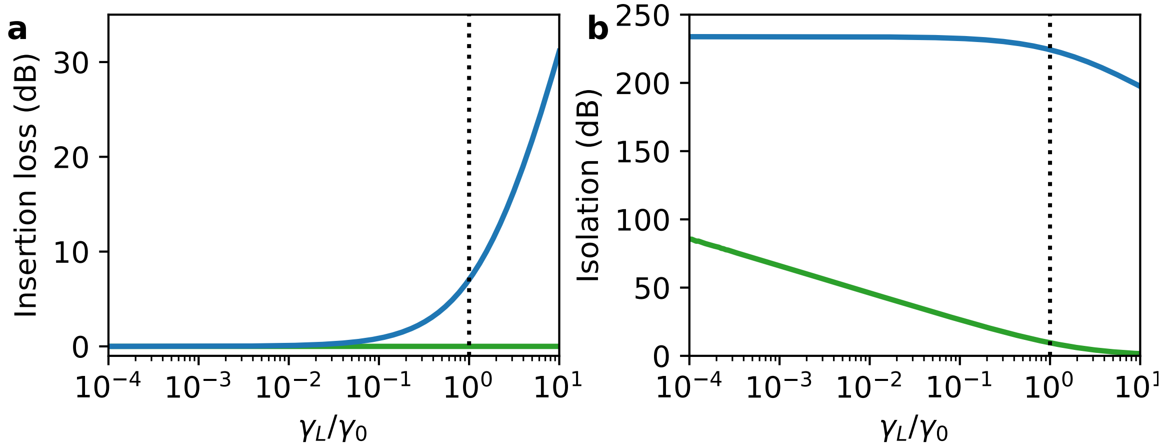

Figure 7.19: (a) Insertion loss and (b) isolation in the $\alpha_O \to \beta_O$ (blue) and $\beta_E \to \alpha_O$ (green) scattering pathways as a function of the resonator loss rate, normalized to the coupling rate to the bottom waveguide. The $\alpha_O \to \beta_O$ pathway experiences large insertion loss for higher γ_L but maintains large isolation. On the other hand, the $\beta_E \to \alpha_O$ pathway experiences reduced isolation for higher γ_L but no increased insertion loss.

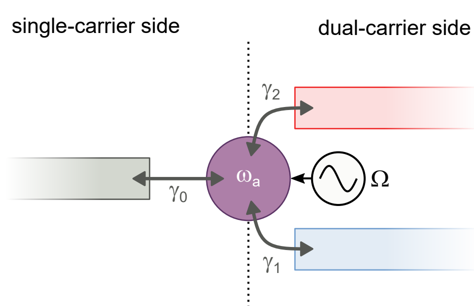

Figure 7.20: Schematic of a three-port optical circuit for generating the dual-carrier compound mode. A single-frequency signal incident from the left will be perfectly converted into the dual-carrier signal on the right if $\gamma_1 = \gamma_2 = \gamma_0/2$. The conversion process is reciprocal and the dual-carrier signal incident from the right will be perfectly converted into the single-frequency wave on the left.

[152], the signal spectral properties and overall spectral response are fundamentally different. The signal wave is carried by the dual-carrier wave, and its spectral distribution is conserved during transit across the Floquet circulator (i.e. no net energy transfer occurs between different sideband carriers). This lack of frequency-shifted intermediate signals simplifies the system design, which only needs to target a single frequency range, but also requires only two structural resonances (as opposed to four resonances with parametric conversion), resulting a smaller footprint. More importantly, without depending on large parametric conversion, the Floquet circulators can function at a modulation index that is orders of magnitude smaller than the typical values needed in parametric conversion [150], [152], making it more practical for implementation at optical frequencies. Moreover, the lack of net parametric energy conversion also prevents the depletion of the modulation wave in cases involving high-power signals. The absence of depletion ensures the system response remains linear to the input power, which is essential for high-dynamic range applications [184] such as full-duplex radios [119].

The spectral response of the Floquet circulator is quite different than those that break the degeneracy of counter-propagating traveling modes (Fig. 7.21a), that induce effective rotation in resonant waveguide junctions (Fig. 7.21b), or that induce an directionally dependent transparency window (Fig. 7.21c). Additionally, many possible layouts of low-symmetry one-dimensional cascades of modulated resonators can be used to implement the Floquet circulator. The critical coupling condition and the $\Delta\theta = \pi/2$ phase shift, which collectively produce the ideal circulator response, are not tied to the structural rotational and mirror symmetries of the device. We emphasize that the designation of the compound modes as "even" and "odd" is adopted from the convention in dual-waveguide systems such as directional couplers, and does not require that the system actually have mirror symmetry along the vertical direction. In fact, in our system the resonators have different coupling distances to the two waveguides, which also do not support wave propagation in the same frequency range.

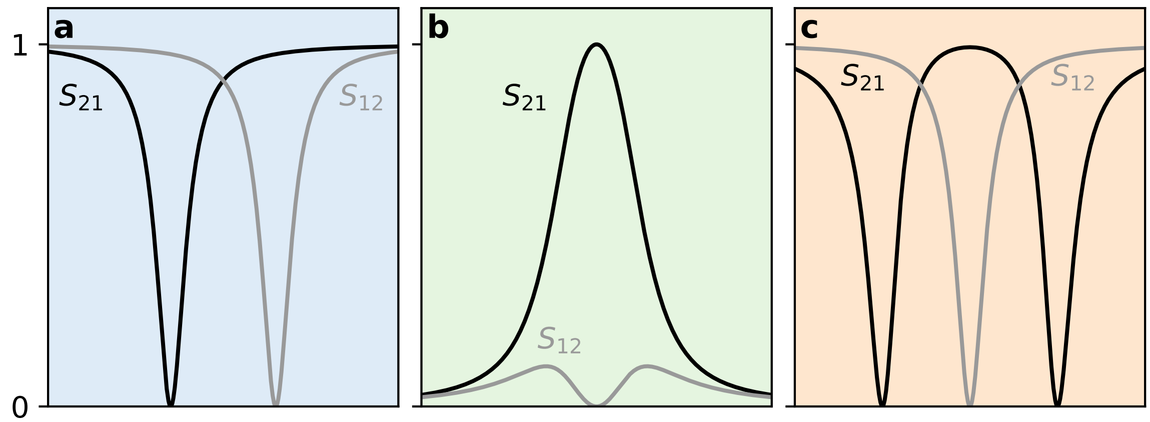

Figure 7.21: Sketch of forward $|S_{21}|^2$ and backward scattering $|S_{12}|^2$ spectra for several nonreciprocal systems. (a) Corresponds to a waveguide side-coupled to a traveling wave resonator with broken degeneracy in its two counter-propagating modes. The degeneracy can be broken either by evanescently coupling the resonator to a magneto-optical material of by applying modulation with an angular momentum. (b) Corresponds to the case of a three-port junction with broken rotational degeneracy. (c) Corresponds to the case of nonreciprocal optomechanically induced transparency.

7.5 Modulation Stability

Neglecting damping and waveguide coupling, the Floquet resonator is equivalent to a parametrically modulated harmonic oscillator described by the Mathieu differential equation [180], [181]. This is given in dimensionless form as

$$\frac{\delta^2 a}{\delta t^2} + [1 + \delta \cos(\Omega t)]\, a = 0, \tag{7.34}$$

where a is the oscillator amplitude, δ is the modulation index, and Ω is the modulation rate. This equation admits stable and unstable periodic solutions depending on the combination of modulation parameters. A map of the stability regions has been computed and is given in Figure 7.22 where the dark blue regions correspond to unstable solutions that occur due to parametric resonance when the system is driven at harmonics of the fundamental system resonance. In this work we limit consideration to relatively "weak" and "slow" modulation which corresponds to the region around the origin (bottom left) of Fig. 7.22.

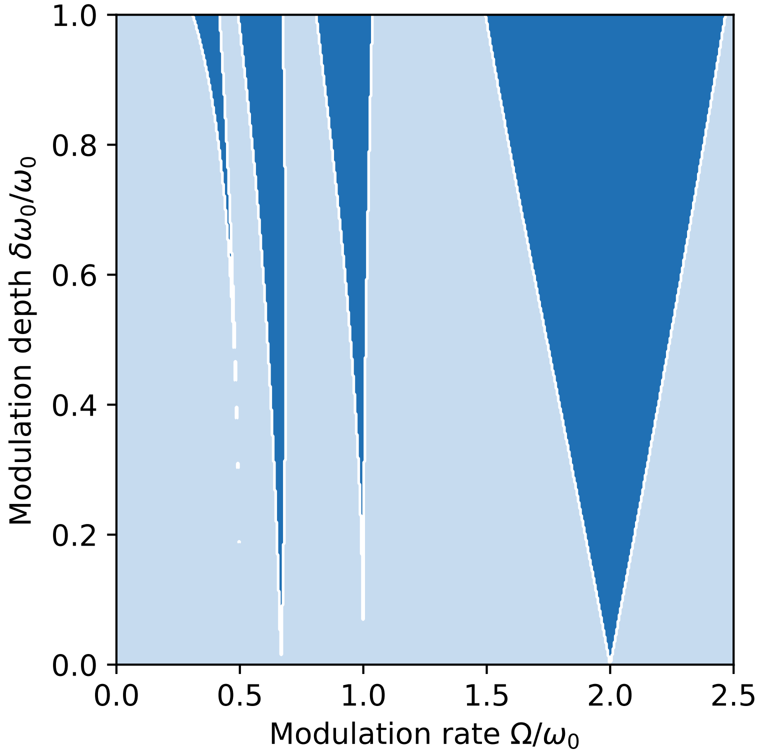

Figure 7.22: Modulated harmonic oscillator stability map. (light blue) Stable and (dark blue) unstable solutions as a function of modulation rate and modulation depth.

The instability regions occur at modulation frequencies that are harmonics of the *unmodulated* oscillator frequency ω_0, which is challenging to reach in optical systems due to the relatively slow underlying modulation mechanism.

Appendix A

Quadratic Eigenvalue Problem Parameter Sweeper (QEPPS)

This appendix documents the Quadratic Eigenvalue Parameter Sweeper (QEPPS) software package* which was developed as part of this dissertation. As its name suggests, the purpose of QEPPS is to perform parameter sweeps of quadratic eigenvalue problems on a Linux HPC cluster environment.

A.1 Background

Modal studies in electromagnetics and optics are quadratic eigenvalue problems. When discretized using the finite element method or some other approach, they have the form

$$\left(\lambda^2 \mathbf{E} + \lambda \mathbf{D} + \mathbf{K}\right) \mathbf{u} = 0 \tag{A.1}$$

where $\mathbf{E}$ is the mass matrix, $\mathbf{D}$ is the damping matrix, and $\mathbf{K}$ is the stiffness matrix. $\mathbf{u}$ is the eigenvector, and λ is the eigenvalue. Physically, $\mathbf{u}$ corresponds to the electric or magnetic field distribution over the discretized domain depending on how the problem was formulated. Each vector element corresponds to the field components at a location within the mesh of the original problem. The eigenvalue λ can represent either a spatial frequency (such as the wave vector of a waveguide mode) or a temporal frequency.

In electromagnetic problems, one is often interested in sweeping frequency to analyze the dispersion of one or more modes. This is useful for many situations, including photonic band gap engineering and for characterizing the attenuation of a transmission line.

A.2 Approach

QEPPS was developed with the intention of solving problems that have been exported from COMSOL Multiphysics using the MATLAB API for accessing the

*The source code for QEPPS is available at `https://github.com/ianwilliamson/qepps`.

linear algebra data structures. In this discussion we assume that COMSOL is being used to define the problem but this approach could apply elsewhere.

To illustrate the class of use cases for QEPPS, consider the scenario of solving for the guided wave vector of a structure as a function of the temporal frequency. This means that $\lambda = k$ in Eqn. A.1 and $\lambda(\omega)$ where ω is the temporal frequency. QEPPS provides an interface for specifying an arbitrary number of sub-matrices (Fig. A.1), each with its own arbitrary scaling function of ω, that are used to combine the sub-matrices into the problem matrices $\mathbf{E}$, $\mathbf{D}$, and $\mathbf{K}$. This means that rather than having assembling a set of problem matrices $[\mathbf{E}, \mathbf{D}, \mathbf{K}]$ for every $\omega = [\omega_1, \omega_2, \omega_3, \ldots]$ and uploading to a cluster, the problem can be specified in the form

$$\mathbf{E} = \mathbf{E}_0 + \omega \mathbf{E}_1 + \omega^2 \mathbf{E}_2 \tag{A.2}$$

$$\mathbf{D} = \mathbf{D}_0 + \omega \mathbf{D}_1 + \omega^2 \mathbf{D}_2 \tag{A.3}$$

$$\mathbf{K} = \mathbf{K}_0 + \omega \mathbf{K}_1 + \omega^2 \mathbf{K}_3, \tag{A.4}$$

where a single set of sub-matrices $\mathbf{E}_n$, $\mathbf{D}_n$, and $\mathbf{K}_n$ are extracted from COMSOL by modifying the underlying weak form equations.

The interface provided by QEPPS for specifying the scaling functions is implemented using a LUA interpreter with support for complex numbers. This is general, and it is emphasized that more complex functions of ω can also be specified (beyond the polynomials of 1, ω, and ω^2 shown above). For example, the dispersive surface conductivity of graphene could be added to the problem though the inclusion of an appropriate sub-matrix. The parameter sweeping functionality can also be applied to parameters other than ω, so long as they do not modify the underlying mesh of the problem.

A.3 Building

QEPPS was developed using the Texas Advanced Computing Center (TACC) resources. Accordingly, most of the dependencies can be satisfied by loading the prepackaged TACC modules. The full list of dependencies is:

- PETSc 3.5 (complex)

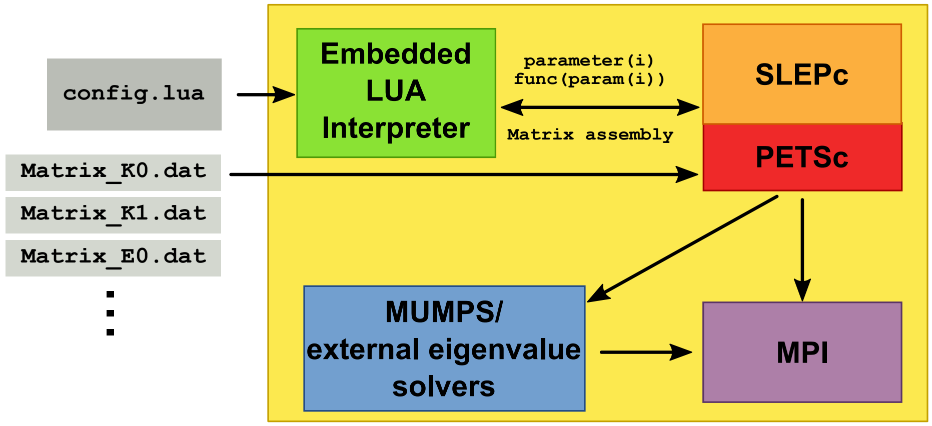

Figure A.1: Block diagram of QEPPS.

- SLEPc 3.5 (complex)
- MUMPS 4.10 (complex)
- libgrvy 0.32
- LUA 5.2

The appropriate versions of PETSC, SLEPc, MUMPS, and libgrvy can all be added to the user env on at TACC with the following command

```
module load \
   petsc/3.5-complex \
   slepc/3.5-complex \
   mumps/4.10.0-complex \
   grvy/0.32.0
```

LUA 5.2 is included in the source of QEPPS under src/lua and the QEPPS makefile is already configured to build and link against LUA in this location. After the dependencies have been satisfied, all that is needed to build QEPPS is the command

```
make
```

A.4 Test Problems

The configuration LUA scripts and data files for several test problems are provided under the tests/ subdirectory. These can be run in their current form, without modification on a single TACC stampede dev node. Launcher bash scripts are also included for running each problem. Currently two problems are provided and both are relatively small; the entire parameter sweep for each should complete in less than a minute. These can be used to validate the results that are obtained after modifying QEPPS or trying different solver options.

A.5 Usage and Output

As demonstrated by the provided test problems, a LUA script file along with command line arguments to the PETSc options database control all runtime configuration of QEPPS. This approach affords the user maximal flexibility in modifying the parameter sweep values and changing the problem configuration.

The scaling functions are specified in the LUA configuration script and their evaluation is handled at run time by the embedded LUA engine. The locations of the data files are also specified in the LUA script. Additionally, various options for controling QEPPS behavior are also specified in the LUA script. Please see the example problems under the tests/ subdirectory for detailed explanations and examples.

A.5.1 Eigenvalues

The eigenvalues are printed to an output file as well as to stdout in a CSV (comma separated value) format along row-by-row for each parameter sweep value. This allows the output file to be easily parsed by the plotting utility provided under tools/. Additional problem information is also printed; these lines are prefixed with a #.

A.5.2 Eigenvectors

There is a flag in the input configuration that specifies whether QEPPS should save the solution vectors for each parameter sweep value. For more information see the test problem configuration files.

Appendix B
Coupled Mode Theory

In this appendix we derive the coupled mode theory for several basic optical systems. These are based on the author's personal notes and are provided here for reference to the interested reader and for comparison with the coupled mode theory derivation used to model the Floquet circulator in Chapter 7.

B.1 Assumptions

The concept of modes is fundamental to electromagnetics, optics, and many other areas of physics. Optical modes are generally categorized as being either propagating or non-propagating, i.e. in a waveguide or localized in a resonator cavity. The scattering response of many optical systems, so long as they have a well-defined set of pathways for waves to enter and exit the system, can be described by temporal coupled mode theory (CMT). The approach taken in this appendix follows that of Herman Haus in his textbook [105].

Note that we assume all phasor quantities have $e^{j\omega t}$ time-dependence.

B.2 Two-Port System

The simplest and most common cases of two-port coupled optical systems are an optical resonator side-coupled to a waveguide (Fig. B.1a) and end-coupled to two waveguides (Fig. B.1b). However, we will first consider a generic two-port system and revisit these two specific cases after some more fundamental relationships have been derived. For now, we neglect any intrinsic absorption or radiation loss in the resonator. The governing equation that describes the time variation of the resonator amplitude, a is

$$\frac{da}{dt} = (j\omega_0 - \gamma)\, a + \begin{pmatrix} \kappa_1 & \kappa_2 \end{pmatrix} \begin{pmatrix} s_{1+} \\ s_{2+} \end{pmatrix}, \tag{B.1}$$

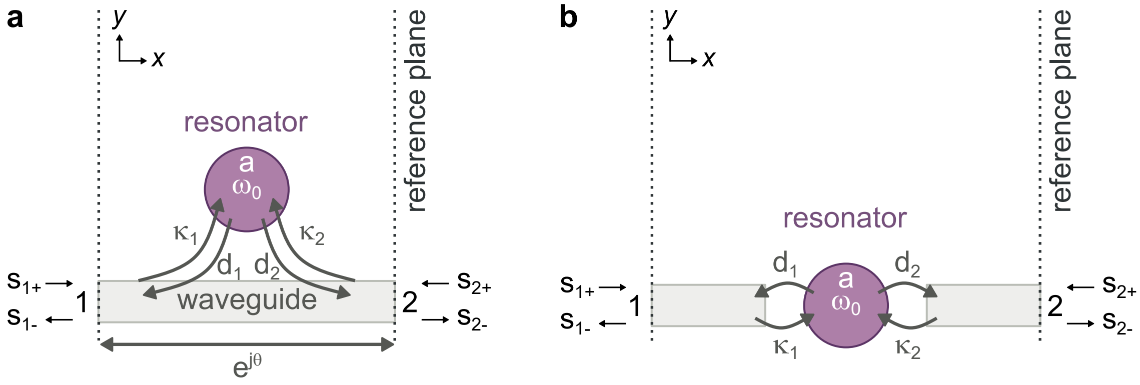

Figure B.1: (a) Schematic of a generic resonator *side-coupled* to a waveguide. (b) Schematic of a generic resonator *end-coupled* to two waveguides. Both systems have two ports and the quantity a represents the complex amplitude of the resonator mode with frequency ω_0. The energy stored in the mode is given by $|a|^2$. The complex constants κ_n and d_n represent the strength of coupling from the n-th port to the resonance and vice-versa, respectively. In the side-coupled system of (a), θ represents the phase delay of a wave traveling between the ports in the waveguide.

while the governing equation for the outgoing waves, $s_{1(2)-}$ is

$$\begin{pmatrix} s_{1-} \\ s_{2-} \end{pmatrix} = \begin{pmatrix} r & t \\ t & r \end{pmatrix} \begin{pmatrix} s_{1+} \\ s_{2+} \end{pmatrix} + a \begin{pmatrix} d_1 \\ d_2 \end{pmatrix}. \tag{B.2}$$

Note that we are representing coupling *into* the resonator with the coefficient κ_n and coupling *out* of the resonator with the coefficient d_n. It will be shown later that energy conservation forces these coefficients to be equivalent. In Eqns. B.1 and B.2, a represents the resonator complex mode amplitude; ω_0 represents the angular resonance frequency; γ represents the decay rate of the resonator. Note that γ is a half-width half-max quantity and the full-width half-max of the dip in the transmission and reflection spectra is given by the quantity 2γ.

B.2.1 Energy Conservation

Through energy conservation the number of unknowns in Eqns. B.1 and B.2 can be reduced. First we assume no excitation (with $s_{1+} = s_{2+} = 0$) and we allow the resonator to decay into the output ports. This gives us the two expressions

$$\frac{d\,|a|^2}{dt} = -2\gamma\,|a|^2 \tag{B.3}$$

$$\frac{d\,|a|^2}{dt} = -\,|s_{1-}|^2 - |s_{2-}|^2 = -\left(|d_1|^2 + |d_2|^2\right)|a|^2, \tag{B.4}$$

from which we conclude that

$$\gamma = \frac{1}{2}\left(|d_1|^2 + |d_2|^2\right). \tag{B.5}$$

B.2.2 Time-Reversal Symmetry

The resonator amplitude has the time dependence $a \sim a_0 e^{(j\omega_0-\gamma)t}$, which leads to the outgoing waves decaying exponentially with the same time dependence, $s_{1-} \sim s'_{1-}e^{(j\omega_0-\gamma)t}$ and $s_{2-} \sim s'_{2-}, e^{(j\omega_0-\gamma)t}$ where $s'_{1-} = d_1a_0$ and $s'_{2-} = d_2a_0$. Next we consider the scenario where the resonator is coherently pumped by turning the outgoing waves into incoming waves. We let $\widetilde{s}_{1+} = (s_{1-}|_{t\to -t})^*$ and $\widetilde{s}_{2+} = (s_{2-}|_{t\to -t})^*$ where $(\cdot)^*$ denotes the complex conjugate. $\widetilde{a}$ denotes the time reversed, exponentially growing resonator amplitude. Plugging these into Eqn. B.1 gives

$$\frac{d\widetilde{a}}{dt} = a_0^*\left(j\omega_0 + \gamma\right) = a_0^*\left(j\omega_0 - \gamma\right) + \begin{pmatrix}\kappa_1 & \kappa_2\end{pmatrix}\begin{pmatrix}\widetilde{s}_{1+} \\ \widetilde{s}_{2+}\end{pmatrix}. \tag{B.6}$$

Therefore,

$$\begin{aligned} a_0^* 2\gamma &= \kappa_1\left(d_1a_0\right)^* + \kappa_2\left(d_2a_0\right)^* \\ 2\gamma &= \kappa_1 d_1^* + \kappa_2 d_2^*. \end{aligned} \tag{B.7}$$

The above result, when combined with the conclusion from energy conservation means that

$$\kappa_1 = d_1 \tag{B.8}$$

$$\kappa_2 = d_2. \tag{B.9}$$

Finally, when the system is coherently driven through the input ports, there are no outgoing waves. This translates to the following relationship

$$
\begin{aligned}
\begin{pmatrix} 0 \\ 0 \end{pmatrix} &= \begin{pmatrix} r & t \\ t & r \end{pmatrix} \begin{pmatrix} \widetilde{s}_{1+} \\ \widetilde{s}_{2+} \end{pmatrix} + \widetilde{a} \begin{pmatrix} d_1 \\ d_2 \end{pmatrix} \\
\begin{pmatrix} d_1 \\ d_2 \end{pmatrix} &= - \begin{pmatrix} r & t \\ t & r \end{pmatrix} \begin{pmatrix} d_1^* \\ d_2^* \end{pmatrix},
\end{aligned} \tag{B.10}
$$

where the second line implies that the direct pathway through the system (the waveguide) imposes conditions on the resonant pathway. The complete scattering matrix for this system is

$$
S = \begin{pmatrix} r & t \\ t & r \end{pmatrix} + \frac{1}{j\left(\omega - \omega_0\right) + \gamma} \begin{pmatrix} d_1 d_1 & d_1 d_2 \\ d_2 d_1 & d_2 d_2 \end{pmatrix}. \tag{B.11}
$$

Regarding the expression in Eqn. B.5, a common convention is to allow the decay rate to be represented as

$$
\gamma = \gamma_1 + \gamma_2, \tag{B.12}
$$

where γ_1 and γ_2 represent the decay rates into the waveguide connected to port 1 and port 2, respectively. Under this convention the magnitude of the coupling coefficients are given by

$$
|d_1| = \sqrt{2\gamma_1} \tag{B.13}
$$

$$
|d_2| = \sqrt{2\gamma_2}. \tag{B.14}
$$

The phase of d_1 and d_2 are always given by Eqn. B.10.

B.2.3 Resonator Absorption and Radiation Losses

Accounting for absorption and radiation loss in the resonator is straightforward. This actually does not change the derivation in the previous section and an additional contribution to the decay rate can be added. This modification changes

Eqn. B.1 into

$$\frac{da}{dt} = (j\omega_0 - \gamma_1 - \gamma_2 - \gamma_a)\, a + \begin{pmatrix} d_1 & d_2 \end{pmatrix} \begin{pmatrix} s_{1+} \\ s_{2+} \end{pmatrix}. \tag{B.15}$$

Similarly, the expression in Eqn. B.11 for the total scattering matrix is

$$S = \begin{pmatrix} r & t \\ t & r \end{pmatrix} + \frac{1}{j\,(\omega - \omega_0) + \gamma_1 + \gamma_2 + \gamma_a} \begin{pmatrix} d_1 d_1 & d_1 d_2 \\ d_2 d_1 & d_2 d_2 \end{pmatrix}. \tag{B.16}$$

B.2.4 Example: Side-Coupled Resonator

In a side-coupled configuration, such as the one considered so far and shown in Fig. B.1, $r = 0$ and $t = 1$. Therefore,

$$d_1 = -d_1^* \tag{B.17}$$

$$d_2 = -d_2^* \tag{B.18}$$

which implies that both d_1 and d_2 are purely imaginary. Additionally, if the resonator decays symmetrically into the two ports, we have:

$$\gamma_1 = \gamma_2 = \gamma_e/2 \tag{B.19}$$

$$d_1 = d_2 = j\sqrt{\gamma_e} \tag{B.20}$$

The complete frequency-dependent scattering parameters for this system (with absorption) are:

$$S_{11}(\omega) = -\frac{\gamma_e}{j(\omega - \omega_0) + \gamma_e + \gamma_a} \tag{B.21}$$

$$S_{21}(\omega) = \frac{j(\omega - \omega_0) + \gamma_a}{j(\omega - \omega_0) + \gamma_e + \gamma_a} \tag{B.22}$$

B.2.5 Example: End-Coupled Resonator

In an end-coupled configuration, $r = 1$ and $t = 0$. Therefore,

$$d_1 = -d_2^* \tag{B.23}$$

$$d_2 = -d_1^* \tag{B.24}$$

which implies that both d_1 and d_2 are purely imaginary. Additionally, if the resonator decays symmetrically into the two ports, we have:

$$\gamma_1 = \gamma_2 = \gamma_e/2 \tag{B.25}$$

$$d_1 = d_2 = j\sqrt{\gamma_e} \tag{B.26}$$

The complete frequency-dependent scattering parameters for this system (with absorption) are:

$$S_{11}(\omega) = -\frac{\gamma_e}{j(\omega - \omega_0) + \gamma_e + \gamma_a} \tag{B.27}$$

$$S_{21}(\omega) = \frac{j(\omega - \omega_0) + \gamma_a}{j(\omega - \omega_0) + \gamma_e + \gamma_a} \tag{B.28}$$

B.2.6 Example: One-Port System

In a one port single resonance system, the governing equations are given by

$$\frac{da}{dt} = (j\omega_0 - \gamma_1 - \gamma_a)a + d_1 s_{1+}, \tag{B.29}$$

and

$$s_{1-} = r s_{1+} + a d_1. \tag{B.30}$$

Combining these equations and using the previously developed conditions on the parameters gives the following expression for total system's reflection coefficient:

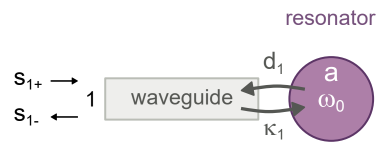

Figure B.2: Schematic of the one port coupled resonator system.

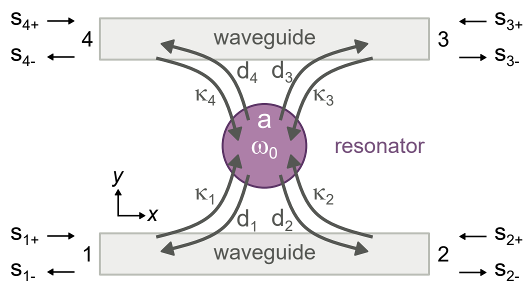

Figure B.3: Schematic of a general waveguide-resonator-waveguide structure.

$$S_{11} = r + \frac{2\gamma_1}{j(\omega - \omega_0) + \gamma_1 + \gamma_a} \tag{B.31}$$

$$= \frac{2\gamma_1 - j(\omega - \omega_0) - \gamma_1 - \gamma_a}{j(\omega - \omega_0) + \gamma_1 + \gamma_a} \tag{B.32}$$

$$= \frac{-j(\omega - \omega_0) + \gamma_1 - \gamma_a}{j(\omega - \omega_0) + \gamma_1 + \gamma_a} \tag{B.33}$$

B.3 Four-Port System

We consider the four port system shown in Fig. B.3 where a resonator is simultaneously side-coupled to two waveguides (commonly used as a channel add and drop filter).

The coupled mode equations for the system shown in Fig. B.3 are,

$$\frac{da}{dt} = (j\omega_0 - \gamma_1 - \gamma_2 - \gamma_3 - \gamma_4 - \gamma_a)a + \begin{pmatrix} d_1 & d_2 & d_3 & d_4 \end{pmatrix} \begin{pmatrix} s_{1+} \\ s_{2+} \\ s_{3+} \\ s_{4+} \end{pmatrix} \tag{B.34}$$

$$\begin{pmatrix} s_{1-} \\ s_{2-} \\ s_{3-} \\ s_{4-} \end{pmatrix} = \begin{pmatrix} 0 & e^{-j\phi_1} & 0 & 0 \\ e^{-j\phi_1} & 0 & 0 & 0 \\ 0 & 0 & 0 & e^{-j\phi_2} \\ 0 & 0 & e^{-j\phi_2} & 0 \end{pmatrix} \begin{pmatrix} s_{1+} \\ s_{2+} \\ s_{3+} \\ s_{4+} \end{pmatrix} + \begin{pmatrix} d_1 \\ d_2 \\ d_3 \\ d_4 \end{pmatrix} a \tag{B.35}$$

Similarly to the two-port system, energy conservation and time-reversal symmetry provide the conditions

$$d_1 = -e^{-j\phi_1} d_2^* \tag{B.36}$$
$$d_2 = -e^{-j\phi_1} d_1^* \tag{B.37}$$
$$d_3 = -e^{-j\phi_2} d_4^* \tag{B.38}$$
$$d_4 = -e^{-j\phi_2} d_3^* \tag{B.39}$$

$$|d_1| = \sqrt{2\gamma_1} \tag{B.40}$$
$$|d_2| = \sqrt{2\gamma_2} \tag{B.41}$$
$$|d_3| = \sqrt{2\gamma_3} \tag{B.42}$$
$$|d_4| = \sqrt{2\gamma_4}. \tag{B.43}$$

Combining Eqns. B.34 and B.35, we have the following as the complete scattering matrix of the system,

$$\mathbf{S} = \begin{pmatrix} 0 & e^{-j\phi_1} & 0 & 0 \\ e^{-j\phi_1} & 0 & 0 & 0 \\ 0 & 0 & 0 & e^{-j\phi_2} \\ 0 & 0 & e^{-j\phi_2} & 0 \end{pmatrix} + \frac{1}{j(\omega - \omega_0) + \gamma} \begin{pmatrix} d_1 d_1 & d_1 d_2 & d_1 d_3 & d_1 d_4 \\ d_2 d_1 & d_2 d_2 & d_2 d_3 & d_2 d_4 \\ d_3 d_1 & d_3 d_2 & d_3 d_3 & d_3 d_4 \\ d_4 d_1 & d_4 d_2 & d_4 d_3 & d_4 d_4 \end{pmatrix} \tag{B.44}$$

where $\gamma = \gamma_1 + \gamma_2 + \gamma_3 + \gamma_4 + \gamma_a$.

If the resonator is a standing wave cavity with even symmetry in the vertical and horizontal directions, it decays with equal magnitude and sign into all ports, $|d_1| = |d_2|$, $|d_3| = |d_4|$, $\gamma_1 = \gamma_2$, and $\gamma_3 = \gamma_4$. Additionally, the conditions given by Eqns. B.34 and B.35, imply that the coupling coefficients satisfy

$$\begin{aligned} d_1 &= j\sqrt{2\gamma_0} \\ d_2 &= j\sqrt{2\gamma_0} \\ d_3 &= j\sqrt{2\gamma_1} \\ d_4 &= j\sqrt{2\gamma_1} \end{aligned}$$

if we allow ϕ_1 and ϕ_2 to be some even multiple of 2π through a suitable choice of the port reference planes.

If we consider excitation from only port 1, the scattering parameters are

$$S_{11} = \frac{-\gamma_0}{j(\omega - \omega_0) + \gamma_0 + \gamma_1 + \gamma_a} \tag{B.45}$$

$$S_{21} = 1 + \frac{-\gamma_0}{j(\omega - \omega_0) + \gamma_0 + \gamma_1 + \gamma_a} \tag{B.46}$$

$$S_{31} = \frac{-\sqrt{\gamma_0\gamma_1}}{j(\omega - \omega_0) + \gamma_0 + \gamma_1 + \gamma_a} \tag{B.47}$$

$$S_{41} = \frac{-\sqrt{\gamma_0\gamma_1}}{j(\omega - \omega_0) + \gamma_0 + \gamma_1 + \gamma_a} \tag{B.48}$$

The above results agree with Eqns. 10-13 of [171] with $\theta_1 = \theta_2 = \theta_3 = \theta_4 = \pi/2$.

Appendix C

Frequency-Domain Numerical Modeling of Time-Driven and Nonlinear Systems

C.1 Coupling Terms in Time-Driven Systems

In this appendix we outline the approach for modeling periodically time-modulated optical systems in the frequency domain. We use a set of single-frequency wave equations which are coupled in the regions that are undergoing modulation. To derive the coupling terms, we start with the general wave equation for the electric field given by

$$\nabla \times \nabla \times \mathbf{E} + \frac{1}{c^2}\frac{\delta^2}{\delta t^2}\mathbf{E} + \frac{1}{\epsilon_0 c^2}\frac{\delta^2}{\delta t^2}\mathbf{P} = 0, \tag{C.1}$$

where $\mathbf{E}$ is the total electric field, $\mathbf{P}$ is the total electric polarizability (accounting for both static and modulated terms), ϵ_0 is the vacuum permittivity, and c is the speed of light in vacuum. The refractive index in the modulated region has the form $n'_0 = n_0 + \Delta n_0(t)$ where we assume that the time-varying component is purely sinusoidal,

$$\Delta n_0(t) = \delta n_0 \cos(\Omega t + \phi) = \frac{\delta n_0}{2}\left[e^{j\Omega t}e^{j\phi} + e^{-j\Omega t}e^{-j\phi}\right]. \tag{C.2}$$

Eqn. C.2 is substituted into Eqn. C.1. The wave equation is then rearranged into "static" and "modulated" terms (where $\Delta n_0{}^2 \ll n_0$) to give [105],

$$\nabla \times \nabla \times \mathbf{E} + \frac{n_0{}^2}{c^2}\frac{\delta^2}{\delta t^2}\mathbf{E} + \frac{1}{c^2}\frac{\delta^2}{\delta t^2}\left[2n_0\Delta n_0(t)\cdot\mathbf{E}\right] = 0. \tag{C.3}$$

By representing the total electric field as a sum of components oscillating at discrete frequencies indexed by n,

$$\mathbf{E} = \sum_n \mathbf{E}_n e^{j\omega_n t} \tag{C.4}$$

and substituting into Eqn. C.3, we have

$$\nabla \times \nabla \times \mathbf{E}_n e^{j\omega_n t} + \frac{{n_0}^2}{c^2}\frac{\delta^2}{\delta t^2}\mathbf{E}_n e^{j\omega_n t} + \frac{\delta n_0 n_0}{c^2}\frac{\delta^2}{\delta t^2}\left[\left(e^{j\Omega t}e^{j\phi} + e^{-j\Omega t}e^{-j\phi}\right)\mathbf{E}_n e^{j\omega_n t}\right] = 0 \quad \text{(C.5)}$$

$$\nabla \times \nabla \times \mathbf{E}_n e^{j\omega_n t} - \frac{{\omega_n}^2 {n_0}^2}{c^2}\mathbf{E}_n e^{j\omega_n t} - \frac{\delta n_0 n_0}{c^2}\left[(\omega_n + \Omega)^2 e^{j(\omega_{n+1}t+\phi)} + (\omega_n - \Omega)^2 e^{j(\omega_{n-1}t-\phi)}\right]\mathbf{E}_n = 0. \quad \text{(C.6)}$$

The expression in Eqn. C.6 is an ordinary single-frequency wave equation with an added "nearest neighbor coupling" term. Essentially, the wave at frequency ω_n feeds energy to the waves at frequencies $\omega_n \pm \Omega$ via a current distribution proportional to $\mathbf{E}_n$. The coupling term is,

$$g(n, m) = -\frac{\delta n_0 n_0}{c^2}{\omega_n}^2 e^{j\phi(n-m)}\delta(|n-m|-1)\,\mathbf{E}_m, \quad \text{(C.7)}$$

where the $(n-m)$ term in the exponential enforces a negative phase accumulation from a higher-order frequency component to a lower-order frequency component, and a positive phase accumulation from a lower-order frequency component to a higher-order frequency component. The Dirac delta, $\delta(|n-m|-1)$ enforces the condition of the entire term being non-zero only when n and m differ by 1. This means that with a single-frequency sinusoidal modulation waveform, each sideband component has only two source terms, corresponding to the nearest neighbor frequency components, i.e. $n = 0 : g(0, -1)$ and $g(0, 1)$.

This coupling can be implemented in finite element analysis by converting to a weak form expression. In this case, the weak form corresponds to a simple multiplication by the test function corresponding to the unknown electric field, e.g. Ψ_n. The following expression can added as a weak contribution in the modulated domain(s) for each frequency component,

$$F_n = g(n, n+1)\cdot\Psi_n + g(n, n-1)\cdot\Psi_n. \quad \text{(C.8)}$$

C.1.1 Implementation in COMSOL Multiphysics

Converting the source coupling term in Eqn. C.8 to a form that can be input into COMSOL Multiphysics is straight forward. Shown below is an example that applies to the TM polarization in a two-dimensional simulation ($\mathbf{E}_z$ electric field component only) with *three* frequency components (one carrier and two sidebands).

```
g12     -n*dn/c_const^2*4*pi^2*(freq0+freqM)^2*E2z*exp(-1j*phi)
g21     -n*dn/c_const^2*4*pi^2*(freq0)^2*E1z*exp(1j*phi)
g23     -n*dn/c_const^2*4*pi^2*(freq0)^2*E3z*exp(-1j*phi)
g32     -n*dn/c_const^2*4*pi^2*(freq0-freqM)^2*E2z*exp(1j*phi)
weak1   test(E1z)*g12
weak2   test(E2z)*(g23+g21)
weak3   test(E3z)*g32
```

The parameter `freq0` is the carrier frequency, `freqM` is the modulation frequency, `phi` is the modulation phase, `n` is the refractive index of the material, and `dn` is the relative change in the refractive index due to modulation. `E1z`, `E2z`, and `E3z` are the unknown electric field components of the lower sideband $(\omega - \Omega)$, the carrier (ω), and the upper sideband $(\omega + \Omega)$. The expressions `weak1`, `weak2`, and `weak3` can be added as *domain* weak contributions to the modulated region(s).

C.2 Coupling Terms in Nonlinear Wave-Mixing

The same approach used in the previous section can also be applied to the interaction of waves in nonlinear media. In this case however the number of frequency components is more limited as an infinite set of sidebands does not need to be considered. To derive the coupling terms, we begin with the nonlinear wave equation given by

$$\nabla \times \left(\frac{1}{\mu_r} \nabla \times \mathbf{E} \right) - k_0 \left(\epsilon_r - \frac{j\sigma}{\omega\epsilon_0} \right) \mathbf{E} = -\mu_0 j\omega \mathbf{J} + \mu_0 \frac{d^2 \mathbf{P}_{NL}}{dt^2}. \tag{C.9}$$

where

$$\mathbf{E} = \sum_{n=\pm1,\pm2,\pm3} \frac{1}{2} \mathbf{E}_n e^{j\omega_n t} \tag{C.10}$$

and $\mathbf{E}_{-n} = \mathbf{E}_n^*$ and $\omega_{-n} = -\omega_n$. The nonlinear polarization term is

$$\mathbf{P}_{NL} = 2d\mathbf{E}^2 \tag{C.11}$$

$$= \frac{1}{2}d \sum_{n,m=\pm 1,\pm 2,\pm 3} \mathbf{E}_n \mathbf{E}_m e^{j(\omega_n+\omega_m)t}, \tag{C.12}$$

which consists of thirty six different terms. We can define a set of coupled linear wave equations given by

$$\nabla \times \left(\frac{1}{\mu_r}\nabla \times \mathbf{E}_n\right) - k_0\left(\epsilon_r - \frac{j\sigma}{\omega_n \epsilon_0}\right)\mathbf{E}_n = -\mu_0 j\omega_n \mathbf{J}_n + \mathbf{S}_n \tag{C.13}$$

where n corresponds to the n-th wave, oscillating at a frequency ω_n and

$$\mathbf{S}_n = \frac{1}{2}\mu_0 d \sum_{n',m'=\pm 1,\pm 2,\pm 3} \left(\omega_{n'} + \omega_{m'}\right)^2 \mathbf{E}_{n'}\mathbf{E}_{m'} e^{j(\omega_{n'}+\omega_{m'})t} \delta\left(\omega_n - \omega_{n'} - \omega_{m'}\right) \tag{C.14}$$

represents the nonlinear source coupling term. The $\mathbf{S}_n$ term can be converted into an effective current density defined as

$$\mathbf{J}_n^{(NL)} = -\frac{1}{\mu_0 j\omega_n}\mathbf{S}_n. \tag{C.15}$$

C.2.1 $\chi^{(2)}$ Nonlinearity

For a $\chi^{(2)}$ process where $\omega_3 = \omega_1 + \omega_2$, the source terms are given by

$$\mathbf{S}_1 = 2\mu_0 \omega_1^2 d E_2^* E_3 \tag{C.16}$$

$$\mathbf{S}_2 = 2\mu_0 \omega_2^2 d E_1^* E_3 \tag{C.17}$$

$$\mathbf{S}_3 = 2\mu_0 \omega_3^2 d E_1 E_2 \tag{C.18}$$

which can be mapped into effective current densities given by

$$\mathbf{J}_1^{(NL)} = 2j\omega_1 d E_2^* E_3 \tag{C.19}$$

$$\mathbf{J}_2^{(NL)} = 2j\omega_2 d E_1^* E_3 \tag{C.20}$$

$$\mathbf{J}_3^{(NL)} = 2j\omega_3 d E_1 E_2. \tag{C.21}$$

C.3 Validation

The Manley-Rowe relations can be used to confirm that energy is conserved. We can say that at port n, $I_{\text{in},n}$ is the total *incoming* energy and $I_{\text{out},n}$ is the total *outgoing* energy. This means

$$I_{\text{in},n} = \sum_m \frac{|s_{n+}^m|^2}{\omega_m} \tag{C.22}$$

$$I_{\text{out},n} = \sum_m \frac{|s_{n-}^m|^2}{\omega_m} \tag{C.23}$$

where $s_{n+(-)}^m$ is the complex amplitude of the incoming (outgoing) wave at port n with frequency m. For energy conservation to hold, in a lossless system we have that

$$\sum_n I_{\text{in},n} = \sum_n I_{\text{out},n}. \tag{C.24}$$

In terms of our numerical model, a relative error for this relationship can be defined as

$$E_{\text{energy}} = \frac{|\sum_n I_{\text{in},n} - \sum_n I_{\text{out},n}|}{\sum_n I_{\text{in},n}}. \tag{C.25}$$

References

[1] I. A. D. Williamson, T.-A. N. Nguyen, and Z. Wang, "Suppression of the skin effect in radio frequency transmission lines via gridded conductor fibers," *Applied Physics Letters*, vol. 108, no. 8, p. 083 502, Feb. 22, 2016.

[2] S. H. Mousavi, I. A. D. Williamson, and Z. Wang, "Kinetic inductance driven nanoscale 2D and 3D THz transmission lines," *Scientific Reports*, vol. 6, p. 25 303, May 3, 2016.

[3] I. A. D. Williamson, S. H. Mousavi, and Z. Wang, "Extraordinary wavelength reduction in terahertz graphene-cladded photonic crystal slabs," *Scientific Reports*, vol. 6, p. 25 301, May 4, 2016.

[4] ——, "Large Cavity-Optomechanical Coupling with Graphene at Infrared and Terahertz Frequencies," *ACS Photonics*, vol. 3, no. 12, pp. 2353–2361, Dec. 21, 2016.

[5] A. Deutsch, "Electrical characteristics of interconnections for high-performance systems," *Proceedings of the IEEE*, vol. 86, no. 2, pp. 315–357, 1998.

[6] J. Yao, "Photonics to the Rescue: A Fresh Look at Microwave Photonic Filters," *IEEE Microwave Magazine*, vol. 16, no. 8, pp. 46–60, Sep. 2015.

[7] J. Capmany, B. Ortega, and D. Pastor, "A tutorial on microwave photonic filters," *Journal of Lightwave Technology*, vol. 24, no. 1, pp. 201–229, Jan. 2006.

[8] D. A. B. Miller and H. M. Ozaktas, "Limit to the bit-rate capacity of electrical interconnects from the aspect ratio of the system architecture," *Journal of parallel and distributed computing*, vol. 41, no. 1, pp. 42–52, 1997.

[9] C. Svensson and G. H. Dermer, "Time domain modeling of lossy interconnects," *IEEE Transactions on Advanced Packaging*, vol. 24, no. 2, pp. 191–196, 2001.

[10] H. W. Johnson and M. Graham, *High Speed Signal Propagation: Advanced Black Magic*, ser. Prentice Hall Modern Semiconductor Design Series. Prentice Hall, Professional Technical Rreference, 2003.

[11] M. J. R. Heck, “Highly integrated optical phased arrays: Photonic integrated circuits for optical beam shaping and beam steering,” *Nanophotonics*, vol. 6, p. 152, Jan. 1, 2017.

[12] M. J. R. Heck, J. F. Bauters, M. L. Davenport, J. K. Doylend, S. Jain, G. Kurczveil, S. Srinivasan, Y. Tang, and J. E. Bowers, “Hybrid Silicon Photonic Integrated Circuit Technology,” *IEEE Journal of Selected Topics in Quantum Electronics*, vol. 19, no. 4, pp. 6 100 117–6 100 117, Jul. 2013.

[13] J. S. Bunch, A. M. van der Zande, S. S. Verbridge, I. W. Frank, D. M. Tanenbaum, J. M. Parpia, H. G. Craighead, and P. L. McEuen, “Electromechanical Resonators from Graphene Sheets,” *Science*, vol. 315, no. 5811, pp. 490–493, Jan. 26, 2007.

[14] J. S. Bunch, S. S. Verbridge, J. S. Alden, A. M. van der Zande, J. M. Parpia, H. G. Craighead, and P. L. McEuen, “Impermeable Atomic Membranes from Graphene Sheets,” *Nano Letters*, vol. 8, no. 8, pp. 2458–2462, Aug. 1, 2008.

[15] J. T. Robinson, M. Zalalutdinov, J. W. Baldwin, E. S. Snow, Z. Wei, P. Sheehan, and B. H. Houston, “Wafer-scale Reduced Graphene Oxide Films for Nanomechanical Devices,” *Nano Letters*, vol. 8, no. 10, pp. 3441–3445, Oct. 8, 2008.

[16] C. Chen, S. Rosenblatt, K. I. Bolotin, W. Kalb, P. Kim, I. Kymissis, H. L. Stormer, T. F. Heinz, and J. Hone, “Performance of monolayer graphene nanomechanical resonators with electrical readout,” *Nature Nanotechnology*, vol. 4, no. 12, pp. 861–867, Dec. 2009.

[17] S. Shivaraman, R. A. Barton, X. Yu, J. Alden, L. Herman, M. Chandrashekhar, J. Park, P. L. McEuen, J. M. Parpia, H. G. Craighead, and M. G. Spencer, “Free-Standing Epitaxial Graphene,” *Nano Letters*, vol. 9, no. 9, pp. 3100–3105, Sep. 9, 2009.

[18] V. Singh, S. Sengupta, H. S. Solanki, R. Dhall, A. Allain, S. Dhara, Prita Pant, and M. M. Deshmukh, “Probing thermal expansion of graphene and modal dispersion at low-temperature using graphene nanoelectromechanical systems resonators,” *Nanotechnology*, vol. 21, no. 16, p. 165 204, 2010.

[19] Y. Xu, C. Chen, V. V. Deshpande, F. A. DiRenno, A. Gondarenko, D. B. Heinz, S. Liu, P. Kim, and J. Hone, "Radio frequency electrical transduction of graphene mechanical resonators," *Applied Physics Letters*, vol. 97, no. 24, p. 243 111, Dec. 13, 2010.

[20] A. M. van der Zande, R. A. Barton, J. S. Alden, C. S. Ruiz-Vargas, W. S. Whitney, P. H. Q. Pham, J. Park, J. M. Parpia, H. G. Craighead, and P. L. McEuen, "Large-Scale Arrays of Single-Layer Graphene Resonators," *Nano Letters*, vol. 10, no. 12, pp. 4869–4873, Dec. 8, 2010.

[21] X. Song, M. Oksanen, M. A. Sillanpää, H. G. Craighead, J. M. Parpia, and P. J. Hakonen, "Stamp Transferred Suspended Graphene Mechanical Resonators for Radio Frequency Electrical Readout," *Nano Letters*, vol. 12, no. 1, pp. 198–202, Jan. 11, 2012.

[22] V. Singh, S. J. Bosman, B. H. Schneider, Y. M. Blanter, A. Castellanos-Gomez, and G. A. Steele, "Optomechanical coupling between a multilayer graphene mechanical resonator and a superconducting microwave cavity," *Nature Nanotechnology*, vol. 9, no. 10, pp. 820–824, Oct. 2014.

[23] X. Song, M. Oksanen, J. Li, P. J. Hakonen, and M. A. Sillanpää, "Graphene Optomechanics Realized at Microwave Frequencies," *Physical Review Letters*, vol. 113, no. 2, p. 027 404, Jul. 11, 2014.

[24] P. Weber, J. Güttinger, I. Tsioutsios, D. E. Chang, and A. Bachtold, "Coupling Graphene Mechanical Resonators to Superconducting Microwave Cavities," *Nano Letters*, vol. 14, no. 5, pp. 2854–2860, May 14, 2014.

[25] M. Poot and H. S. van der Zant, "Mechanical systems in the quantum regime," *Physics Reports*, vol. 511, no. 5, pp. 273–335, Feb. 2012.

[26] M. Wu, A. C. Hryciw, C. Healey, D. P. Lake, H. Jayakumar, M. R. Freeman, J. P. Davis, and P. E. Barclay, "Dissipative and Dispersive Optomechanics in a Nanocavity Torque Sensor," *Physical Review X*, vol. 4, no. 2, p. 021 052, Jun. 19, 2014.

[27] C. Reinhardt, T. Müller, A. Bourassa, and J. C. Sankey, "Ultralow-Noise SiN Trampoline Resonators for Sensing and Optomechanics," *Physical Review X*, vol. 6, no. 2, p. 021 001, Apr. 1, 2016.

[28] J. Gieseler, L. Novotny, and R. Quidant, "Thermal nonlinearities in a nanomechanical oscillator," *Nature Physics*, vol. 9, no. 12, pp. 806–810, Dec. 2013.

[29] C. A. Muschik, S. Moulieras, A. Bachtold, F. H. L. Koppens, M. Lewenstein, and D. E. Chang, "Harnessing Vacuum Forces for Quantum Sensing of Graphene Motion," *Physical Review Letters*, vol. 112, no. 22, p. 223 601, Jun. 3, 2014.

[30] A. Reserbat-Plantey, K. G. Schädler, L. Gaudreau, G. Navickaite, J. Güttinger, D. Chang, C. Toninelli, A. Bachtold, and F. H. L. Koppens, "Electromechanical control of nitrogen-vacancy defect emission using graphene NEMS," *Nature Communications*, vol. 7, p. 10 218, Jan. 8, 2016.

[31] R. M. Cole, G. A. Brawley, V. P. Adiga, R. De Alba, J. M. Parpia, B. Ilic, H. G. Craighead, and W. P. Bowen, "Evanescent-Field Optical Readout of Graphene Mechanical Motion at Room Temperature," *Physical Review Applied*, vol. 3, no. 2, p. 024 004, Feb. 17, 2015.

[32] C. R. Sullivan, "Litz-Wire Transformer Winding Optimal Choice for Number of Strands in a Litz-Wire Transformer Winding," *IEEE Transactions on Power Electronics*, vol. 14, no. 2, pp. 283–291, 1999.

[33] M. Kazimierczuk, *High-Frequency Magnetic Components*. Chichester, U.K: J. Wiley, 2009, 486 pp.

[34] A. Clogston, "Reduction of skin-effect losses by the use of laminated conductors," *Proceedings of the IRE*, 1951.

[35] Vaage, EF, "Transmission properties of laminated Clogston type conductors," *Bell System Technical Journal, The*, 1953.

[36] S. P. Morgan, "Mathematical theory of laminated transmission lines - Part I," *Bell System Technical Journal, The*, vol. 31, no. 5, pp. 883–949, Sep. 1952.

[37] ——, "Mathematical theory of laminated transmission lines - Part II," *Bell System Technical Journal, The*, vol. 31, no. 6, pp. 1121–1206, Nov. 1952.

[38] A. F. Abouraddy, M. Bayindir, G. Benoit, S. D. Hart, K. Kuriki, N. Orf, O. Shapira, F. Sorin, B. Temelkuran, and Y. Fink, "Towards multimaterial multifunctional fibres that see, hear, sense and communicate," *Nature Materials*, vol. 6, no. 5, pp. 336–347, May 2007.

[39] M. Fokine, L.-E. Nilsson, Å. Claesson, D. Berlemont, L. Kjellberg, L. Krummenacher, and W. Margulis, "Integrated fiber Mach-Zehnder interferometer for electro-optic switching," *Optics letters*, vol. 27, no. 18, pp. 1643–1645, 2002.

[40] A. Tuniz, K. J. Kaltenecker, B. M. Fischer, M. Walther, S. C. Fleming, A. Argyros, and B. T. Kuhlmey, "Metamaterial fibres for subdiffraction imaging and focusing at terahertz frequencies over optically long distances," *Nature Communications*, vol. 4, Oct. 28, 2013.

[41] M. Alexander Schmidt, A. Argyros, and F. Sorin, "Hybrid Optical Fibers - An Innovative Platform for In-Fiber Photonic Devices," *Advanced Optical Materials*, vol. 4, no. 1, pp. 13–36, Jan. 2016.

[42] D. M. Pozar, *Microwave Engineering*, 4th ed. Hoboken, NJ: Wiley, 2012, 732 pp.

[43] C. Hou, X. Jia, L. Wei, S.-C. Tan, X. Zhao, J. D. Joannopoulos, and Y. Fink, "Crystalline silicon core fibres from aluminium core preforms," *Nature Communications*, vol. 6, p. 6248, Feb. 20, 2015.

[44] D. Correas-Serrano, J. Gomez-Diaz, J. Perruisseau-Carrier, and A. Alvarez-Melcon, "Spatially Dispersive Graphene Single and Parallel Plate Waveguides: Analysis and Circuit Model," *IEEE Transactions on Microwave Theory and Techniques*, vol. 61, no. 12, pp. 4333–4344, Dec. 2013.

[45] R. Araneo, G. Lovat, and P. Burghignoli, "Dispersion analysis of graphene nanostrip lines," in *2012 IEEE Antennas and Propagation Society International Symposium*, 2012, pp. 1–2.

[46] S. Rakheja, V. Kumar, and A. Naeemi, "Evaluation of the Potential Performance of Graphene Nanoribbons as On-Chip Interconnects," *Proceedings of the IEEE*, vol. 101, no. 7, pp. 1740–1765, Jul. 2013.

[47] F. J. García de Abajo, "Graphene Plasmonics: Challenges and Opportunities," *ACS Photonics*, vol. 1, no. 3, pp. 135–152, Mar. 19, 2014.

[48] J. Christensen, A. Manjavacas, S. Thongrattanasiri, F. H. L. Koppens, and F. J. García de Abajo, "Graphene Plasmon Waveguiding and Hybridization in Individual and Paired Nanoribbons," *ACS Nano*, vol. 6, no. 1, pp. 431–440, Jan. 24, 2012.

[49] D. N. Basov, M. M. Fogler, A. Lanzara, F. Wang, and Y. Zhang, "Colloquium: Graphene spectroscopy," *Reviews of Modern Physics*, vol. 86, no. 3, pp. 959–994, Jul. 23, 2014.

[50] M. Jablan, H. Buljan, and M. Soljačić, "Plasmonics in graphene at infrared frequencies," *Physical Review B*, vol. 80, no. 24, p. 245 435, Dec. 23, 2009.

[51] A. Y. Nikitin, F. Guinea, F. J. García-Vidal, and L. Martín-Moreno, "Edge and waveguide terahertz surface plasmon modes in graphene microribbons," *Physical Review B*, vol. 84, no. 16, p. 081 405, Oct. 2011.

[52] R. Meservey and P. M. Tedrow, "Measurements of the Kinetic Inductance of Superconducting Linear Structures," *Journal of Applied Physics*, vol. 40, no. 5, pp. 2028–2034, 1969.

[53] M. Staffaroni, J. Conway, S. Vedantam, J. Tang, and E. Yablonovitch, "Circuit analysis in metal-optics," *Photonics and Nanostructures - Fundamentals and Applications*, vol. 10, no. 1, pp. 166–176, Jan. 2012.

[54] Y.-H. Suh and K. Chang, "Coplanar stripline resonators modeling and applications to filters," *IEEE Transactions on Microwave Theory and Techniques*, vol. 50, no. 5, pp. 1289–1296, May 2002.

[55] C. C. Teng, "Traveling-wave polymeric optical intensity modulator with more than 40 GHz of 3-dB electrical bandwidth," *Applied Physics Letters*, vol. 60, no. 13, p. 1538, 1992.

[56] K. Goverdhanam, R. N. Simons, and L. P. Katehi, "Coplanar stripline components for high-frequency applications," *Microwave Theory and Techniques, IEEE Transactions on*, vol. 45, no. 10, pp. 1725–1729, 1997.

[57] E. Chen and S. Chou, "Characteristics of coplanar transmission lines on multilayer substrates: Modeling and experiments," *IEEE Transactions on Microwave Theory and Techniques*, vol. 45, no. 6, pp. 939–945, Jun. 1997.

[58] G. Hanson, "Dyadic Green's Functions for an Anisotropic, Non-Local Model of Biased Graphene," *IEEE Transactions on Antennas and Propagation*, vol. 56, no. 3, pp. 747–757, Mar. 2008.

[59] A. D. Rakic, A. B. Djuri?i? J. M. Elazar, and M. L. Majewski, "Optical properties of metallic films for vertical-cavity optoelectronic devices," *Applied Optics*, vol. 37, no. 22, pp. 5271–5283, Aug. 1, 1998.

[60] H. Yan, F. Xia, W. Zhu, M. Freitag, C. Dimitrakopoulos, A. A. Bol, G. Tulevski, and P. Avouris, "Infrared Spectroscopy of Wafer-Scale Graphene," *ACS Nano*, vol. 5, no. 12, pp. 9854–9860, Dec. 27, 2011.

[61] V. Kumar and A. Naeemi, "Analytical models for the frequency response of multi-layer graphene nanoribbon interconnects," in *2012 IEEE International Symposium on Electromagnetic Compatibility (EMC)*, Aug. 2012, pp. 440–445.

[62] L. Lu, Y. Shen, X. Chen, L. Qian, and K. Lu, "Ultrahigh Strength and High Electrical Conductivity in Copper," *Science*, vol. 304, no. 5669, pp. 422–426, Apr. 16, 2004.

[63] J. D. Joannopoulos, S. G. Johnson, J. N. Winn, and R. D. Meade, *Photonic Crystals: Molding the Flow of Light (Second Edition)*. Princeton University Press, Oct. 30, 2011, 306 pp.

[64] S. Noda, T. Baba, O. I. (Japan), and T. D. Association, *Roadmap on Photonic Crystals*. Springer Science & Business Media, Jul. 31, 2003, 272 pp.

[65] S. G. Johnson, S. Fan, P. R. Villeneuve, J. D. Joannopoulos, and L. A. Kolodziejski, "Guided modes in photonic crystal slabs," *Physical Review B*, vol. 60, no. 8, pp. 5751–5758, Aug. 15, 1999.

[66] S. Fan, P. R. Villeneuve, J. D. Joannopoulos, and E. F. Schubert, "High extraction efficiency of spontaneous emission from slabs of photonic crystals," *Physical Review Letters*, vol. 78, no. 17, p. 3294, 1997.

[67] E. Chow, S. Y. Lin, S. G. Johnson, P. R. Villeneuve, J. D. Joannopoulos, J. R. Wendt, G. A. Vawter, W. Zubrzycki, H. Hou, and A. Alleman, "Three-dimensional control of light in a two-dimensional photonic crystal slab," *Nature*, vol. 407, no. 6807, pp. 983–986, Oct. 26, 2000.

[68] M. Loncar, T. Doll, J. Vuckovic, and A. Scherer, "Design and fabrication of silicon photonic crystal optical waveguides," *Journal of Lightwave Technology*, vol. 18, no. 10, pp. 1402–1411, Oct. 2000.

[69] S. McNab, N. Moll, and Y. Vlasov, "Ultra-low loss photonic integrated circuit with membrane-type photonic crystal waveguides," *Optics Express*, vol. 11, no. 22, pp. 2927–2939, Nov. 3, 2003.

[70] M. Notomi, "Strong Light Confinement With Periodicity," *Proceedings of the IEEE*, vol. 99, no. 10, pp. 1768–1779, Oct. 2011.

[71] S.-Y. Lin, E. Chow, V. Hietala, P. R. Villeneuve, and J. D. Joannopoulos, "Experimental Demonstration of Guiding and Bending of Electromagnetic Waves in a Photonic Crystal," *Science*, vol. 282, no. 5387, pp. 274–276, Sep. 10, 1998.

[72] A. Bingham, Y. Zhao, and D. Grischkowsky, "THz parallel plate photonic waveguides," *Applied Physics Letters*, vol. 87, no. 5, p. 051 101, Aug. 1, 2005.

[73] G. W. Hanson, "Dyadic Green's functions and guided surface waves for a surface conductivity model of graphene," *Journal of Applied Physics*, vol. 103, no. 6, p. 064 302, Mar. 15, 2008.

[74] Z. H. Chen, Q. L. Tan, J. Lao, Y. Liang, and X. G. Huang, "Reconfigurable and tunable flat graphene photonic crystal circuits," *Nanoscale*, vol. 7, no. 25, pp. 10 912–10 917, Jun. 18, 2015.

[75] K. Chang, J. T. Liu, J. B. Xia, and N. Dai, "Enhanced visibility of graphene: Effect of one-dimensional photonic crystal," *Applied Physics Letters*, vol. 91, no. 18, p. 181 906, Oct. 29, 2007.

[76] H. Da and C.-W. Qiu, "Graphene-based photonic crystal to steer giant Faraday rotation," *Applied Physics Letters*, vol. 100, no. 24, p. 241 106, 2012.

[77] O. L. Berman, V. S. Boyko, R. Y. Kezerashvili, A. A. Kolesnikov, and Y. E. Lozovik, "Graphene-based photonic crystal," *Physics Letters A*, vol. 374, no. 47, pp. 4784–4786, Oct. 25, 2010.

[78] K. Y. M. Yeung, J. Chee, H. Yoon, Y. Song, J. Kong, and D. Ham, "Far-Infrared Graphene Plasmonic Crystals for Plasmonic Band Engineering," *Nano Letters*, vol. 14, no. 5, pp. 2479–2484, May 14, 2014.

[79] A. Y. Nikitin, F. Guinea, F. J. Garcia-Vidal, and L. Martin-Moreno, "Surface plasmon enhanced absorption and suppressed transmission in periodic arrays of graphene ribbons," *Physical Review B*, vol. 85, no. 8, p. 081 405, Feb. 2012.

[80] S. Thongrattanasiri, F. H. L. Koppens, and F. J. García de Abajo, "Complete Optical Absorption in Periodically Patterned Graphene," *Physical Review Letters*, vol. 108, no. 4, Jan. 2012.

[81] M. G. Rybin, A. S. Pozharov, C. Chevalier, M. Garrigues, C. Seassal, R. Peretti, C. Jamois, P. Viktorovitch, and E. D. Obraztsova, "Enhanced optical absorbance of CVD-graphene monolayer by combination with photonic crystal slab," *physica status solidi (b)*, vol. 249, no. 12, pp. 2530–2533, Dec. 1, 2012.

[82] X. Gan, R.-J. Shiue, Y. Gao, K. F. Mak, X. Yao, L. Li, A. Szep, D. Walker, J. Hone, T. F. Heinz, and D. Englund, "High-Contrast Electrooptic Modulation of a Photonic Crystal Nanocavity by Electrical Gating of Graphene," *Nano Letters*, vol. 13, no. 2, pp. 691–696, Feb. 13, 2013.

[83] A. Majumdar, J. Kim, J. Vuckovic, and F. Wang, "Electrical Control of Silicon Photonic Crystal Cavity by Graphene," *Nano Letters*, vol. 13, no. 2, pp. 515–518, Feb. 13, 2013.

[84] T. Gu, N. Petrone, J. F. McMillan, A. van der Zande, M. Yu, G. Q. Lo, D. L. Kwong, J. Hone, and C. W. Wong, "Regenerative oscillation and four-wave mixing in graphene optoelectronics," *Nature Photonics*, vol. 6, no. 8, pp. 554–559, Jul. 15, 2012.

[85] M.-H. Shih, L.-J. Li, Y.-C. Yang, H.-Y. Chou, C.-T. Lin, and C.-Y. Su, "Efficient Heat Dissipation of Photonic Crystal Microcavity by Monolayer Graphene," *ACS Nano*, vol. 7, no. 12, pp. 10 818–10 824, Dec. 23, 2013.

[86] E. V. Loewenstein, D. R. Smith, and R. L. Morgan, "Optical constants of far infrared materials. 2: Crystalline solids," *Applied optics*, vol. 12, no. 2, pp. 398–406, 1973.

[87] F. H. L. Koppens, D. E. Chang, and F. J. García de Abajo, "Graphene Plasmonics: A Platform for Strong Light–Matter Interactions," *Nano Letters*, vol. 11, no. 8, pp. 3370–3377, Aug. 10, 2011.

[88] Z. Li and N. Yu, "Modulation of mid-infrared light using graphene-metal plasmonic antennas," *Applied Physics Letters*, vol. 102, no. 13, p. 131 108, 2013.

[89] Y. Yao, M. A. Kats, P. Genevet, N. Yu, Y. Song, J. Kong, and F. Capasso, "Broad Electrical Tuning of Graphene-Loaded Plasmonic Antennas," *Nano Letters*, vol. 13, no. 3, pp. 1257–1264, Mar. 13, 2013.

[90] K. F. Mak, L. Ju, F. Wang, and T. F. Heinz, "Optical spectroscopy of graphene: From the far infrared to the ultraviolet," *Solid State Communications*, Exploring Graphene, Recent Research Advances, vol. 152, no. 15, pp. 1341–1349, Aug. 2012.

[91] P.-Y. Chen, C. Argyropoulos, and A. Alu, "Terahertz Antenna Phase Shifters Using Integrally-Gated Graphene Transmission-Lines," *IEEE Transactions on Antennas and Propagation*, vol. 61, no. 4, pp. 1528–1537, Apr. 2013.

[92] C. Fietz, Y. Urzhumov, and G. Shvets, "Complex k band diagrams of 3D metamaterial/photonic crystals.," *Optics express*, vol. 19, no. 20, pp. 19 027–19 041, 2011.

[93] H. Yoon, K. Y. M. Yeung, V. Umansky, and D. Ham, "A Newtonian approach to extraordinarily strong negative refraction," *Nature*, vol. 488, no. 7409, pp. 65–69, Aug. 2, 2012.

[94] V. T. Renard, I. V. Gornyi, O. A. Tkachenko, V. A. Tkachenko, Z. D. Kvon, E. B. Olshanetsky, A. I. Toropov, and J.-C. Portal, "Quantum corrections to the conductivity and hall coefficient of a two-dimensional electron gas in a dirty $Al_xGa_{1-x}As/GaAs/Al_xGa_{1-x}As$ quantum well: From the diffusive to the ballistic regime," *Physical Review B*, vol. 72, no. 7, p. 075 313, Aug. 3, 2005.

[95] A. F. Braña, C. Diaz-Paniagua, F. Batallan, J. A. Garrido, E. Muñoz, and F. Omnes, "Scattering times in AlGaN/GaN two-dimensional electron gas from magnetoresistance measurements," *Journal of Applied Physics*, vol. 88, no. 2, pp. 932–937, Jul. 15, 2000.

[96] P. J. Burke, I. B. Spielman, J. P. Eisenstein, L. N. Pfeiffer, and K. W. West, "High frequency conductivity of the high-mobility two-dimensional electron gas," *Applied Physics Letters*, vol. 76, no. 6, pp. 745–747, Feb. 7, 2000.

[97] A. Mittal, R. G. Wheeler, M. W. Keller, D. E. Prober, and R. N. Sacks, "Electron-phonon scattering rates in GaAs/AlGaAs 2DEG samples below 0.5 K," *Surface Science*, vol. 361, pp. 537–541, Jul. 1, 1996.

[98] N. G. Asmar, A. G. Markelz, E. G. Gwinn, J. Černe, M. S. Sherwin, K. L. Campman, P. F. Hopkins, and A. C. Gossard, "Resonant-energy relaxation of terahertz-driven two-dimensional electron gases," *Physical Review B*, vol. 51, no. 24, pp. 18 041–18 044, Jun. 15, 1995.

[99] J. D. Thompson, B. M. Zwickl, A. M. Jayich, F. Marquardt, S. M. Girvin, and J. G. E. Harris, "Strong dispersive coupling of a high-finesse cavity to a micromechanical membrane," *Nature*, vol. 452, no. 7183, pp. 72–75, Mar. 6, 2008.

[100] H. Da, Q. Bao, R. Sanaei, J. Teng, K. P. Loh, F. J. Garcia-Vidal, and C.-W. Qiu, "Monolayer graphene photonic metastructures: Giant Faraday rotation and nearly perfect transmission," *Physical Review B*, vol. 88, no. 20, p. 205 405, Nov. 6, 2013.

[101] F. Gires and P. Tournois, "Interferometre utilisable pour la compression d'impulsions lumineuses modulees en frequence," *Comptes Rendus de l'Académie des Sciences*, vol. 258, pp. 6112–6115, 1964.

[102] J. Sabio, C. Seoánez, S. Fratini, F. Guinea, A. H. C. Neto, and F. Sols, "Electrostatic interactions between graphene layers and their environment," *Physical Review B*, vol. 77, no. 19, p. 195 409, May 6, 2008.

[103] N. Matuschek, F. X. Kartner, and U. Keller, "Exact coupled-mode theories for multilayer interference coatings with arbitrary strong index modulations," *IEEE JOURNAL OF QUANTUM ELECTRONICS*, vol. 33, no. 3, pp. 295–302, 1997.

[104] I. Favero, J. Sankey, and E. M. Weig, "Mechanical Resonators in the Middle of an Optical Cavity," in *Cavity Optomechanics*, M. Aspelmeyer, T. J. Kippenberg, and F. Marquardt, Eds., Berlin, Heidelberg: Springer Berlin Heidelberg, 2014, pp. 83–119.

[105] H. A. Haus, *Fields and Waves in Optoelectronics*, ser. Prentice-Hall Series in Solid State Physical Electronics. Prentice Hall, Incorporated, 1984.

[106] S. H. Mousavi, I. Kholmanov, K. B. Alici, D. Purtseladze, N. Arju, K. Tatar, D. Y. Fozdar, J. W. Suk, Y. Hao, A. B. Khanikaev, R. S. Ruoff, and G. Shvets, "Inductive Tuning of Fano-Resonant Metasurfaces Using Plasmonic Response of Graphene in the Mid-Infrared," *Nano Letters*, vol. 13, no. 3, pp. 1111–1117, Mar. 13, 2013.

[107] M. Aspelmeyer, T. J. Kippenberg, and F. Marquardt, "Cavity optomechanics," *Reviews of Modern Physics*, vol. 86, no. 4, pp. 1391–1452, Dec. 30, 2014.

[108] R. A. Barton, I. R. Storch, V. P. Adiga, R. Sakakibara, B. R. Cipriany, B. Ilic, S. P. Wang, P. Ong, P. L. McEuen, J. M. Parpia, and H. G. Craighead, "Photothermal Self-Oscillation and Laser Cooling of Graphene Optomechanical Systems," *Nano Letters*, vol. 12, no. 9, pp. 4681–4686, Sep. 12, 2012.

[109] A. Heidmann, J. Restrepo, J. Gabelli, C. Ciuti, and I. Favero, "Classical and quantum theory of photothermal cavity cooling of a mechanical oscillator," *Comptes Rendus Physique*, vol. 12, no. 9, pp. 860–870, Dec. 1, 2011.

[110] M. Aspelmeyer, T. J. Kippenberg, and F. Marquardt, Eds., *Cavity Optomechanics*, Berlin, Heidelberg: Springer Berlin Heidelberg, 2014.

[111] A. Pitanti, J. M. Fink, A. H. Safavi-Naeini, J. T. Hill, C. U. Lei, A. Tredicucci, and O. Painter, "Strong opto-electro-mechanical coupling in a silicon photonic crystal cavity," *Optics Express*, vol. 23, no. 3, pp. 3196–3208, Feb. 9, 2015.

[112] J. Chan, T. P. M. Alegre, A. H. Safavi-Naeini, J. T. Hill, A. Krause, S. Gröblacher, M. Aspelmeyer, and O. Painter, "Laser cooling of a nanomechanical oscillator into its quantum ground state," *Nature*, vol. 478, no. 7367, pp. 89–92, Oct. 6, 2011.

[113] A. H. Safavi-Naeini, T. P. M. Alegre, M. Winger, and O. Painter, "Optomechanics in an ultrahigh-Q two-dimensional photonic crystal cavity," *Applied Physics Letters*, vol. 97, no. 18, p. 181 106, Nov. 1, 2010.

[114] R. Schilling, H. Schütz, A. H. Ghadimi, V. Sudhir, D. J. Wilson, and T. J. Kippenberg, "Near-Field Integration of a SiN Nanobeam and a SiO2 Microcavity for Heisenberg-Limited Displacement Sensing," *Physical Review Applied*, vol. 5, no. 5, p. 054 019, May 26, 2016.

[115] K. Inoue, "Gain-clamped fiber amplifier with a short length of preamplification fiber," *IEEE Photonics Technology Letters*, vol. 11, no. 9, pp. 1108–1110, Sep. 1999.

[116] P. Ehlers, I. Silander, J. Wang, A. Foltynowicz, and O. Axner, "Fiber-laser-based noise-immune cavity-enhanced optical heterodyne molecular spectrometry incorporating an optical circulator," *Optics Letters*, vol. 39, no. 2, pp. 279–282, Jan. 15, 2014.

[117] R. Tkach and A. Chraplyvy, "Regimes of feedback effects in 1.5um distributed feedback lasers," *Journal of Lightwave Technology*, vol. 4, no. 11, pp. 1655–1661, Nov. 1986.

[118] A. M. Rollins and J. A. Izatt, "Optimal interferometer designs for optical coherence tomography," *Optics Letters*, vol. 24, no. 21, pp. 1484–1486, Nov. 1, 1999.

[119] A. Sabharwal, P. Schniter, D. Guo, D. W. Bliss, S. Rangarajan, and R. Wichman, "In-Band Full-Duplex Wireless: Challenges and Opportunities," *IEEE Journal on Selected Areas in Communications*, vol. 32, no. 9, pp. 1637–1652, Sep. 2014.

[120] J. Prat, V. Polo, C. Bock, C. Arellano, and J. Olmos, "Full-duplex single fiber transmission using FSK downstream and IM remote upstream Modulations for fiber-to-the-home," *IEEE Photonics Technology Letters*, vol. 17, no. 3, pp. 702–704, Mar. 2005.

[121] A. K. Dutta, N. K. Dutta, and M. Fujiwara, *WDM Technologies: Passive Optical Components*. Academic Press, Jun. 4, 2003, 551 pp.

[122] T. M. Stace, C. H. W. Barnes, and G. J. Milburn, "Mesoscopic One-Way Channels for Quantum State Transfer via the Quantum Hall Effect," *Physical Review Letters*, vol. 93, no. 12, p. 126 804, Sep. 17, 2004.

[123] G. Viola and D. P. DiVincenzo, "Hall Effect Gyrators and Circulators," *Physical Review X*, vol. 4, no. 2, p. 021 019, May 2, 2014.

[124] Y. Shoji, K. Miura, and T. Mizumoto, "Optical nonreciprocal devices based on magneto-optical phase shift in silicon photonics," *Journal of Optics*, vol. 18, no. 1, p. 013 001, Jan. 1, 2016.

[125] H. Dötsch, N. Bahlmann, O. Zhuromskyy, M. Hammer, L. Wilkens, R. Gerhardt, P. Hertel, and A. F. Popkov, "Applications of magneto-optical waveguides in integrated optics: Review," *JOSA B*, vol. 22, no. 1, pp. 240–253, 2005.

[126] D. Jalas, A. Petrov, M. Eich, W. Freude, S. Fan, Z. Yu, R. Baets, M. Popović, A. Melloni, J. D. Joannopoulos, M. Vanwolleghem, C. R. Doerr, and H. Renner, "What is — and what is not — an optical isolator," *Nature Photonics*, vol. 7, no. 8, pp. 579–582, Aug. 2013.

[127] M.-C. Tien, T. Mizumoto, P. Pintus, H. Kromer, and J. E. Bowers, "Silicon ring isolators with bonded nonreciprocal magneto-optic garnets," *Optics express*, vol. 19, no. 12, pp. 11 740–11 745, 2011.

[128] L. Bi, J. Hu, P. Jiang, D. H. Kim, G. F. Dionne, L. C. Kimerling, and C. A. Ross, "On-chip optical isolation in monolithically integrated non-reciprocal optical resonators," *Nature Photonics*, vol. 5, no. 12, pp. 758–762, Nov. 13, 2011.

[129] X. Y. Sun, Q. Du, T. Goto, M. C. Onbasli, D. H. Kim, N. M. Aimon, J. Hu, and C. A. Ross, "Single-Step Deposition of Cerium-Substituted Yttrium Iron Garnet for Monolithic On-Chip Optical Isolation," *ACS Photonics*, vol. 2, no. 7, pp. 856–863, Jul. 15, 2015.

[130] D. Huang, P. Pintus, C. Zhang, Y. Shoji, T. Mizumoto, and J. Bowers, "Electrically Driven and Thermally Tunable Integrated Optical Isolators for Silicon Photonics," *IEEE Journal of Selected Topics in Quantum Electronics*, vol. PP, no. 99, pp. 1–1, 2016.

[131] Y. Shoji, T. Mizumoto, H. Yokoi, I.-W. Hsieh, and R. M. Osgood, "Magneto-optical isolator with silicon waveguides fabricated by direct bonding," *Applied Physics Letters*, vol. 92, no. 7, p. 071 117, 2008.

[132] Y. Shoji, M. Ito, Y. Shirato, and T. Mizumoto, "MZI optical isolator with Si-wire waveguides by surface-activated direct bonding," *Optics express*, vol. 20, no. 16, pp. 18 440–18 448, 2012.

[133] S. Ghosh, S. Keyvavinia, W. Van Roy, T. Mizumoto, G. Roelkens, and R. Baets, "Ce: YIG/Silicon-on-Insulator waveguide optical isolator realized by adhesive bonding," *Optics express*, vol. 20, no. 2, pp. 1839–1848, 2012.

[134] S. Ghosh, S. Keyvaninia, Y. Shirato, T. Mizumoto, G. Roelkens, and R. Baets, "Optical Isolator for TE Polarized Light Realized by Adhesive Bonding of Ce:YIG on Silicon-on-Insulator Waveguide Circuits," *IEEE Photonics Journal*, vol. 5, no. 3, pp. 6 601 108–6 601 108, Jun. 2013.

[135] K. Fang and S. Fan, "Effective magnetic field for photons based on the magneto-optical effect," *Physical Review A*, vol. 88, no. 4, Oct. 2013.

[136] Z. Yu, G. Veronis, Z. Wang, and S. Fan, "One-Way Electromagnetic Waveguide Formed at the Interface between a Plasmonic Metal under a Static Magnetic Field and a Photonic Crystal," *Physical Review Letters*, vol. 100, no. 2, p. 023 902, Jan. 17, 2008.

[137] G. A. Peterson, F. Lecocq, K. Cicak, R. W. Simmonds, J. Aumentado, and J. D. Teufel, "Demonstration of efficient nonreciprocity in a microwave optomechanical circuit," *arXiv preprint arXiv:1703.05269*, 2017.

[138] L. Fan, J. Wang, L. T. Varghese, H. Shen, B. Niu, Y. Xuan, A. M. Weiner, and M. Qi, "An All-Silicon Passive Optical Diode," *Science*, vol. 335, no. 6067, pp. 447–450, Jan. 27, 2012.

[139] B. Peng, Ş. K. Özdemir, F. Lei, F. Monifi, M. Gianfreda, G. L. Long, S. Fan, F. Nori, C. M. Bender, and L. Yang, "Parity–time-symmetric whispering-gallery microcavities," *Nature Physics*, vol. 10, no. 5, pp. 394–398, Apr. 6, 2014.

[140] Y. Shi, Z. Yu, and S. Fan, "Limitations of nonlinear optical isolators due to dynamic reciprocity," *Nature Photonics*, vol. 9, no. 6, pp. 388–392, Jun. 2015.

[141] A. Rangelov and S. Longhi, "Nonlinear adiabatic optical isolator," Dec. 16, 2016.

[142] S. Hua, J. Wen, X. Jiang, Q. Hua, L. Jiang, and M. Xiao, "Demonstration of a chip-based optical isolator with parametric amplification," *Nature Communications*, vol. 7, p. 13 657, Nov. 25, 2016.

[143] S. Ibrahim, S. Bhandare, D. Sandel, H. Zhang, and R. Noe, "Non-magnetic 30 dB integrated optical isolator in III/V material," *Electronics Letters*, vol. 40, no. 20, pp. 1293–1294, Sep. 2004.

[144] S. Bhandare, S. K. Ibrahim, D. Sandel, H. Zhang, F. Wust, and R. Noe, “Novel nonmagnetic 30-dB traveling-wave single-sideband optical isolator integrated in III/V material,” *IEEE Journal of Selected Topics in Quantum Electronics*, vol. 11, no. 2, pp. 417–421, Mar. 2005.

[145] C. R. Doerr, L. Chen, and D. Vermeulen, “Silicon photonics broadband modulation-based isolator,” *Optics Express*, vol. 22, no. 4, pp. 4493–4498, Feb. 24, 2014.

[146] Z. Yu and S. Fan, “Complete optical isolation created by indirect interband photonic transitions,” *Nature Photonics*, vol. 3, no. 2, pp. 91–94, Feb. 2009.

[147] H. Lira, Z. Yu, S. Fan, and M. Lipson, “Electrically Driven Nonreciprocity Induced by Interband Photonic Transition on a Silicon Chip,” *Physical Review Letters*, vol. 109, no. 3, p. 033 901, Jul. 16, 2012.

[148] M. S. Kang, A. Butsch, and P. S. J. Russell, “Reconfigurable light-driven opto-acoustic isolators in photonic crystal fibre,” *Nature Photonics*, vol. 5, no. 9, pp. 549–553, Sep. 2011.

[149] D. L. Sounas, C. Caloz, and A. Alù, “Giant non-reciprocity at the subwavelength scale using angular momentum-biased metamaterials,” *Nature Communications*, vol. 4, p. 2407, Sep. 2, 2013.

[150] A. Kamal, J. Clarke, and M. H. Devoret, “Noiseless non-reciprocity in a parametric active device,” *Nature Physics*, vol. 7, no. 4, pp. 311–315, Apr. 2011.

[151] N. A. Estep, D. L. Sounas, J. Soric, and A. Alù, “Magnetic-free non-reciprocity and isolation based on parametrically modulated coupled-resonator loops,” *Nature Physics*, vol. 10, no. 12, pp. 923–927, Dec. 2014.

[152] N. Reiskarimian and H. Krishnaswamy, “Magnetic-free non-reciprocity based on staggered commutation,” *Nature Communications*, vol. 7, p. 11 217, Apr. 15, 2016.

[153] C. W. Peterson, S. Kim, J. T. Bernhard, and G. Bahl, “Reconfigurable arbitrary nonreciprocal transfer functions through nonreciprocal coupling,” *arXiv preprint arXiv:1702.06476*, 2017.

[154] M. Hafezi and P. Rabl, “Optomechanically induced non-reciprocity in microring resonators,” *Optics express*, vol. 20, no. 7, pp. 7672–7684, 2012.

[155] F. Ruesink, M.-A. Miri, A. Alù, and E. Verhagen, "Nonreciprocity and magnetic-free isolation based on optomechanical interactions," *Nature Communications*, vol. 7, p. 13 662, Nov. 29, 2016.

[156] K. Fang, J. Luo, A. Metelmann, M. H. Matheny, F. Marquardt, A. A. Clerk, and O. Painter, "Generalized nonreciprocity in an optomechanical circuit via synthetic magnetism and reservoir engineering," *Nature Physics*, Jan. 16, 2017.

[157] E. A. Kittlaus, N. T. Otterstrom, and P. T. Rakich, "On-chip Inter-modal Brillouin Scattering," Nov. 10, 2016.

[158] J. Kim, S. Kim, and G. Bahl, "Complete linear optical isolation at the microscale with ultralow loss," Oct. 29, 2016.

[159] J. Kim, M. C. Kuzyk, K. Han, H. Wang, and G. Bahl, "Non-reciprocal Brillouin scattering induced transparency," *Nature Physics*, vol. 11, no. 3, pp. 275–280, Jan. 26, 2015.

[160] N. R. Bernier, L. D. Tóth, A. Koottandavida, A. Nunnenkamp, A. K. Feofanov, and T. J. Kippenberg, "Nonreciprocal reconfigurable microwave optomechanical circuit," Dec. 24, 2016.

[161] A. Metelmann and A. A. Clerk, "Nonreciprocal Photon Transmission and Amplification via Reservoir Engineering," *Physical Review X*, vol. 5, no. 2, Jun. 15, 2015.

[162] T. Kitagawa, E. Berg, M. Rudner, and E. Demler, "Topological characterization of periodically driven quantum systems," *Physical Review B*, vol. 82, no. 23, Dec. 2010.

[163] R. Fleury, A. B. Khanikaev, and A. Alù, "Floquet topological insulators for sound," *Nature Communications*, vol. 7, p. 11 744, Jun. 17, 2016.

[164] K. Fang and S. Fan, "Controlling the Flow of Light Using the Inhomogeneous Effective Gauge Field that Emerges from Dynamic Modulation," *Physical Review Letters*, vol. 111, no. 20, Nov. 2013.

[165] T. Ozawa, H. M. Price, N. Goldman, O. Zilberberg, and I. Carusotto, "Synthetic dimensions in integrated photonics: From optical isolation to 4D quantum Hall physics," *Physical Review A*, vol. 93, no. 4, Apr. 15, 2016.

[166] Y. Shi and S. Fan, "Dynamic non-reciprocal meta-surfaces with arbitrary phase reconfigurability based on photonic transition in meta-atoms," *Applied Physics Letters*, vol. 108, no. 2, p. 021 110, Jan. 11, 2016.

[167] A. Yariv, *Quantum Electronics*. Wiley, Jan. 17, 1989, 702 pp.

[168] L. E. Reichl, "Driven Systems," in *The Transition to Chaos*, ser. Institute for Nonlinear Science, Springer New York, 1992, pp. 382–444.

[169] L. Ruby, "Applications of the Mathieu equation," *American Journal of Physics*, vol. 64, no. 1, pp. 39–44, Jan. 1, 1996.

[170] W. W. Mumford, "Some Notes on the History of Parametric Transducers," *Proceedings of the IRE*, vol. 48, no. 5, pp. 848–853, May 1960.

[171] C. Manolatou, M. J. Khan, S. Fan, P. R. Villeneuve, H. A. Haus, and J. D. Joannopoulos, "Coupling of modes analysis of resonant channel add-drop filters," *Quantum Electronics, IEEE Journal of*, vol. 35, no. 9, pp. 1322–1331, 1999.

[172] S. Fan, W. Suh, and J. Joannopoulos, "Temporal coupled-mode theory for the Fano resonance in optical resonators," *JOSA A*, vol. 20, no. 3, pp. 569–572, 2003.

[173] W. Suh, Z. Wang, and S. Fan, "Temporal coupled-mode theory and the presence of non-orthogonal modes in lossless multimode cavities," *IEEE Journal of Quantum Electronics*, vol. 40, no. 10, pp. 1511–1518, Oct. 2004.

[174] R. C. Jones, "A New Calculus for the Treatment of Optical Systems I. Description and Discussion of the Calculus," *JOSA*, vol. 31, no. 7, pp. 488–493, Jul. 1, 1941.

[175] A. Yariv, Y. Xu, R. K. Lee, and A. Scherer, "Coupled-resonator optical waveguide: A proposal and analysis," *Optics Letters*, vol. 24, no. 11, pp. 711–713, Jun. 1, 1999.

[176] U. P. Dharanipathy, M. Minkov, M. Tonin, V. Savona, and R. Houdre, "High-Q silicon photonic crystal cavity for enhanced optical nonlinearities," *Applied Physics Letters*, vol. 105, no. 10, p. 101 101, Sep. 8, 2014.

[177] H. Sekoguchi, Y. Takahashi, T. Asano, and S. Noda, "Photonic crystal nanocavity with a Q-factor of 9 million," *Optics Express*, vol. 22, no. 1, pp. 916–924, Jan. 13, 2014.

[178] G. T. Reed, G. Mashanovich, F. Y. Gardes, and D. J. Thomson, "Silicon optical modulators," *Nature Photonics*, vol. 4, no. 8, pp. 518–526, Aug. 2010.

[179] J. H. Wülbern, S. Prorok, J. Hampe, A. Petrov, M. Eich, J. Luo, A. K.-Y. Jen, M. Jenett, and A. Jacob, "40 GHz electro-optic modulation in hybrid silicon–organic slotted photonic crystal waveguides," *Optics letters*, vol. 35, no. 16, pp. 2753–2755, 2010.

[180] G. Acar and B. F. Feeny, "Floquet-Based Analysis of General Responses of the Mathieu Equation," *Journal of Vibration and Acoustics*, vol. 138, no. 4, p. 041 017, May 25, 2016.

[181] N. McLachlan, *Theory and Application of Mathieu Functions*. Clarendon Press, 1947.

[182] R. Soref and B. Bennett, "Electrooptical effects in silicon," *IEEE Journal of Quantum Electronics*, vol. 23, no. 1, pp. 123–129, Jan. 1987.

[183] L. Yuan, Y. Shi, and S. Fan, "Photonic gauge potential in a system with a synthetic frequency dimension," *Optics Letters*, vol. 41, no. 4, p. 741, Feb. 15, 2016.

[184] V.J. Urick, B. Bucholtz, and E.E. Funk, "High dynamic range, 100km digital radio-over-fiber links," in *Microwave Photonics*, CRC Press, Mar. 21, 2013, pp. 201–241.